Department of Physics and Astronomy

Ruprecht-Karls-University Heidelberg

Master's thesis in physics

submitted by

Tim Scherr

born in Neustadt an der Weinstraße

2017

Gradient-Based Surface Reconstruction

and the Application to Wind Waves

This master's thesis has been carried out by

Tim Scherr

at the Institute of Environmental Physics

under the supervision of

Prof. Dr. Bernd Jähne

Abstract   New gradient-based surface reconstruction techniques are presented: regularized least absolute deviations based methods using common discrete differential operators, and spline based methods. All new methods are formulated in the same mathematical framework as convex optimization problems and can handle non-rectangular domains. For the spline based methods, either common P-splines or P1-splines can be used. Extensive reconstruction error analysis shows that the new P1-spline based method is superior to conventional methods in the case of gradient fields corrupted with outliers. In the analysis, both spline based methods provide the lowest reconstruction errors for reconstructions from incomplete gradient fields. Furthermore, the pre-processing of gradient fields is investigated. Median filter pre-processing offers a computationally efficient method that is robust to outliers. After the reconstruction error analysis, selected reconstruction methods are applied to imaging slope gauge data measured in the wind-wave facility Aeolotron in Heidelberg. Using newly developed segmentation methods, it is possible to detect different coordinate system orientations of gradient field data and reconstruction algorithms. In addition, the use of a zero slope correction for reconstructions from the provided imaging slope gauge data is justified. The impact of light refracting bubbles on reconstructions from this data is part of this thesis as well. Finally, some water surface reconstructions for measurement conditions with different fetch lengths at the same wind speed in the Aeolotron are shown.

Zusammenfassung   Neue Methoden zur Oberflächenrekonstruktion aus Neigungsdaten werden vorgestellt: auf der Methode der kleinsten absoluten Abweichungen basierende Methoden mit Regularisierung und diskreten Ableitungsoperatoren, sowie splinebasierte Methoden. Die neuen Methoden sind in einem einheitlichen mathematischen Rahmen als konvexe Optimierungsprobleme formuliert. Bei den splinebasierten Methoden können gewöhnliche P-splines oder P1-splines eingesetzt werden. In einer ausführlichen Rekonstruktionsfehleranalyse zeigt sich, dass im Fall von Ausreißern die neue P1-spline Methode gewöhnlichen Methoden überlegen ist. Beide splinebasierte Methoden liefern in der Analyse die geringsten Rekonstruktionsfehler für Rekonstruktionen aus lückenhaften Neigungsdaten. Ein weiterer Punkt dieser Arbeit ist die Vorverarbeitung von Neigungsdaten. Durch Anwendung von Medianfiltern wird eine recheneffiziente Methode, die zu Ausreißern robust ist, ermöglicht. Nach der Fehleranalyse werden ausgewählte Rekonstruktionsmethoden auf Imaging Slope Gauge Daten, die im Wind-Wellen-Kanal Aeolotron in Heidelberg gemessen wurden, angewendet. Mit neu entwickelten Segmentierungsmethoden können unterschiedliche Koordinatensystemorientierungen von Neigungsdaten und Rekonstruktionsalgorithmen detektiert werden. Des Weiteren wird der Gebrauch einer Nullneigungskorrektur für Rekonstruktionen aus den bereitgestellten Imaging Slope Gauge Daten gerechtfertigt. Der Einfluss von lichtbrechenden Blasen im Wasser auf die Oberflächenrekonstruktion ist auch Teil dieser Arbeit. Zuletzt werden Wasseroberflächenrekonstruktionen für verschiedene Windantriebslängen bei gleicher Windgeschwindigkeit im Aeolotron gezeigt.

Contents

List of Symbols

$A, B, C, \ldots$	Matrices
$A^\top$	Transpose of matrix A
A^{-1}	Inverse of matrix A
A^+	Moore–Penrose pseudoinverse of matrix A
$a_{\cdot i}$	Column vector containing the i-th column of matrix A
$a_{i \cdot}$	Column vector containing the i-th row of matrix A
a_{ij}	Entry in the i-th row and j-th column of a matrix A
$a, b, c, \ldots$	Column vectors / matrices
$a^\top$	Row vector / matrix, transpose of column vector a
a_i	i-th component of vector a
$a, b, c, \ldots$	Scalars, constants, variables
$\alpha, \beta, \gamma, \ldots$	Parameters
$\alpha^*, x^*, \ldots$	Optimal parameter, variable, ...
B	B-spline basis matrix
g_{ij}	$\begin{pmatrix} p_{ij} & q_{ij} \end{pmatrix}^\top$, given discrete gradient field at position (i, j)
$g(x, y)$	$\begin{pmatrix} p(x, y) & q(x, y) \end{pmatrix}^\top$, given gradient field in the continuous domain
I_n	n-by-n identity matrix
LAD, LS	Least absolute deviations, least squares
MSE, RMSE	Mean-squared error, root-mean-squared error
P	x-components of a given discrete gradient field
p_{ij}	x-component of a given discrete gradient field at position (i, j)
$p, p(x, y)$	x-component of a given gradient field in the continuous domain
Q	y-components of a given discrete gradient field
q_{ij}	y-component of a given discrete gradient field at position (i, j)
$q, q(x, y)$	y-component of a given gradient field in the continuous domain
R / r	Matrix / vector containing residuals or errors
S	Cost functional
σ	Standard deviation of Gaussian noise
Z	Surface / height matrix (discrete)
z_{ij}	Entries of the surface / height matrix
$z(x, y)$	Surface / height function (continuous)
$0, 1, \ldots$	Column vector whose elements are all 0, 1, ...

Operators

$\mathscr{C}$	Discrete cosine transform
$\mathscr{C}^{-1}$	Inverse discrete cosine transform
$\boldsymbol{D}_1$	Matrix operator for first-order differences
$\boldsymbol{D}_2$	Matrix operator for second-order differences
$\mathbf{D}_x$	Matrix operator for discrete differentiation with respect to x
$\mathscr{F}$	Fourier transform
$\mathscr{F}^{-1}$	Inverse Fourier transform
tr	Trace of a square matrix
vec	Vectorization of a matrix, converts a matrix into a column vector
$\times$	Cross product / vector product
$\otimes$	Kronecker product
$\odot$	Hadamard product / Schur product
∂_x	Partial derivative with respect to x
∂_{xy}	$\partial_x \partial_y$
f_x	$\partial_x f$
f_{xy}	$\partial_{xy} f$
$\boldsymbol{\nabla}$	Nabla operator
Δ	Laplace operator
$\leq, \geq$	Less than or equal to, greater than or equal to (scalars)
$\preceq, \succeq$	Vector or componentwise inequality
$\lVert \cdot \rVert$	Norm on a vector space
$\lVert \cdot \rVert_1$	L^1-norm
$\lVert \cdot \rVert_2$	L^2-norm / Euclidean norm
$\lVert \cdot \rVert_F$	Frobenius norm / Hilbert-Schmidt norm
$\lVert \cdot \rVert_\infty$	L^∞-norm / maximum norm / uniform norm

Introduction   1

Ocean wave breaking plays a primary role in the air-sea exchange of momentum, mass, and heat (Melville, 1996; Babanin, 2011). Wave energy is transmitted into incoming turbulence and bubbles under the ocean interface, and into spray generation (Babanin, 2011). Microscale or micro breaking is the breaking of small-scale waves without entrainment of air (Banner & Phillips, 1974). Microscale breaking is the dominant mechanism contributing to air-sea heat and gas transfer at low to moderate wind speeds (Zappa, Asher, Jessup, Klinke, & Long, 2004). Small-scale shape of the water surface mirrors various small-scale exchange processes between the atmosphere and the ocean (Jähne, Klinke, & Waas, 1994). Since the ocean covers about 70 % of Earth's surface, the importance of these processes and wave breaking for climate is significant (Figure 1.1).

Measurement and detection of wave breaking are challenging tasks (Babanin, 2011). Several criteria for wave breaking that depend on the breaker's height have been proposed, e.g., from Munk (1949) and Komar and Gaughan (1972). Duncan, Qiao, Philomin, and Wenz (1999) found that the beginning of the breaking process for small-scale spilling breakers is marked by the formation of a bulge at the crest on the forward face of the wave. As the breaking process continues, this bulge becomes more pronounced while its toe remains in a nearly fixed position (Duncan et al., 1999). There are various experimental and numerical studies confirming the formation of a bulge for micro breakers, e.g., Iafrati and Campana (2005), Caulliez (2013), and Deike, Popinet, and Melville (2015).

There is need for methods that directly detect breaking events (Babanin, 2011). Spatial information about the shape of the water surface may be helpful to detect micro breakers. Water surfaces can be reconstructed from their measured gradient fields.

Gradient-Based Surface Reconstruction

Surface reconstruction from gradient fields is a problem appearing in many classic applications, such as shape from shading (B. K. P. Horn & Brooks, 1986; Frankot & Chellappa, 1988), photometric stereo (Ikeuchi, 1981), refractive imaging slope gauge (X. Zhang & Cox, 1994), image editing (Pérez, Gangnet, & Blake, 2003), or the numerical solution of partial differential equations (Simchony, Chellappa, & Shao, 1990). Modern applications include HDR compression (Fattal, Lischinski, & Werman, 2002), facial
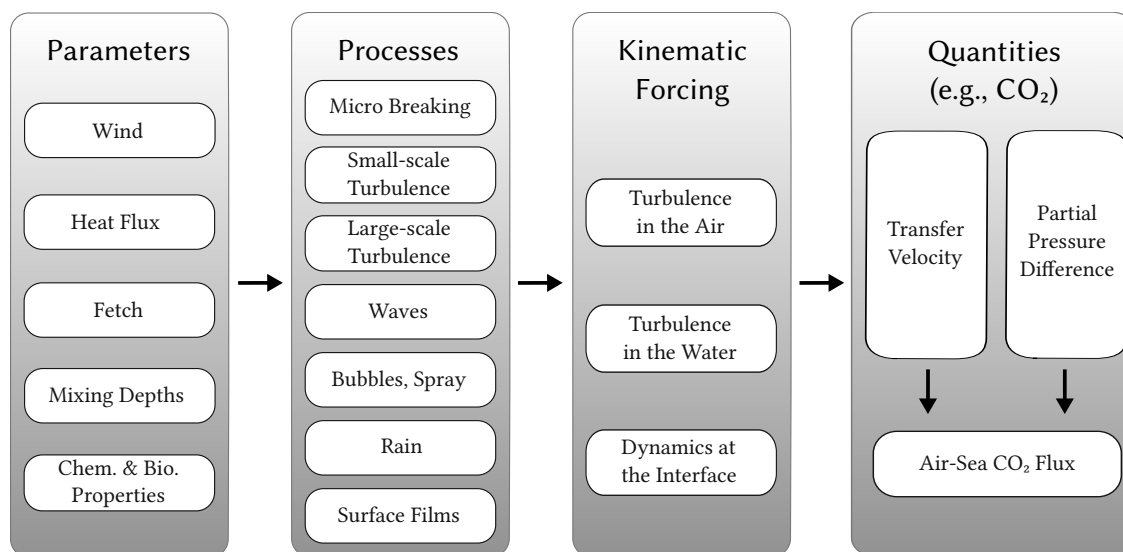
Figure 1.1 | Simplified Schematic of Factors Influencing Air-Sea Gas Transfer. The processes are closely connected, e.g., micro breaking generates turbulence. Modified after Garbe et al. (2014).

recognition (Hansen, Atkinson, Smith, & Smith, 2010), industrial workpiece tracking and surface inspection (Harker & O'Leary, 2013; Kang, Jang, & Won, 2013), and hybrid light field and photometric stereo approaches (Antensteiner et al., 2017).

This surface reconstruction problem is sometimes also called gradient-based surface reconstruction or surface normal integration. It is a classic problem in computer vision. The problem can be considered as the inversion of the process of differentiation. Nowadays, it is still a task to devise a method working on different domains with high accuracy, robustness, and computational efficiency (Bähr, Breuß, Quéau, Boroujerdi, & Durou, 2017). The solution can only be determined up to a integration constant.

Difficulties arise since measured gradient fields may be corrupted by noise and measuring errors. Thus, a gradient field is generally no longer integrable. If different noise forms or outliers are present, a least squares solution is no longer optimal in the maximum likelihood sense and some form of regularization is needed (Harker & O'Leary, 2015). Real-world gradient fields are not noise-free and may contain outliers since computer vision processes such as photometric stereo rely on simplified assumptions that often do not hold for illumination and surface reflectance (Bähr et al., 2017). The robustness to noise and outliers is therefore a major task in gradient-based surface reconstruction. Another difficulty may be the presence of depth discontinuities (Quéau & Durou, 2015).

The Mathematical Problem

While a measured gradient field is discrete, it is at times beneficial to formulate and solve the problem in the continuous domain. Let $g(x, y)$ be the given two-dimensional gradient

field and $p(x, y)$ and $q(x, y)$ its x- and y-components in the continuous domain. The surface z may in so-called local integration techniques be obtained via simple integration:

$$z(x, y) = \int_\gamma [p(x, y)\,\mathrm{d}x + q(x, y)\,\mathrm{d}y] = \int_\gamma \boldsymbol{g}(x, y)\,\mathrm{d}\boldsymbol{x} \ . \tag{1.1}$$

The integral may also be formulated in terms of the surface normal $\boldsymbol{n}$. Since the gradient field may be corrupted by noise or outliers, the surface z depends in such local integration techniques on the path γ. A way to suppress the influence of noise may be the averaging over many paths (Wu & Li, 1988). The discretization is simply done by using discrete integration formulas. However, local techniques propagate both the measurement error and the discretization error (Ettl, Kaminski, Knauer, & Häusler, 2008; Wu & Li, 1988).

More common are global integration techniques. Global integration techniques are based on a functional to minimize. Already B. K. P. Horn and Brooks (1986) stated the main points of global integration techniques:

1. Select a non-negative functional F such that

$$S(z) = \iint F\left(p, q, z, z_x, z_y, \dots\right)\,\mathrm{d}x\,\mathrm{d}y \tag{1.2}$$

   constitutes a measure of the departure of z from an ideal solution.

2. Absorb into F any constraint that z should satisfy.

3. Minimize the functional S.

4. Develop a discrete approximation.

For handling different forms of noise or outliers an appropriate functional has to be chosen. Major tasks of global integration techniques are the choice of this functional and the discretization. Additionally, difficulties may arise if the given gradient fields are imperfect, i.e., do not lie on a regular grid. This may be due to measurement limitations or due to segmentation of the gradient field into segments without depth discontinuities.

Formulating the problem in the continuous domain is not essential. In the discrete domain dealing with explicit boundary conditions is avoided (Quéau & Durou, 2015).

$$S(\boldsymbol{Z}) = \left\| F\left(\boldsymbol{P}, \boldsymbol{Q}, \boldsymbol{Z}, \boldsymbol{Z}_x, \boldsymbol{Z}_y, \dots\right)\right\| \ , \tag{1.3}$$

$\boldsymbol{Z}$, $\boldsymbol{P}$, and $\boldsymbol{Q}$ are the representations of the functional, the reconstructed surface, and the given gradient field in the discrete domain. In the discrete domain convex optimization methods may be used for minimizing S.

Another way to obtain a robust, accurate, and computationally efficient method for surface reconstruction may be pre-processing of the given gradient field data. Then a rather simple functional can be chosen. Here, the task is shifted to the data pre-processing.

Objectives and Structure of this Thesis

The scope of this thesis is an application analysis of gradient-based surface reconstruction methods to imaging slope gauge data. A reconstruction method should be robust to noise and rely on the mentioned main points of global integration techniques. At least one to outliers robust method is needed. How non-regular grids due to measurement limitations of the used imaging slope gauge can be treated is another task. It is an open question whether pre-processing may replace a computationally expensive functional.

This thesis is mainly split into three parts: theory and methods of measurement, reconstruction methods and reconstruction error analysis, and the application to imaging slope gauge data. The second part is widely uncoupled to reconstruction from imaging slope gauge data. The gained generality makes it more easy to compare with publications regarding surface reconstruction from gradient fields.

All methods used in this thesis are implemented within the software environment MATLAB. Sometimes, additional C++ source code running in MATLAB is used. Method and function names are written in italics for easy reading and recognition. Appendix C gives an overview of the functions and references to the sources of external code.

<div align="right">

Theory $\quad$ 2

</div>

Some gradient-based surface reconstruction methods may be formulated as convex optimization problems. An important component of all reconstruction methods is the numerical differentiation. The data often come as images. Thus, in this chapter a brief introduction in digital image processing, convex optimization, splines, and numerical differentiation is given. At last, some basics of water wave theory are reviewed.

2.1 Digital Image Processing

Most gradient measure techniques are optical and noninvasive. Usually, the gradient components are constructed of more than one image, e.g., in photometric stereo. Therefore, it is quite feasible to revise some basics of digital image processing. This section is based on Jähne (2005) and Jähne (2012).

Images represent the irradiance's distribution at a plane. Computers cannot handle continuous images. So, images are stored as 2-D discrete grids (matrices). A point on this grid is called a pixel and represents the irradiance. Since every pixel represents not only one point but a region, its size should be smaller than the smallest objects to investigate.

2.1.1 Image Formation

Image formation techniques project the 3-D object space onto a 2-D image plane. Technically seen in visual systems the 3-D world is reconstructed of 2-D images. The radiometry deals with the image intensity and its dependency from optical properties. In the steps of digitization and quantization a continuous image is converted into a digital image. The physical model of a camera and the mathematical model of a single pixel are shown in Figure 2.1. The signal-to-noise ratio increases to higher irradiations.

Digitization and Quantization

The digitization is the last step for generating a digital image and means a sampling of the image at selected positions on a discrete grid. The signal at the grid points is the integral over the area of a single sensor / pixel. The sampling theorem states that sampling loses
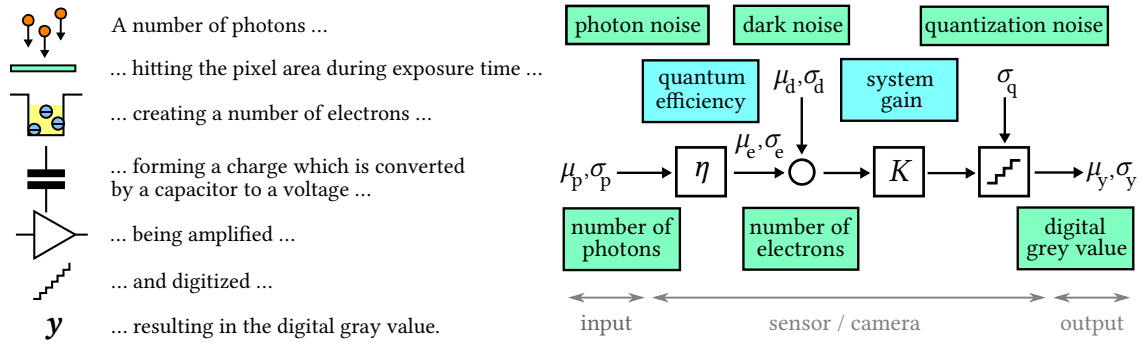
Figure 2.1 │ **Physical Model of a Camera and Mathematical Model of a Single Pixel.** The number of photons is Poisson distributed. Noise sources that are related to the sensor read out and the amplifier circuits can be described as a signal independent normal-distributed noise source with variance σ_d^2. Another noise source is the analog digital conversion. Modified from EMVA (2016).

no information if there is no wavenumber larger than the Nyquist wavenumber. The quantization maps the measured irradiance to a finite number of discrete gray values.

2.1.2 Filtering

Neighborhood operations combine pixels locally for new images. Information may be lost. Thus, these operators are called filter. An image must be extended periodically, embedded in zeros, or extrapolated for using a filter at the boundaries.

Smoothing filters are used to suppress Gaussian noise. Mathematically, smoothing with a binomial filter is a convolution with the mask $\frac{1}{2}\begin{bmatrix} 1 & 1 \end{bmatrix}$. For an efficient multi-dimensional smoothing the filter is applied to one after another dimension. For higher order filtering the filter can be applied several times.

Rank value filters sort the gray values in a neighborhood in ascending order and select one value. Median filters select the median. They can be used for filtering outliers and salt-and-pepper noise. In contrast to binomial filters, median filters are non-linear operators.

2.2 Convex Optimization

Convex optimization is a special class of mathematical optimization including least squares and linear programming. An advantage of formulating a problem as a convex optimization problem is the reliable and efficient solving (Boyd & Vandenberghe, 2009). A mathematical optimization problem has the form

$$
\begin{aligned}
& \text{minimize} && f_0(\boldsymbol{x}) \\
& \text{subject to} && f_i(\boldsymbol{x}) \le b_i, \quad i = 1, \dots, m.
\end{aligned}
\tag{2.1}
$$

The vector $\boldsymbol{x} \in \mathbb{R}^n$ is the optimization variable, $f_0 : \mathbb{R}^n \to \mathbb{R}$ the objective function, $f_i : \mathbb{R}^n \to \mathbb{R}$ the constraint functions and $b_i \in \mathbb{R}$ the limits or bounds for the constraints (Boyd & Vandenberghe, 2009). $\boldsymbol{x}^*$ is the optimal solution to the problem if $f_0(\boldsymbol{x}^*)$ is minimal and the constraints are satisfied.

A convex optimization problem is an optimization problem in which the objective and the constraint functions are convex (Boyd & Vandenberghe, 2009):

$$f_i(\alpha\,\boldsymbol{x} + \beta\,\boldsymbol{y}) \le \alpha\,f_i(\boldsymbol{x}) + \beta\,f_i(\boldsymbol{x}) \qquad \forall\,\boldsymbol{x}, \boldsymbol{y} \in \mathbb{R}^n,\ \alpha, \beta \in \mathbb{R}_{\ge 0} : \alpha + \beta = 1\ . \quad (2.2)$$

If the equality holds for all $\alpha, \beta \in \mathbb{R}$, the optimization problem is called a linear program. If each constraint function depends only on a small number of the variables, the problem is called sparse.

2.2.1 Least Squares Problems

A least squares (LS) problem is a convex optimization problem with no constraints and an objective function expressible as a sum of squares:

$$\text{minimize} \quad f_0(\boldsymbol{x}) = \|\boldsymbol{A}\boldsymbol{x} - \boldsymbol{b}\|_2^2 = (\boldsymbol{A}\boldsymbol{x} - \boldsymbol{b})^\top (\boldsymbol{A}\boldsymbol{x} - \boldsymbol{b})\ , \quad (2.3)$$

with the matrix $\boldsymbol{A} \in \mathbb{R}^{m \times n}$ ($m \ge n$), the vector $\boldsymbol{b} \in \mathbb{R}^m$ and the L^2-norm $\|\cdot\|_2$ (Boyd & Vandenberghe, 2009). This problem is the basis for linear regression analysis and many parameter estimation methods, e.g., maximum likelihood estimation, given linear measurements corrupted by Gaussian measurement errors (Boyd & Vandenberghe, 2009). Straightforward minimization (Appendix A) yields the so-called normal equations

$$\boldsymbol{A}^\top \boldsymbol{A}\boldsymbol{x}^* = \boldsymbol{A}^\top \boldsymbol{b}\ . \quad (2.4)$$

For solving least squares problems efficiently and stable see, e.g., Björck (2015). The normal equations can be much worse conditioned than its underlying LS problem (Björck, 2015). In this thesis MATLAB's *mldivide* is used which implements a range of algorithms depending on the input $\boldsymbol{A}$ and $\boldsymbol{b}$. For under-determined systems a solution with minimum $\|\boldsymbol{x}\|_2$ can be computed with the Moore-Penrose pseudoinverse $\boldsymbol{A}^+$.

Weighted Least Squares

Weighted least squares are used if given linear measurements are corrupted by errors with unequal variance or simply to influence the solution (Boyd & Vandenberghe, 2009):

$$\text{minimize} \quad f_0(\boldsymbol{x}) = \|\boldsymbol{W}(\boldsymbol{A}\boldsymbol{x} - \boldsymbol{b})\|_2^2\ . \quad (2.5)$$

$\boldsymbol{W} \in \mathbb{R}^{m \times m}$ is a diagonal matrix with the weights on the diagonal.

Regularization

In regularization, extra terms are added to the objective function to solve ill-posed problems, e.g., standard form Tikhonov regularization (Golub, Hansen, & O'Leary, 1999)

$$\text{minimize} \quad f_0(x) = \|Ax - b\|_2^2 + \lambda \|x\|_2^2 = (Ax - b)^\top (Ax - b) + \lambda \, x^\top x \, . \quad (2.6)$$

2.2.2 Linear Programming

In linear programming all objective and constraint functions are linear. In contrast to the least squares problem, there is no simple analytic formula for the solution of a linear program, but there are effective methods for solving it (Boyd & Vandenberghe, 2009). The least absolute deviations (LAD) statistical optimality criterion

$$\text{minimize} \quad f_0(x) = \|Ax - b\|_1 = \sum_i \left| a_{i\cdot}^\top x - b_i \right| \, , \quad (2.7)$$

where $\|\cdot\|_1$ denotes the L^1-norm and $a_{i\cdot}^\top$ is a row vector containing the i-th row of the matrix A, can be formulated and solved as a linear program efficiently (Barrodale & Roberts, 1973; Boyd & Vandenberghe, 2009, see Appendix A). Linear programs are solved in this thesis with the solver Gurobi (Gurobi Optimization, Inc., 2017).

2.2.3 Norm Approximation

A norm approximation problem is an unconstrained convex problem of the form

$$\text{minimize} \quad f_0(x) = \|Ax - b\| = \|r\| \, . \quad (2.8)$$

Goal is to approximate the vector b as closely as possible with the deviation measured in the norm $\| \cdot \|$. The components of the vector $r \in \mathbb{R}^m$ are called the residuals (Boyd & Vandenberghe, 2009). Weights can be introduced for formulating a weighted norm approximation problem

$$\text{minimize} \quad f_0(x) = \|W(Ax - b)\| \, . \quad (2.9)$$

L^1-norm vs L^2-norm

The L^1-norm weights small residuals more and large residuals less than the L^2-norm. In the case of outliers the L^1-approximation is superior to L^2-approximation for estimating the true form of data (Barrodale & Roberts, 1973). While LAD is more robust to outliers than is LS, LAD is more often unstable as well (Ellis, 1998). In many applications, the L^1-norm is robust enough since the measurements and their errors are bounded (Ke & Kanade, 2005). The robustness is demonstrated in the linear regressions in Figure 2.2.

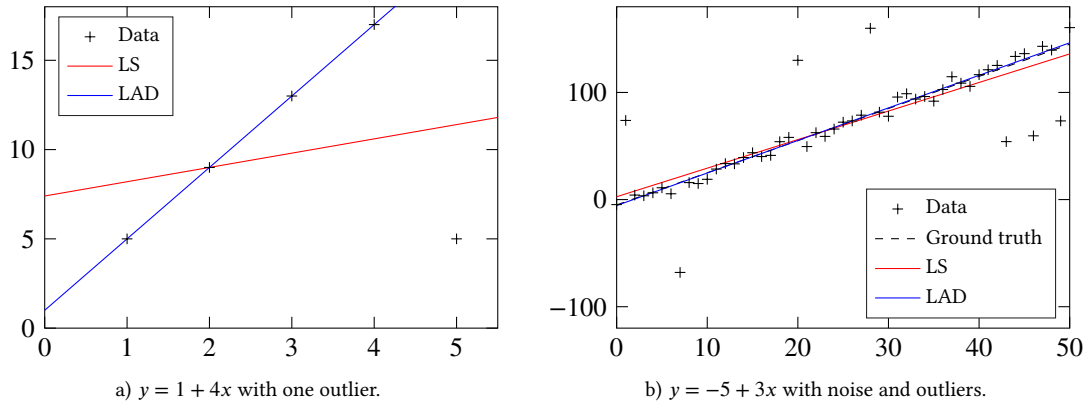a) $y = 1 + 4x$ with one outlier. b) $y = -5 + 3x$ with noise and outliers.

Figure 2.2 | Linear Regression with Least Squares and with Least Absolute Deviations. The least squares method is more sensitive to outliers than the least absolute deviations method.

2.3 Error Measure

To compare a reconstructed surface Z with its ground truth Z_0, a matrix norm as error measure is needed. For a matrix $A \in \mathbb{R}^{m \times n}$ a vector norm for the vector $\text{vec}(A)$ consisting of the mn components of A can be used (Björck, 2015). The Frobenius norm

$$\|A\|_F := \|\text{vec}(A)\|_2 = \sqrt{\text{tr}(A^\top A)} = \sqrt{\sum_{i=1}^{m} \sum_{j=1}^{n} |a_{ij}|^2} \tag{2.10}$$

is derived from the vector L^2-norm. The mean squared error and the root-mean-squared error of a reconstruction are

$$\text{MSE} := \min_{\beta} \frac{1}{m\,n} \left\| Z_0 - (Z + \beta) \right\|_F^2, \tag{2.11}$$

$$\text{RMSE} = \sqrt{\text{MSE}}. \tag{2.12}$$

Minimizing β corrects a method-dependent shift since the integration constant is not known. This shift has no significance for the reconstruction quality. Harker and O'Leary (2015) also remove any bias due to scaling. But if the scaling is surface-independent, the method could be corrected. If not, it makes no sense to minimize the error for scaling.

Since large errors are weighted more than small errors, the Frobenius norm is a natural choice as an error measure. As Harker and O'Leary (2015) state, it is common in literature "to find only subjective reconstruction results, leaving the reader to 'eyeball' the quality of the results". Furthermore, the reconstructions are at times not shifted to the reference level of Z_0, making comparisons of reconstruction errors of different methods useless. Beside the root-mean-squared error, the errors' distribution may give indications for systematic errors as well and is a kind of fingerprint of erroneous algorithms.

2.4 Splines

Polynomials are often used for approximation or interpolation because they can be evaluated, differentiated, and integrated easily (de Boor, 2001). Polynomial approximation depends globally on local properties (de Boor, 2001). This dependence, and thereby instabilities due to Runge's phenomenon, can be avoided with piecewise polynomials, the splines.

A spline of degree k is a function consisting piecewise of polynomials with maximum degree k. Places where the polynomials connect are called knots. At this knots the joining pieces underlie a certain number of constraints, e.g., that the spline should have $k - 1$ continuous derivatives. A popular choice are cubic splines ($k = 3$).

Cubic Spline Interpolation

Given data $y_1, \dots, y_n$ and the related knots $t_1 < \dots < t_n$ the cubic spline interpolant is

$$f(x) = P_i(x) \qquad \text{for} \quad t_i \le x \le t_{i+1}, \; i = 1, \dots, n-1 \tag{2.13}$$

with polynomials P_i of degree 3 satisfying the conditions (de Boor, 2001)

$$P_i(t_i) = y_i, \quad P_i(t_{i+1}) = y_{i+1}, \quad P_i'(t_i) = s_i, \quad P_i'(t_{i+1}) = s_{i+1}, \tag{2.14}$$

The resulting cubic spline interpolant is continuous and has a continuous first derivative on $[t_1, t_n]$, regardless of how the free parameters $s_1, \dots, s_n$ are chosen.

Smoothing Splines

For experimental data with unknown underlying function there may be be a demand of smoothing instead of strict interpolation (Reinsch, 1967). Cubic smoothing splines are the solution of (Reinsch, 1967; de Boor, 2001)

$$\text{minimize} \quad p \sum_{i=1}^{n} \left[y_i - f(x_i) \right]^2 + (1-p) \int_{t_1}^{t_n} \left[f''(t) \right]^2 \mathrm{d}t \, . \tag{2.15}$$

The smoothing parameter ranges from $p = 0$ to $p = 1$. A smoothing parameter $p = 1$ corresponds to the cubic spline interpolant.

2.4.1 B-splines

Typical problems involving splines are interpolation and smoothing of data. The computational efficiency demands the construction of a convenient basis resulting in the

so-called B-splines or basis splines (de Boor, 2001). The i-th B-spline of degree 0 for the knot sequence $t_1, \dots, t_n$ is (de Boor, 2001)

$$B_{i,0}(x) = \begin{cases} 1 \,, & \text{for } t_i \leq x < t_{i+1}; \\ 0 \,, & \text{otherwise.} \end{cases} \tag{2.16}$$

B-splines of degree $k > 0$ can be calculated with the recurrence relation (de Boor, 2001)

$$B_{i,k}(x) = \frac{x - t_i}{t_{i+k} - t_i} B_{i,k-1}(x) + \frac{t_{i+k+1} - x}{t_{i+k+1} - t_{i+1}} B_{i+1,k-1}(x) \,. \tag{2.17}$$

Properties of B-splines (de Boor, 2001; Eilers & Marx, 1996):

- $B_{i,k}(x)$ is a piecewise polynomial of degree k with knots $t_i, \dots, t_{i+k+1}$.
- The $k + 1$ polynomial pieces with degree k join at k inner knots.
- At these joining points, derivatives up to order k-1 are continuous.
- $B_{i,k}(x) = 0$ for $x \notin [t_i, t_{i+k+1})$ and $B_{i,k}(x) > 0$ for $x \in [t_i, t_{i+k+1})$.
- A spline of degree k is a linear combination of B-splines $\sum_i \alpha_i B_{i,k}$.
- At a given x are $k + 1$ B-splines nonzero.
- Too many knots lead to overfitting of the data, too few to underfitting.

Splines can be differentiated easily in the interval $[t_r, t_s]$ by differencing their B-spline coefficients (de Boor, 2001):

$$\frac{\mathrm{d}}{\mathrm{d}x} \sum_i \alpha_i B_{i,k}(x) = \sum_i \alpha_i B'_{i,k}(x) = k \sum_{i=r-k+1}^{s-1} \frac{\alpha_i - \alpha_{i-1}}{t_{i+k} - t_i} B_{i,k-1}(x) \,. \tag{2.18}$$

The regression of m data points (x_i, y_i) on a set of n B-splines $B_{j,k}(x)$ can be formulated as a norm approximation problem:

$$\text{minimize} \quad f_0(\boldsymbol{\alpha}) = \|\boldsymbol{B}\boldsymbol{\alpha} - \boldsymbol{y}\| \,. \tag{2.19}$$

$\boldsymbol{\alpha}$ is an n-by-1 vector of the B-splines coefficients and the sparse m-by-n basis matrix

$$b_{ij} = B_{j,k}(x_i) \tag{2.20}$$

is built in such a way that $(\boldsymbol{B}\boldsymbol{\alpha})_i$ equals the spline $\sum_j \alpha_j B_{j,k}(x)$ evaluated at x_i.

Cardinal B-splines

Cardinal B-splines are B-splines with uniform knot sequences. Cardinal B-splines of the same degree k are shifted copies of each other. Figure 2.3 shows cardinal linear and

a) Cardinal linear B-splines ($k = 1$). b) Cardinal cubic B-splines ($k = 3$).
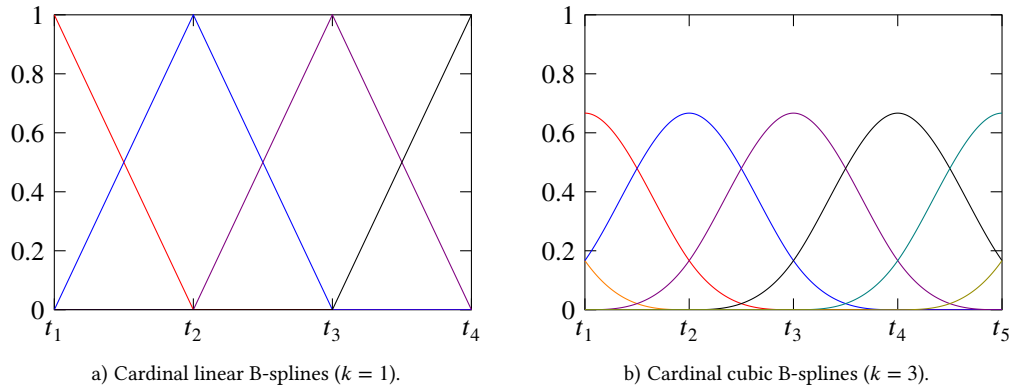
Figure 2.3 | Cardinal Linear and Cardinal Cubic B-splines. In each interval $k + 1$ B-splines are nonzero. The $k + 1$ nontrivial polynomial pieces of a B-spline connect at k inner knots.

cardinal cubic B-splines. The recurrence relation for building cardinal B-splines with knot separation h simplifies to

$$B_{i,k}(x) = B_{i+j,k}(x + j \cdot h) = \frac{x - t_i}{k\,h} B_{i,k-1}(x) + \frac{t_{i+k+1} - x}{k\,h} B_{i+1,k-1}(x) \ . \tag{2.21}$$

The differentiation of splines to

$$h \sum_i \alpha_i B'_{i,k}(x) = \sum_i \left(\alpha_i - \alpha_{i-1}\right) B_{i,k-1}(x) = \sum_i \Delta\alpha_i B_{i,k-1}(x) \ , \tag{2.22}$$

$$h^2 \sum_i \alpha_i B''_{i,k}(x) = \sum_i \left(\alpha_i - 2\alpha_{i-1} + \alpha_{i-2}\right) B_{i,k-2}(x) = \sum_i \Delta^2\alpha_i B_{i,k-2}(x) \ . \tag{2.23}$$

2.4.2 P-splines

Choosing the optimal number and positions of knots for smoothing is a complex task (Eilers & Marx, 1996). O'Sullivan (1986, 1988) proposed to use a relatively large number of knots and a penalty on the second derivative of the spline, similar to the ansatz of Reinsch (1967) in Eq. 2.15. The penalty prevents overfitting.

Usually, P-splines are a combination of cardinal cubic B-splines and a second-order difference penalty on the estimated B-spline coefficients instead of an integral on the spline derivative. They are a simplification of O'Sullivan's approach. Both approaches are very similar for second-order differences (Eilers & Marx, 1996). However, P-splines are not restricted to cardinal cubic B-splines and second-order difference penalties.

The minimization problem for the regression of m data points $\left(x_i, y_i\right)$ on a set of n cardinal B-splines $B_{j,k}(x)$ in the P-spline approach is (Eilers & Marx, 1996):

$$\text{minimize} \quad f_0(\boldsymbol{\alpha}) = \|\boldsymbol{B\alpha} - \boldsymbol{y}\|_2^2 + \|\lambda\,\boldsymbol{D}_2\boldsymbol{\alpha}\|_2^2 \ . \tag{2.24}$$

n should be large, such that the fitted curve will show more variation than is justified by the data without the penalty (Eilers & Marx, 1996). $\lambda > 0$ is a smoothing parameter.

$$\boldsymbol{D}_2 = \boldsymbol{D}_{2,n} = \begin{pmatrix} 1 & -2 & 1 & 0 & 0 & \ldots & 0 & 0 & 0 \\ 0 & 1 & -2 & 1 & 0 & \ldots & 0 & 0 & 0 \\ \vdots & \vdots & \vdots & \vdots & \vdots & \vdots & \vdots & \vdots & \vdots \\ 0 & 0 & 0 & 0 & 0 & \ldots & 1 & -2 & 1 \end{pmatrix} \tag{2.25}$$

is the sparse $(n-2)$-by-n matrix representation of the second-order difference operator Δ^2 defined in Eq. 2.23. The solution of the P-spline regression minimization problem is

$$\left(\boldsymbol{B}^\top \boldsymbol{B} + \lambda^2 \boldsymbol{D}_2^\top \boldsymbol{D}_2\right) \boldsymbol{\alpha}^* = \boldsymbol{B}^\top \boldsymbol{y} \,. \tag{2.26}$$

These are the normal equations for the augmented least squares problem

$$\text{minimize} \quad f_0(\boldsymbol{\alpha}) = \left\| \begin{pmatrix} \boldsymbol{B} \\ \lambda \boldsymbol{D}_2 \end{pmatrix} \boldsymbol{\alpha} - \begin{pmatrix} \boldsymbol{y} \\ \boldsymbol{0} \end{pmatrix} \right\|_2^2 \,. \tag{2.27}$$

Further details and properties of P-splines can be found in, e.g., Eilers and Marx (2010).

P1-splines

Using the L^1-norm instead of the L^2-norm in Eq. 2.24 yields the so-called P1-splines

$$\text{minimize} \quad f_0(\boldsymbol{\alpha}) = \left\| \boldsymbol{B}\boldsymbol{\alpha} - \boldsymbol{y} \right\|_1 + \lambda \left\| \boldsymbol{D}_2 \boldsymbol{\alpha} \right\|_1 \,. \tag{2.28}$$

The corresponding least absolute deviations or L^1-norm approximation problem is

$$\text{minimize} \quad f_0(\boldsymbol{\alpha}) = \left\| \begin{pmatrix} \boldsymbol{B} \\ \lambda \boldsymbol{D}_2 \end{pmatrix} \boldsymbol{\alpha} - \begin{pmatrix} \boldsymbol{y} \\ \boldsymbol{0} \end{pmatrix} \right\|_1 \,, \tag{2.29}$$

which can be solved as a linear program.

Cross-Validation

Choosing the optimal amount of smoothing is a major problem of any smoothing technique (Eilers & Marx, 1996). The minimization of the leave-one-out cross-validation

$$\text{CV}(\lambda) = \sum_i \left(y_i - y_{-i}^*\right)^2 \stackrel{\text{P-splines}}{=} \sum_i \left(\frac{y_i - y_i^*}{1 - h_{ii}}\right)^2 \tag{2.30}$$

provides a tool for choosing the smoothing parameter λ (Eilers, Marx, & Durbán, 2015). Thereby is y_{-i}^* the interpolated value for the regression with observation y_i left out, y_i^* the smoothed value with all observations. and $\boldsymbol{H} = \boldsymbol{B} \left(\boldsymbol{B}^\top \boldsymbol{B} + \lambda^2 \boldsymbol{D}_2^\top \boldsymbol{D}_2\right)^{-1} \boldsymbol{B}^\top$.
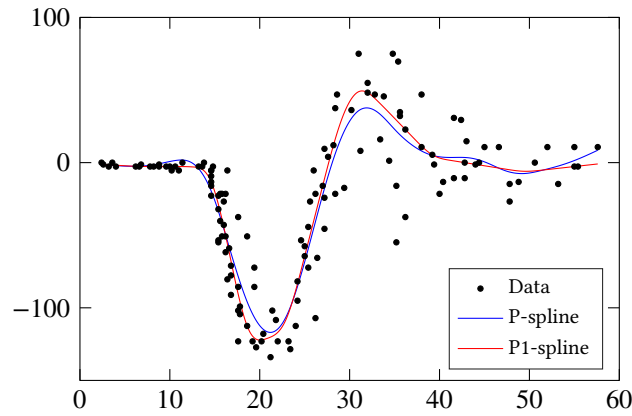
Figure 2.4 │ P-spline Smoothing of Motorcycle Crash Helmet Impact Data. The smoothing parameter, that was obtained via cross-validation for the P-spline, is also used for the P1-spline.
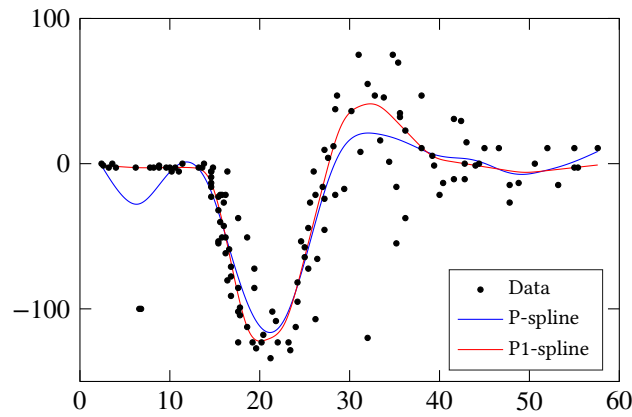

Figure 2.5 │ P-spline Smoothing of Motorcycle Crash Helmet Impact Data with Outliers. The smoothing parameter, that was obtained via cross-validation for the P-spline, is also used for the P1-spline. Concerning outliers, the P1-spline outperforms the P-spline.

A slightly different parameter is produced by the for large datasets significant faster minimization of the generalized cross-validation (Eilers & Marx, 1996; Eilers et al., 2015):

$$\text{CV}(\lambda) = \left\| \frac{\boldsymbol{y} - \boldsymbol{y}^*}{m - \text{tr}(\boldsymbol{H})} \right\|_2^2, \quad \text{tr}(\boldsymbol{H}) = \text{tr}\left(\boldsymbol{I}_n - \left(\boldsymbol{B}^\top \boldsymbol{B} + \lambda^2 \boldsymbol{D}_2^\top \boldsymbol{D}_2\right)^{-1} \lambda^2 \boldsymbol{D}_2^\top \boldsymbol{D}_2\right). \quad (2.31)$$

For P1-splines only a brute-force cross-validation method can be applied. However, the best smoothing parameter for P-splines seems to be reasonable for P1-splines too. Figure 2.4 and Figure 2.5 show the smoothing of motorcycle crash helmet impact data taken from Härdle (1990). The robustness to outliers of P1-splines is at the cost of computation time.

2-D P-splines

As many data to be smoothed come as large grids of values, e.g., images, an extension of P-splines to higher dimensions is needed. Since even for relatively small multidimensional datasets the memory consumption gets quickly out of hand, Eilers, Currie, and Durbán (2006) proposed a framework for effective smoothing of data in multidimensional arrays.

A straightforward extension using tensor product B-splines diminishes the memory consumption by using the fact that the B-spline basis matrices are sparse. This extension is conceptual more simple than the framework proposed by Eilers et al. (2006) and is valid for P1-splines too. Working with data on a grid, the extension for 2-D P-splines is:

$$\text{minimize} \quad f_0\left(\boldsymbol{\alpha}\right) = \left\| \begin{pmatrix} \boldsymbol{W} \cdot \left(\boldsymbol{B}_x \otimes \boldsymbol{B}_y \right) \\ \lambda_x \, \boldsymbol{D}_{2,x} \\ \lambda_y \, \boldsymbol{D}_{2,y} \end{pmatrix} \boldsymbol{\alpha} - \begin{pmatrix} \text{vec}\left(\boldsymbol{Z}\right) \\ \boldsymbol{0} \\ \boldsymbol{0} \end{pmatrix} \right\|_p^p . \tag{2.32}$$

$\boldsymbol{Z} \in \mathbb{R}^{m \times n}$ is the surface to be smoothed. $\text{vec}\left(\boldsymbol{Z}^*\right) = \left(\boldsymbol{B}_x \otimes \boldsymbol{B}_y \right) \boldsymbol{\alpha}^* = \boldsymbol{C}\boldsymbol{\alpha}^*$ is the smoothed surface vector. $\boldsymbol{B}_x \in \mathbb{R}^{n \times n_x}$ and $\boldsymbol{B}_y \in \mathbb{R}^{m \times n_y}$ are the B-spline basis matrices of 1-D cardinal B-splines in x- and y-direction with number n_x and n_y, and degree k_x and k_y. $\boldsymbol{C}$ is the tensor product basis matrix.

$$\boldsymbol{D}_{2,x} = \boldsymbol{D}_{2,n_x} \otimes \boldsymbol{I}_{n_y} \quad \text{and} \quad \boldsymbol{D}_{2,y} = \boldsymbol{I}_{n_x} \otimes \boldsymbol{D}_{2,n_y} \tag{2.33}$$

are reformulations of the second-order differences matrices for the x- and y-direction $\boldsymbol{D}_{2,n_x} \in \mathbb{R}^{n_x-2 \times n_x}$ and $\boldsymbol{D}_{2,n_y} \in \mathbb{R}^{n_y-2 \times n_y}$. $\boldsymbol{W}$ is a diagonal weight matrix for handling gaps in the data. Pseudo-observations with zero weights and zero values for $\boldsymbol{Z}$ have to be introduced to handle missing data in this notation. Weights for available data are 1.

For $p = 1$ P1-spline smoothing is applied and for $p = 2$ P-spline smoothing. For 2-D P-splines the generalized cross-validation can be applied:

$$\text{CV}\left(\lambda\right) = \left\| \frac{\boldsymbol{Z} - \boldsymbol{Z}^*}{m\,n - \text{tr}\left(\boldsymbol{H}\right)} \right\|_F^2 , \quad \text{tr}\left(\boldsymbol{H}\right) = \text{tr}\left(\boldsymbol{I}_{n_x \cdot n_y} - \left(\boldsymbol{C}^\top \boldsymbol{W} \boldsymbol{C} + \boldsymbol{A} \right)^{-1} \boldsymbol{A} \right) , \tag{2.34}$$

with

$$\boldsymbol{A} = \lambda_x^2 \, \boldsymbol{D}_{2,x}^\top \boldsymbol{D}_{2,x} + \lambda_y^2 \, \boldsymbol{D}_{2,y}^\top \boldsymbol{D}_{2,y} . \tag{2.35}$$

2.5 Test Surfaces

For testing surface reconstruction methods, test surfaces and their gradients are needed. An advantage of analytical surfaces is that the reconstruction can be performed on the analytical derivatives evaluated on a discrete grid (Harker & O'Leary, 2015). For non-analytical surfaces the gradient needs to be computed numerically.

a) *cos2* analytical surface.

b) *g2sTestSurf* analytical surface.

c) *ramppeaks* non-analytical surface.

d) *sin2* analytical surface.

e) *tent* surface.
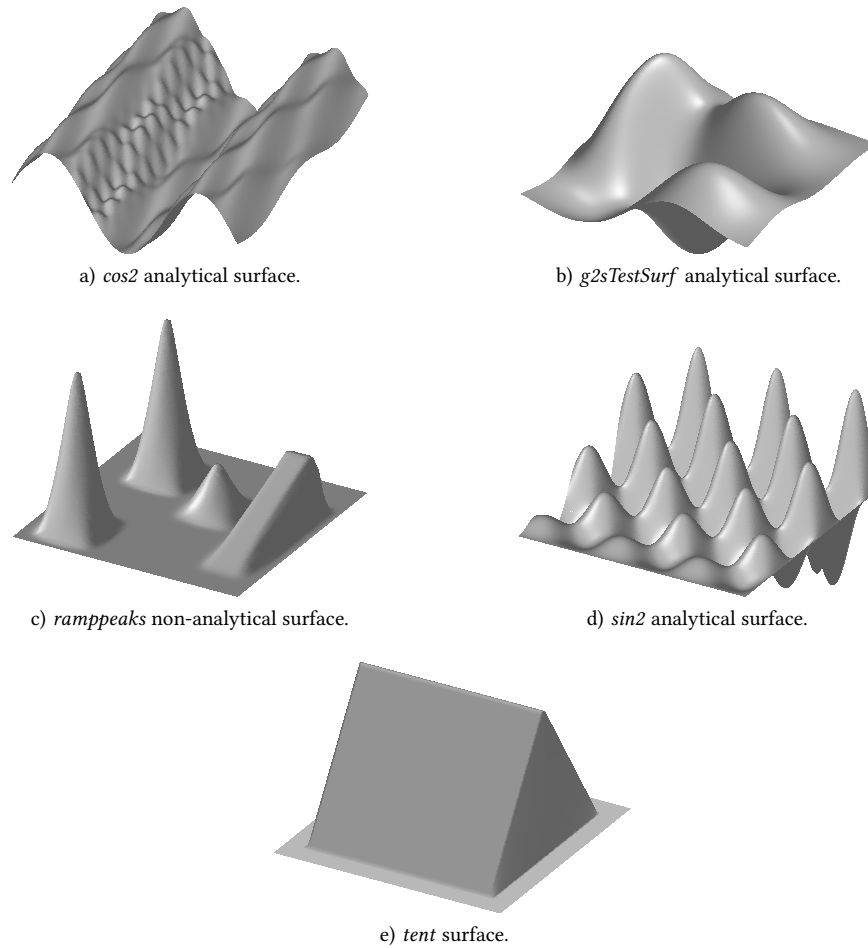
Figure 2.6 | Different Test Surfaces with Unique Features for Gradient-Based Surface Reconstruction. *cos2* has small-scale and large-scale structures. Harker and O'Leary (2013) introduced *g2sTestSurf*, which is a smooth, analytical, and non-polynomial surface. *ramppeaks* has periodic boundaries and steep peaks. It is a benchmark surface used in many publications, e.g., Agrawal, Raskar, and Chellappa (2006) and Badri, Yahia, and Aboutajdine (2014). *sin2* has some periodicity. *tent* contains depth discontinuities.

Figure 2.6 shows the test surfaces used in this thesis. *cos2*, *g2sTestSurf* and *sin2* are analytical *m*-by-*n* surfaces. For more information see Appendix B. *ramppeaks* is a non-analytical 64-by-64 surface. *tent* is a 256-by-256 surface with depth discontinuities.

2.6 Differentiation

Numerical derivatives are needed for calculating the gradients of non-analytical test surfaces. Since the reconstruction quality depends on the gradient fields, as accurate formulas as possible are needed. Some reconstruction methods need numerical differentiation also. The derivative of the function $f(x)$ at x_0 is

$$f'(x_0) = f_x(x_0) = \lim_{h \to 0} \frac{f(x_0 + h) - f(x_0)}{h} \, . \tag{2.36}$$

An obvious way to generate an approximation to $f'(x_0)$ is to simply compute

$$f'(x_0) \approx \frac{f(x_0 + h) - f(x_0)}{h} \tag{2.37}$$

for small values of $h \in \mathbb{R}$. For positive values of h this formula is known as forward-difference formula and is not very successful due to the round-off error (Burden & Faires, 2011). The most common formulas involve three and five evaluation points with even spacing h (Burden & Faires, 2011; Harker & O'Leary, 2015):

Three-Point Formulas

$$f'(x_0) = \frac{-3 f(x_0) + 4 f(x_0 + h) - f(x_0 + 2h)}{2h} \qquad \text{endpoint} \tag{2.38}$$

$$f'(x_0) = \frac{f(x_0 + h) - f(x_0 - h)}{2h} \qquad \text{midpoint} \tag{2.39}$$

Left-endpoint: $h > 0$. Right-endpoint: replace h with $-h$.

For a sequence $\{x_0, x_1, x_2, x_3\}$ of four equidistant points with spacing h the three-point formulas can be written in matrix form as (Harker & O'Leary, 2015)

$$\begin{pmatrix} f'(x_0) \\ f'(x_1) \\ f'(x_2) \\ f'(x_3) \end{pmatrix} = \frac{1}{2h} \begin{pmatrix} -3 & 4 & -1 & 0 \\ -1 & 0 & 1 & 0 \\ 0 & -1 & 0 & 1 \\ 0 & 1 & -4 & 3 \end{pmatrix} \cdot \begin{pmatrix} f(x_0) \\ f(x_1) \\ f(x_2) \\ f(x_3) \end{pmatrix} \qquad \Leftrightarrow \qquad \mathbf{y}' = \mathbf{D}\mathbf{y} \tag{2.40}$$

and similarly for five-point formulas. $\mathbf{D}$ is a differentiation matrix.

Gradients

The numerical gradient of $Z \in \mathbb{R}^{m \times n}$ can be calculated as

$$Z_x = Z \, \mathbf{D}_x^\top \, , \tag{2.41}$$
$$Z_y = \mathbf{D}_y \, Z \, , \tag{2.42}$$

where the differentiation matrix $\mathbf{D}_x \in \mathbb{R}^{n \times n}$ is transposed for the differentiation in x-direction. The differentiation matrices $\mathbf{D}_y \in \mathbb{R}^{m \times m}$, for the differentiation in y-direction, and $\mathbf{D}_x$ are equal for $h_x = h_y$ and $m = n$. Sparse differentiation matrices can be set up with *gradOp*. MATLAB's *gradient* uses three-point formulas for midpoints but only forward-differences at endpoints.

Splines

With an extension of Eq. 2.22 to tensor product cardinal B-splines the derivatives of surfaces can also be estimated:

$$h_x \operatorname{vec}\left(Z_x\right) = \left(B_x' \otimes B_y\right) \alpha_x = C_x \, \alpha_x \, , \quad \alpha_x = \left(D_{1,n_x} \otimes I_{n_y}\right)\alpha = D_{1,x} \, \alpha \, , \tag{2.43}$$
$$h_y \operatorname{vec}\left(Z_y\right) = \left(B_x \otimes B_y'\right) \alpha_y = C_y \, \alpha_y \, , \quad \alpha_y = \left(I_{n_x} \otimes D_{1,n_y}\right)\alpha = D_{1,y} \, \alpha \, . \tag{2.44}$$

The tensor product basis matrices C_x and C_y for the derivatives have to be calculated. One more knot is needed for the 1-D B-spline basis matrices B_x' and B_y' of the derivatives since the derivatives should have the same size of the surface: $t_0 = t_1 - h$ with the knot seperations h_x and h_y in the related dimensions. Furthermore, the first-order differences matrices $D_{1,n_x} \in \mathbb{R}^{n_x+1 \times n_x}$ and $D_{1,n_y} \in \mathbb{R}^{n_y+1 \times n_y}$ are needed:

$$D_1 = D_{1,n} = \begin{pmatrix} 0 & 0 & 0 & 0 & \dots & 0 & 0 & 0 \\ -1 & 1 & 0 & 0 & \dots & 0 & 0 & 0 \\ 0 & -1 & 1 & 0 & \dots & 0 & 0 & 0 \\ \vdots & \vdots & \vdots & \vdots & \vdots & \vdots & \vdots & \vdots \\ 0 & 0 & 0 & 0 & \dots & 0 & -1 & 1 \\ 0 & 0 & 0 & 0 & \dots & 0 & 0 & 0 \end{pmatrix} \in \mathbb{R}^{n+1 \times n} \, . \tag{2.45}$$

Using P-splines or P1-splines, the effects of noise and outliers may be reduced.

Accuracy

Table 2.1 shows the errors of the numerical derivatives in x-direction of various methods for the analytical test surfaces *cos2*, *g2sTestSurf* and *sin2*. The use of forward-differences (*gradOp* 2pt) is not recommended. MATLAB's *gradient* is closely related to the three-point formulas but at the boundaries incorrect and not as fast.

Table 2.1 │ **RMSE of Numerical Derivatives in x-direction Performed on Analytical Surfaces.** The three-point formulas are more accurate and faster than the MATLAB built-in *gradient* function. The P-spline parameters for the surface Z are: $k_x = k_y = 3$, $n_x = \frac{m}{2}$, $n_y = \frac{m}{2}$, $\lambda_x = \lambda_y = 0.001$.

Test Surface	m, n	RMSE				
		gradOp 2pt	*gradient*	*gradOp* 3pt	*gradOp* 5pt	*p_spline2*
cos2	128, 128	$1.33 \cdot 10^{-1}$	$2.07 \cdot 10^{-2}$	$1.35 \cdot 10^{-2}$	$1.00 \cdot 10^{-3}$	$4.34 \cdot 10^{-3}$
	256, 256	$8.00 \cdot 10^{-2}$	$6.56 \cdot 10^{-3}$	$3.38 \cdot 10^{-3}$	$6.63 \cdot 10^{-5}$	$3.06 \cdot 10^{-4}$
	512, 512	$5.08 \cdot 10^{-2}$	$2.16 \cdot 10^{-3}$	$8.45 \cdot 10^{-4}$	$4.20 \cdot 10^{-6}$	$3.25 \cdot 10^{-5}$
g2sTestSurf	128, 128	$5.24 \cdot 10^{-2}$	$2.05 \cdot 10^{-3}$	$1.39 \cdot 10^{-3}$	$4.52 \cdot 10^{-6}$	$5.61 \cdot 10^{-5}$
	256, 256	$3.09 \cdot 10^{-2}$	$6.34 \cdot 10^{-4}$	$3.46 \cdot 10^{-4}$	$2.76 \cdot 10^{-7}$	$6.51 \cdot 10^{-6}$
	512, 512	$1.93 \cdot 10^{-2}$	$2.06 \cdot 10^{-4}$	$8.62 \cdot 10^{-5}$	$1.70 \cdot 10^{-8}$	$7.90 \cdot 10^{-7}$
sin2	128, 128	1.16	$5.94 \cdot 10^{-2}$	$2.77 \cdot 10^{-2}$	$1.41 \cdot 10^{-4}$	$1.22 \cdot 10^{-3}$
	256, 256	$7.66 \cdot 10^{-1}$	$1.94 \cdot 10^{-2}$	$6.74 \cdot 10^{-3}$	$7.86 \cdot 10^{-6}$	$1.39 \cdot 10^{-4}$
	512, 512	$5.21 \cdot 10^{-1}$	$6.55 \cdot 10^{-3}$	$1.66 \cdot 10^{-3}$	$4.53 \cdot 10^{-7}$	$1.78 \cdot 10^{-5}$

Figure 2.7 to Figure 2.9 show numerical derivatives in the presence of noise and outliers. For noise, the P-splines can show their advantages and for outliers the P1-splines. Derivatives calculated with three-point formulas are more accurate than the ones calculated with five-point formulas since the noise propagates with more points.

## 2.7 Waves on the Water Surface

In this section a brief introduction into the theoretical description of free waves on the water surface is given. For further insights into fluid mechanics, the theory of water waves, and wave breaking, the books of Kundu and Cohen (2008), Johnson (1997), and Babanin (2011) are recommended.

2.7.1 Basics of Fluid Dynamics

Fluid dynamics deals with the flow of fluids. It describes no single particles but a body as continuum. Generally, small volumes, the fluid elements, are considered. All fluid dynamics is based on the conservation laws for mass, momentum, and energy (Kundu & Cohen, 2008).

Continuity Equation

Using Gauss's theorem, the continuity equation follows from the conservation of mass: for any volume fixed in space, the rate of change of fluid mass inside it has to be equal
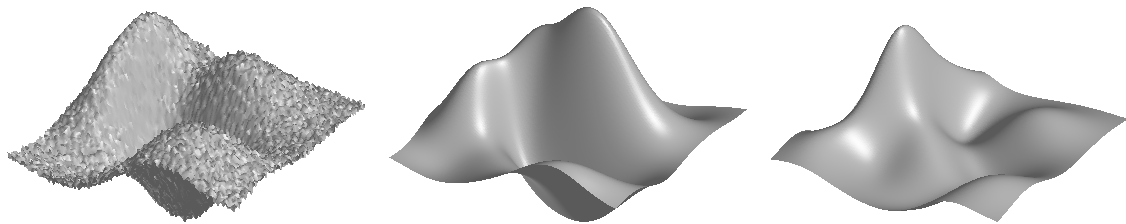
a) Corrupted 128-by-128 surface and the analytic derivatives Z_x and Z_y of the uncorrupted surface as ground truth.
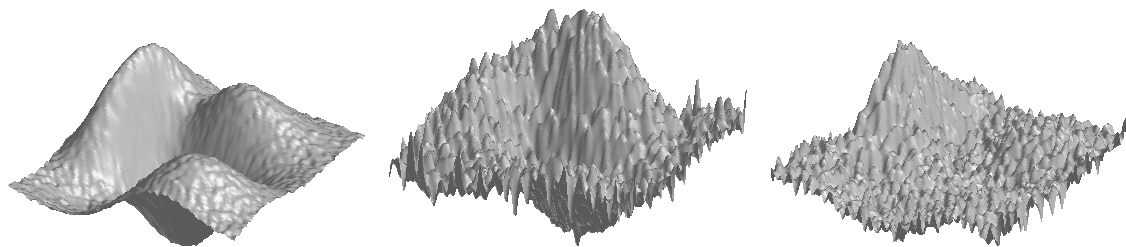
b) Binomial filter smoothed surface and its additional smoothed derivatives calculated with the three-point formulas.
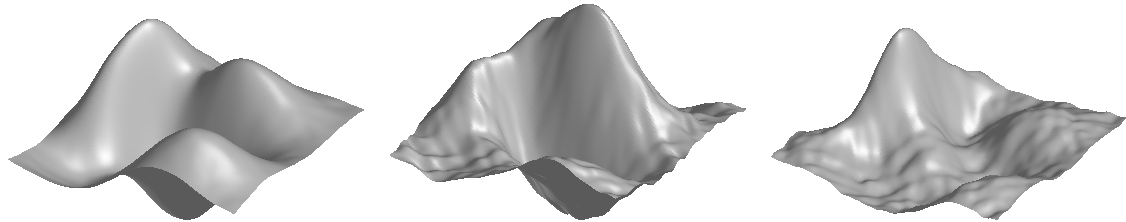
c) P-spline smoothed surface and its derivatives.

Figure 2.7 │ **Numerical Derivatives in the Presence of Gaussian Noise.** Without using a binomial filter, the derivatives calculated with *gradOp* are too noisy to see the surface structure. The amount of smoothing with a binomial filter could probably be improved. P-spline parameters for the surface Z: $k_x = k_y = 3$, $n_x = n_y = 64$, λ_x and λ_y via generalized cross-validation.

a) Corrupted surface and numerical derivatives (five-point formulas) of the uncorrupted surface as ground truth.
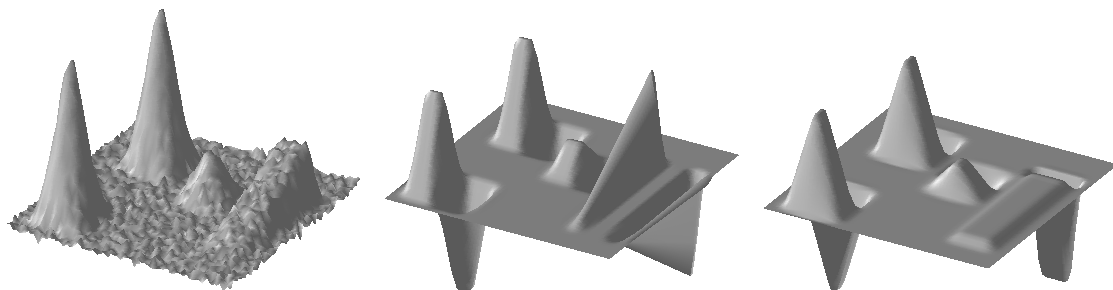

b) Binomial filter smoothed surface and its additional smoothed derivatives calculated with the three-point formulas.
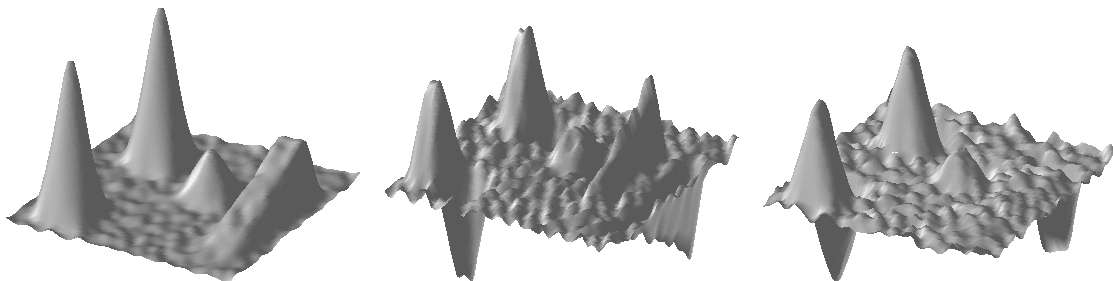
c) P-spline smoothed surface and its derivatives.

Figure 2.8 | Numerical Derivatives in the Presence of Gaussian Noise. Even for this badly sampled surface are the P-spline derivatives superior to to the common three-point formulas. This can be seen by looking at peak heights of the derivatives. P-spline parameters for the surface Z: $k_x = k_y = 3$, $n_x = n_y = 64$, λ_x and λ_y via generalized cross-validation.
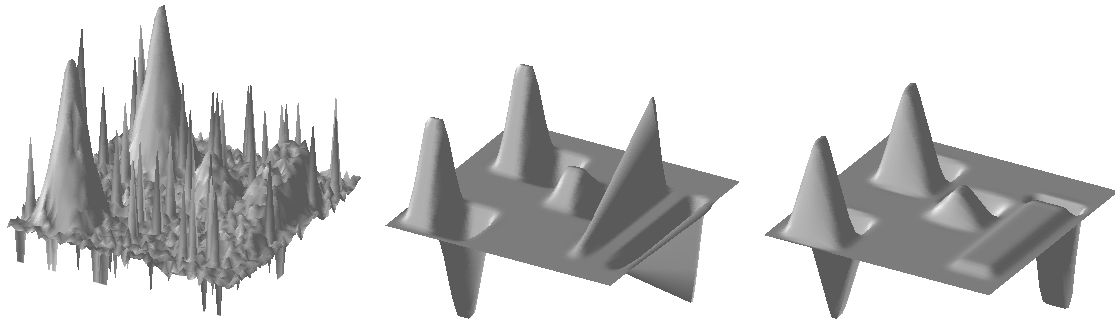
a) Corrupted surface and numerical derivatives (five-point formulas) of the uncorrupted surface as ground truth.
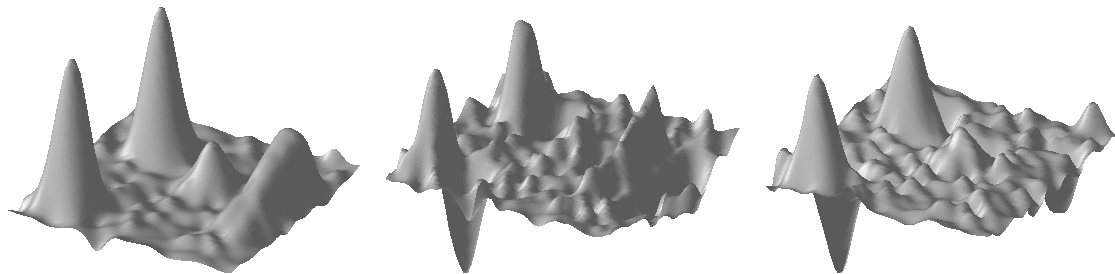
b) P-spline smoothed surface and its derivatives.
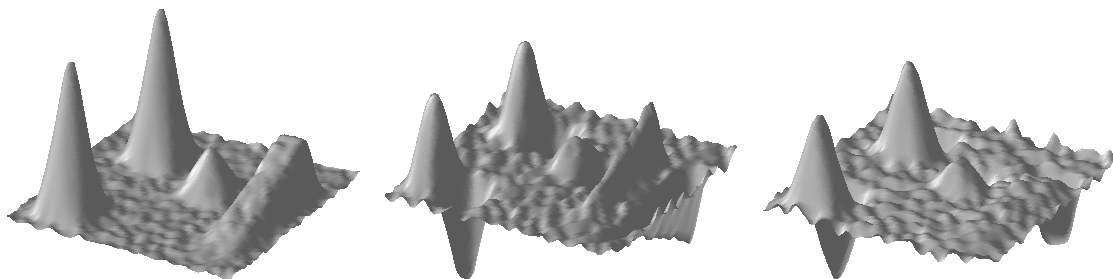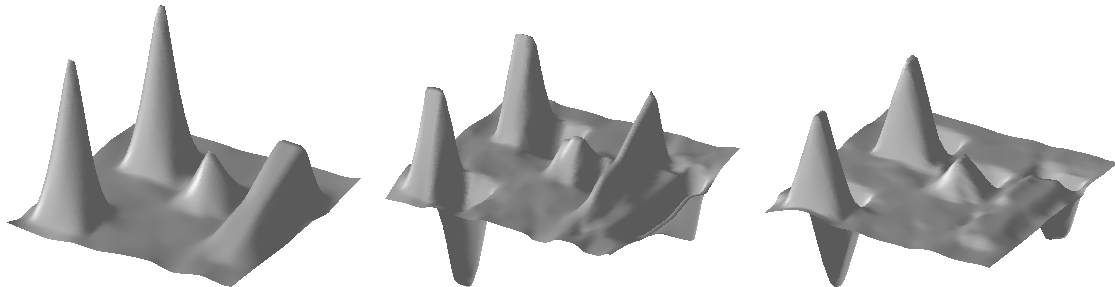

c) P1-spline smoothed surface and its derivatives.

Figure 2.9 | Numerical Derivatives in the Presence of Gaussian Noise and Outliers. The P1-splines are expectedly superior to the P-splines. P-spline parameters for the surface Z: $k_x = k_y = 3$, $n_x = n_y = 64$, λ_x and λ_y via generalized cross-validation. P1-spline parameters for the surface Z: $k_x = k_y = 3$, $n_x = n_y = 64$, λ_x and λ_y are half of the values for the P-splines.

to the net rate of fluid flow into it. For incompressible fluids the continuity equation in differential form becomes (Kundu & Cohen, 2008)

$$\boldsymbol{\nabla} \cdot \boldsymbol{u} = 0 \, , \tag{2.46}$$

where $\boldsymbol{u}$ is the velocity of the fluid.

Navier-Stokes Equations

The Navier-Stokes equations result from the conservation of momentum: the net force on a moving fluid element must equal the product of the element's mass and acceleration. For incompressible fluids and neglecting the Coriolis term, the Navier-Stokes equations are (Kundu & Cohen, 2008)

$$\varrho \, \partial_t \boldsymbol{u} + \varrho \, (\boldsymbol{u} \cdot \boldsymbol{\nabla}) \, \boldsymbol{u} = -\boldsymbol{\nabla} p + \varrho \, \boldsymbol{g} + \mu \, \nabla^2 \boldsymbol{u} \, , \tag{2.47}$$

where ϱ is the density of the fluid, p the pressure, μ the dynamic viscosity, and $\boldsymbol{g}$ the gravitational acceleration. The Navier-Stokes equations are non-linear.

2.7.2 Linear Water Waves

The non-linearity of the Navier-Stokes equations can be neglected for water waves with $a/H \ll 1$ and $a/\lambda \ll 1$, where H is the depth of water and a the amplitude of the wave with wavelength λ (Johnson, 1997; Kundu & Cohen, 2008). The dispersion relation for irrotational, inviscid flow in this linear approximation is given by (Kundu & Cohen, 2008)

$$c = \frac{\omega}{k} = \sqrt{\left(\frac{g}{k} + \frac{\sigma k}{\varrho} \right) \tanh k H} \, . \tag{2.48}$$

c is called the phase speed, ω is the circular frequency, and k is the wavenumber. Particle paths in this linear approximation are elliptical orbits.

2.7.3 Stokes Waves

A consequence of the linear wave theory is that waves of arbitrary shape propagate unchanged in form, if the system is non-dispersive (Kundu & Cohen, 2008). This changes if finite amplitude effects are considered. Stokes waves are periodic finite-amplitude irrotational waves in deep water. The phase speed of them is (Kundu & Cohen, 2008)

$$c = \sqrt{\frac{g}{k} \left(1 + k^2 \, a^2 \right)} \, . \tag{2.49}$$

Stokes waves have a flattened trough and a peaked crest. Attempting to generate waves of larger amplitude than the maximum possible at a 120° crest angle results in the appearance of foam. Particle do no longer move on closed orbits, but undergo a slow drift, the Stokes drift.

2.7.4 Wave Nomenclature

Breaking Waves

When a wave collapses, its shape becomes singular at least at some points along the wave profile. This stage of wave subsistence is called breaking (Babanin, 2011). Simply said, a portion of the fluid at the wave crest overtakes the wave itself.

Wave Breaking is an intermittent random and, compared to other processes in the wave system, very fast process (Babanin, 2011). It is the most significant sink for wave energy (Babanin, 2011). Slowly under wind action and through non-linear transfer over thousands of wave periods accumulated wave energy is suddenly released in the space of less than one period. Wave breaking is a highly non-linear mechanism. Waves do not always generate whitecaps or bubbles when they break (i.e. microscale breaking).

Capillary Waves

Wavelengths $\lambda < 4\,\text{mm}$ are dominated by surface tension. An exact solution for the phase speed of these pure capillary waves is (Crapper, 1957)

$$c = \sqrt{\frac{k\,\sigma}{\varrho}\left(1 + \frac{a^2\,k^2}{16}\right)^{-1/2}} . \tag{2.50}$$

Crapper waves have round crests and narrow troughs. They can easily be noticed as a train of parasitic capillary waves near the crest on the leeward side of gravity waves.

Gravity Waves

If weight is the restoring force of waves, these waves are called gravity waves. In gravity waves particle motions can have components along and perpendicular to the direction of propagation (Kundu & Cohen, 2008).

Microscale Breaking

When breaking, short waves do not generate whitecaps or bubbles. They lose their energy directly to the turbulence (Babanin, 2011). Microscale breaking occurs at low wind speeds and enhances air-sea heat and gas transfer significantly (Zappa et al., 2004).

Methods of Measurement 3

There are various optical methods for measuring the gradient of a surface. Among other things, it depends on the surface photometry which methods are applicable. Classical methods are shape from shading and photometric stereo. For transparent, specular reflecting surfaces imaging slope gauges may be used in laboratory measurements.

3.1 Shape from Shading

Shape from shading techniques estimate surface normals from the gradual variation of shading in a single image. Knowledge of surface photometry and the position of the light source is needed (B. K. P. Horn, 1970). Unknown light source directions can be estimated iteratively (Brooks & Horn, 1985). R. Zhang, Tsai, Cryer, and Shah (1999) give a survey of shape from shading algorithms.

Generally, the image brightness depends on the angle of incidence and on the angle of reflectance (Jähne et al., 1994). The simplest case is a so-called Lambertian surface, which diffuses light isotropically in all directions. Then the image irradiance depends only on the angle of incidence. However, real surfaces may not be Lambertian. Either advanced reflection models for estimating the surface normals or robust surface reconstruction methods are needed for accurate reconstructions.

The principal difficulty involved in shape from shading techniques is that a 2-D vector quantity, the surface gradient, is mapped onto a scalar quantity, the image irradiance (Jähne et al., 1994). Therefore, these techniques are underdetermined for all surface slopes except certain points in the gradient space. In computer vision additional constraints, such as global smoothness, are applied to produce a unique solution. Such constraints are not appropriate for the reconstruction of the ocean surface (Jähne et al., 1994).

3.2 Photometric Stereo

Using several images taken from the same position but with changed lighting directions provides additional information (Woodham, 1980). This so-called photometric stereo approach allows the determination of surface orientation at each image point. There

is no correspondence problem since the imaging geometry is not changed (Woodham, 1980). Photometric stereo works best on smooth surfaces with few discontinuities, whereas traditional stereo works well on rough surfaces (Woodham, 1980). For fractional specularly reflecting surfaces, distributed light sources and adapted algorithms can be used (Ikeuchi, 1981).

3.3 Shape from Reflection of a Specular Surface

Shape from shading and photometric stereo have mainly been developed for diffuse opaque surfaces (Jähne et al., 1994). However, the ocean surface is transparent and has a specularly reflecting surface. Using point light sources, no continuous wave slope imaging is possible. The image would only contain specular reflexes when the reflection condition is met. Thus, an extended light source is required.

A possible setup uses an extended light source and a camera looking in vertical direction to the water surface (Jähne et al., 1994): the light source emits light isotropically but the radiance depends on the position of the light source. Thus, the position of the incident ray from the extended light source depends on the wave slope. However, such a shape from reflection technique works only well for a rather narrow slope range (Jähne et al., 1994). One practical reason for this limitation is the needed large light source diameter. Another disadvantage is the low reflectivity of water surfaces at low and moderate incidence angles.

3.4 Imaging Slope Gauge

So far, the described methods are of little use for wave imaging at the specular water surface (Jähne et al., 1994). The imaging slope gauge (ISG) is a shape from refraction based technique. In contrast to shape from reflection, the ratio of emitted and received light is by far larger. Theoretical considerations about refraction show that it is advantageous to use a system with a light source below the water surface and the camera above (Jähne et al., 1994). Otherwise, non-linearities due to the optical geometry are much larger. Additionally, the maximum measurable slope would be limited by total reflection.

The setup of the imaging slope gauge used in the wind-wave facility Aeolotron in Heidelberg is shown in Figure 3.1. A detailed description of measurement principle, calibration, and characterization of that ISG is given in Kiefhaber, Reith, Rocholz, and Jähne (2014) and Reith (2014). An object-space telecentric setup is used. This guarantees a constant magnification factor independent of water surface height. Only refracted light rays that are orthogonal to the mean water surface reach the camera.

A Fresnel lens below the water body is used to guarantee telecentric illumination. The light source is placed in the focal plane of that lens. So, water surface slopes are connected to a unique illumination screen position. The dependence of the position on
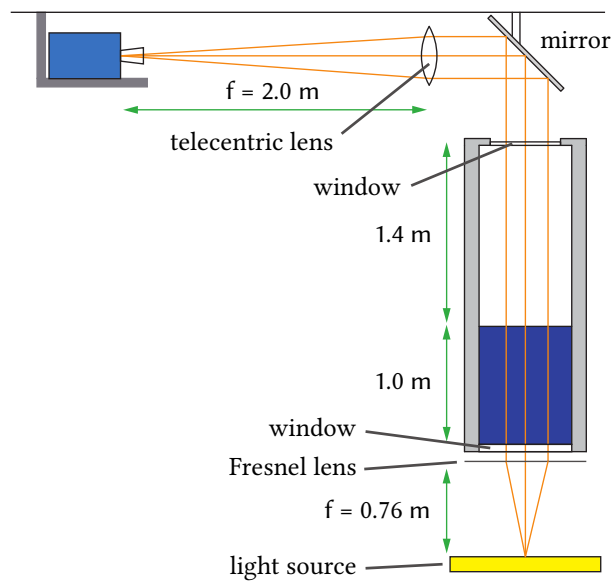
Figure 3.1 | Imaging Slope Gauge Setup at the Wind-Wave Facility Aeolotron in Heidelberg. A high-speed camera observes the water surface from above. The water body is illuminated from below with a programmable high power LED light source. The light is refracted at the water surface. Source: Kiefhaber, Reith, Rocholz, and Jähne (2014).

the light source on surface slope is almost linear (Jähne et al., 1994). The ray geometry is shown in Figure 3.2. Using an appropriate illumination design, the slopes of the water surface can be estimated.

Characteristics of the ISG in the Aeolotron

Using a light source with a gradient in one direction, only one slope component in that direction can be measured (Kiefhaber et al., 2014). The imaging slope gauge in the Aeolotron uses four brightness gradients consecutively. So, slopes in both directions can be measured, lens effects can be corrected, and demands to the homogeneity of the light source can be reduced (Kiefhaber et al., 2014). The final slope data are estimated from four raw images corresponding to the four brightness gradients.

The imaging slope gauge is calibrated using a calibration target with known slopes (Reith, 2014). This calibration step provides a lookup table. In the slope calculation step the lookup table is applied to pre-processed raw images (Reith, 2014).

The camera is a pco.dimax high-speed camera. The raw data frame rate of the ISG data used in this thesis is 6030 fps. The effective frame rate is 1507.5 fps. The spatial resolution of 760×930 pixels corresponds to a water surface area of 175 mm × 214 mm. Slopes up to 26.3° in the alongwind and 19.6° in the crosswind direction can be measured with the setup in the Aeolotron (Kiefhaber et al., 2014). The measurable slope range depends on the size of the light source.
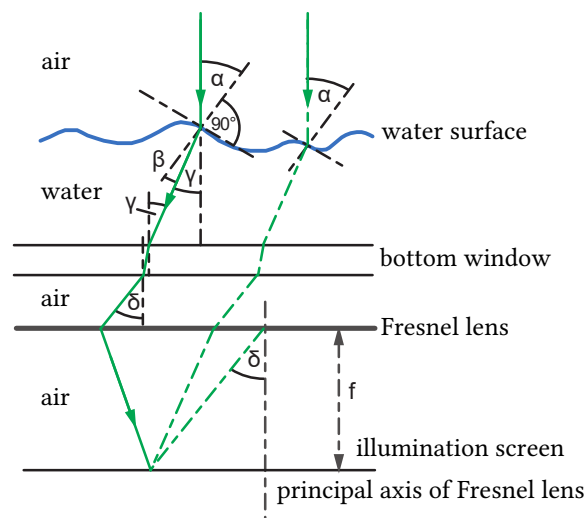
Figure 3.2 | Ray Geometry of the Imaging Slope Gauge. Shown are the reversed light paths. All rays that leave the water at an angle δ to the vertical are focused onto the same position on the illumination screen. Source: Kiefhaber, Reith, Rocholz, and Jähne (2014).

Reconstruction Methods 4

For comfort reasons, the separations of grid points in x- and y-direction are set to one for the rest of this thesis: $h_x = h_y = 1$. The result is a clearer representation of the equations. Virtually there is no problem in doing this. Due to the disadvantages of local integration techniques, the focus in this thesis lies on global integration techniques. The chosen methods are reflected in chronological order with new methods at the end.

Some methods and their implementations are based on the forward-difference formula. They achieve higher accuracy performing on with forward-differences calculated gradient fields, as surface normal integration is the inverse process to differentiation. Performing on analytical or on higher order numerically calculated gradient fields, these methods are inferior to other methods because of a shift in the xy-plane: the surface sampling points z_{ij} and the gradient field sampling points p_{ij} and q_{ij} are shifted by half a pixel. If the forward-difference formula shall be used, a shift has to be applied to the gradient field to avoid the shift of the reconstructed surface z (e.g., Quéau & Durou, 2015):

$$\tilde{p}_{i,j} = \frac{p_{i,j+1} + p_{i,j}}{2} \qquad \text{and} \qquad \tilde{q}_{i,j} = \frac{q_{i+1,j} + q_{i,j}}{2} \ . \tag{4.1}$$

That means also a small smoothing of the gradient field. Real-world gradient fields should not rely on forward-differences. Thus, the superiority of those methods is an erroneous belief resulting from working with the benchmark *ramppeaks* surface with forward-differences derivatives. In this case the shifts of the given field and of the reconstruction cancel each other for those methods.

4.1 Frankot and Chellappa (1988)

Frankot and Chellappa (1988) stated that it is a reasonable constraint to enforce the integrability of the surface slopes (zero-curl condition):

$$z_{xy} = z_{yx} \ . \tag{4.2}$$

As a result, the surface z is independent of the path of integration and smoothed since in the case of depth discontinuities the integrability condition is not fulfilled.

One way to enforce the integrability condition Eq. 4.2 is to project the given possibly non-integrable gradient field components, p and q, onto a set of integrable surface slopes, z_x and z_y, and to minimize

$$S = \iint \left[\left| z_x - p \right|^2 + \left| z_y - q \right|^2 \right] \mathrm{d}x \, \mathrm{d}y \,. \tag{4.3}$$

Goal is to find the integrable surface slopes set which is closest to the given gradient field. The integrable surface slopes are represented by a finite set of integrable basis functions, each satisfying Eq. 4.2. Usually, the use of Fourier basis functions is meant by the method of Frankot and Chellappa (1988).

Minimization of the functional S in the Fourier space, e.g., in Wei and Klette (2001), yields as optimal solution in sense of Eq. 4.3:

$$z = \mathcal{F}^{-1} \left(-i \, \frac{k_x \, \mathcal{F}(p) + k_y \, \mathcal{F}(q)}{k_x^2 + k_y^2} \right) \,, \text{ with } \mathcal{F}(f) = \iint f(x, y) \, \mathrm{e}^{-i \, (k_x x + k_y y)} \, \mathrm{d}x \, \mathrm{d}y \,. \tag{4.4}$$

$\mathcal{F}$ and $\mathcal{F}^{-1}$ denote the Fourier transform and its inverse. Eq. 4.4 is not valid at the point $\boldsymbol{k} = (0, 0)$ in the Fourier space. This simply means that there is no information about the integration constant or mean surface height. The discretization is done using fast Fourier transforms allowing very efficient surface reconstruction.

The method of Frankot and Chellappa (1988) can generally not handle non-regular domains since the Fourier transform weights every data point equal. Thus, possible gaps in the data have to be closed before applying this method.

Implementations

The implementation of Agrawal, *fc_agrawal*, is erroneous in the wavenumbers. Additionally, this implementation cannot handle mean slopes. The frequent use of *fc_agrawal* in literature for comparing with new methods can simply be recognized by some wiggles in the reconstructed surface and characteristic residuals.

fc_ISG can handle mean slopes with a workaround (Rocholz, 2008). Figure 4.1 shows that there are still problems with non-periodic boundaries. Boundary integration errors mainly occur because of discontinuities obtained with discrete Fourier transform routines (Bon, Monneret, & Wattellier, 2012). Discrete Fourier transforms periodize the reconstructed surface artificially[1]. An embedding of the surface $\boldsymbol{Z}$ such that it is perfectly even, and its derivatives odd, solves this problem (Bon et al., 2012).

The implementation of Xiong, *fc_xiong*, embeds the surface $\boldsymbol{Z}$ and the gradient field components $\boldsymbol{P}$ and $\boldsymbol{Q}$ correctly. The reconstruction is then simply the relevant section of

---

[1]Balschbach (2000) deals with non-periodic boundaries by mirroring the gradient field. Rocholz (2008) recommends not to do this. Since then *fc_ISG* seems to be used for ISG data without mirroring.

a) Ground truth surfaces.

b) Surfaces reconstructed with *fc_agrawal*.

c) Surfaces reconstructed with *fc_ISG*.

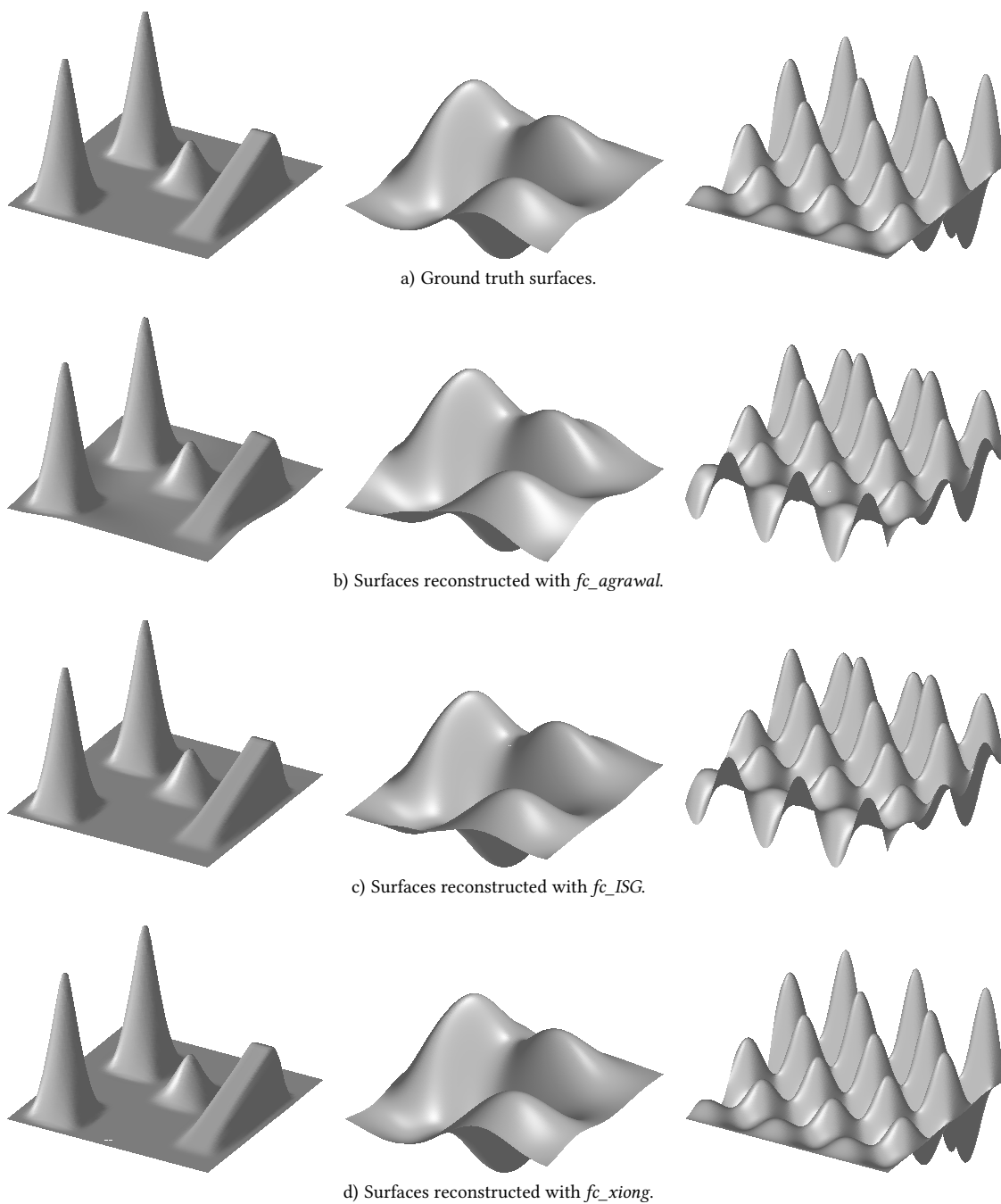d) Surfaces reconstructed with *fc_xiong*.

Figure 4.1 | Comparison of Different Implementations Based on Frankot and Chellappa (1988) in the Absence of Noise and Outliers. Only the implementation *fc_xiong* can handle non-periodic boundary conditions. Unfortunately the implementation *fc_agrawal* is often used in literature to compare with new methods, e.g., in Harker and O'Leary (2015) how the residuals show.

the solution of Eq. 4.4 for the embedded gradient field components. A workaround to reconstruct mean slopes such as for *fc_ISG* is not needed.

4.2 Simchony, Chellappa, and Shao (1990)

Minimization of the functional S in Eq. 4.3 with the calculus of variations yields a Poisson equation:

$$\Delta z = \partial_x p + \partial_y q =: f \ .$$

$$(4.5)$$

Simchony et al. (1990) discussed a way of solving Poisson equations on a rectangular domain using fast orthogonal transforms. The discretization of the Laplacian yields

$$\left(z_{i-1,j} - 2z_{i,j} + z_{i+1,j} \right) + \left(z_{i,j-1} - 2z_{i,j} + z_{i,j+1} \right) = f_{ij}^* \ .$$

$$(4.6)$$

$\boldsymbol{F}^*$ is the discretized function f modified for boundary conditions. In the absence of a boundary condition, the natural Neumann boundary condition

$$(\boldsymbol{\nabla} z - \boldsymbol{g}) \cdot \boldsymbol{\eta} = 0 \ ,$$

$$(4.7)$$

where $\boldsymbol{\eta}$ is the outer unit-length normal to the boundary in the image plane, has to be considered (Quéau & Durou, 2015; Quéau, Durou, & Aujol, 2017). In case of Neumann boundary conditions, the surface may be obtained using the discrete cosine transform $\mathscr{C}$ and its inverse transform $\mathscr{C}^{-1}$ (Quéau et al., 2017):

$$\boldsymbol{Z} = \mathscr{C}^{-1} \left(\frac{-\mathscr{C}\left(\boldsymbol{F}^*\right)}{4 \, \sin^2 \frac{k_x}{2} + 4 \, \sin^2 \frac{k_y}{2}} \right) \ .$$

$$(4.8)$$

The solution is very sensible to the choice of a boundary condition, including the natural boundary condition when only $\boldsymbol{g}$ is known, resulting in great differences in the reconstructed surfaces (Quéau et al., 2017). This is due to the fact that any harmonic function may be added to a solution of the Poisson equation to obtain a different solution satisfying the Poisson equation.

Implementations

The implementation of Agrawal, *scs_agrawal*, uses forward-differences for the calculation of $\boldsymbol{F}$ and is thereby totally based on forward-differences. The implementation of Queau, *scs_queau*, uses three-point formulas and the natural Neumann boundary condition. The new implementation *scs* is based on *scs_queau* but uses slightly modified boundary conditions and a surface embedding such as described in the section before.

Table 4.1 | RMSE of Different Implementations Based on Simchony et al. (1990). The test surfaces are analytical 256-by-256 surfaces. In addition the implementations are compared with *fc_xiong*. σ is the standard deviation of the Gaussian noise added to the gradient fields.

Test Surface	$\sigma\left[\|\boldsymbol{g}\|_\infty\right]$	RMSE			
		scs_queau	*scs*	*scs_agrawal*	*fc_xiong*
g2sTestSurf	-	$9.45 \cdot 10^{-3}$	$4.62 \cdot 10^{-3}$	$2.54 \cdot 10^{-2}$	$3.11 \cdot 10^{-4}$
	5 %	$\approx 1.1 \cdot 10^{-2}$	$\approx 9.6 \cdot 10^{-3}$	$\approx 2.8 \cdot 10^{-2}$	$\approx 9.1 \cdot 10^{-3}$
sin2	-	$6.85 \cdot 10^{-1}$	$9.31 \cdot 10^{-2}$	$2.05 \cdot 10^{-1}$	$9.23 \cdot 10^{-3}$
	5 %	$\approx 6.8 \cdot 10^{-1}$	$\approx 1.3 \cdot 10^{-1}$	$\approx 2.2 \cdot 10^{-1}$	$\approx 9.9 \cdot 10^{-2}$

Table 4.1 shows the accuracy of the different implementations. Obviously the new implementation is an improvement but not as good as a proper implementation of the method of Frankot and Chellappa (1988). In contrast, Quéau et al. (2017) state that the method of Simchony et al. (1990) improves the method of Frankot and Chellappa (1988) a lot. Even the new implementation's errors show patterns at one boundary. So, a further improvement may be possible.

The method of Simchony et al. (1990) cannot handle gaps in the gradient data and non-rectangular domains. Since the discrete cosine transform is implemented with fast Fourier transform, the method is also computationally efficient.

4.3 Wei and Klette (2001, 2002)

Wei and Klette (2001) added a constraint to the functional in Eq. 4.3 to improve the accuracy and robustness, and to reflect the relations among z, p, and q more effectively:

$$S = \iint \left[\left|z_x - p\right|^2 + \left|z_y - q\right|^2 + \lambda \left(\left|z_{xx} - p_x\right|^2 + \left|z_{yy} - z_y\right|^2 \right) \right] \mathrm{d}x\,\mathrm{d}y \,. \tag{4.9}$$

λ is a positive parameter. Minimization in the Fourier space yields

$$z = \mathscr{F}^{-1} \left(-i\, \frac{\left(k_x + \lambda\, k_x^3\right) \mathscr{F}(p) + \left(k_y + \lambda\, k_y^3\right) \mathscr{F}(q)}{k_x^2 + k_y^2 + \lambda \left(k_x^4 + k_y^4\right)} \right) \,. \tag{4.10}$$

The method of Frankot and Chellappa (1988) appears as a limit, but no λ with an improvement could be found. The method is implemented with *wei*. Of course an embedding of $\boldsymbol{Z}$, $\boldsymbol{P}$ and $\boldsymbol{Q}$ such as described in section 4.1 is needed to avoid boundary effects.

Wei and Klette (2002) did another modification of the functional and combined the integrability constraint, a small deflection approximation of the surface area, and a small
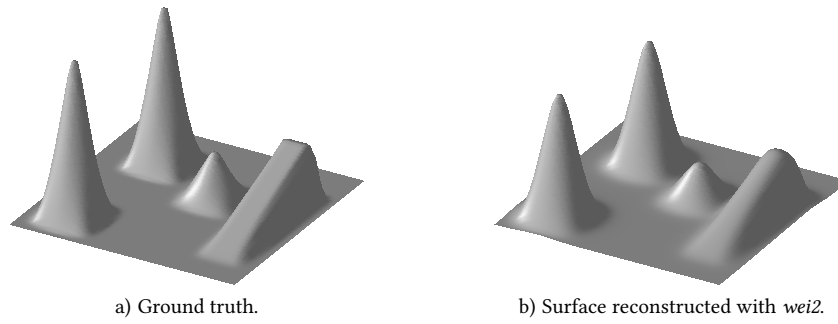
a) Ground truth.　　　　　　　　b) Surface reconstructed with *wei2*.

Figure 4.2 | Surface Reconstruction Based on Wei and Klette (2002). The amount of smoothing increases with μ. λ is set to zero since it only degrades the solution.

deflection approximation of the surface curvature. The modification should again reflect the relations among z, p, and q more effectively:

$$
\begin{aligned}
S = \iint \left[\left| z_x - p \right|^2 + \left| z_y - q \right|^2 \right] \mathrm{d}x\, \mathrm{d}y + \lambda \iint \left[\left| z_x \right|^2 + \left| z_y \right|^2 \right] \mathrm{d}x\, \mathrm{d}y \\
+ \mu \iint \left[\left| z_{xx} \right|^2 + 2 \left| z_{xy} \right|^2 + \left| z_{yy} \right|^2 \right] \mathrm{d}x\, \mathrm{d}y \,.
\end{aligned}
\tag{4.11}
$$

λ and μ are positive parameters. Minimization in the Fourier space yields

$$
z = \mathscr{F}^{-1} \left(-i\, \frac{k_x\, \mathscr{F}(p) + k_y\, \mathscr{F}(q)}{(1 + \lambda)\left(k_x^2 + k_y^2 \right) + \mu \left(k_x^2 + k_y^2 \right)^2} \right) \,.
$$

Again, the method of Frankot and Chellappa (1988) is a limit and no parameter $\lambda > 0$ with an improvement could be found. Figure 4.2 demonstrates that the parameter μ works as a smoothing parameter. The optimal parameter μ depends on the surface and on the noise level. The gain is rather small and is at the cost of the search for a good parameter μ. *wei2* is an implementation of this method.

Since the methods of Wei and Klette (2001) and Wei and Klette (2002) are modifications of the methods of Frankot and Chellappa (1988), they cannot handle non-rectangular domains and are numerically efficient.

4.4 Agrawal, Raskar, and Chellappa (2006)

Agrawal, Raskar, and Chellappa (2006) proposed a generalized framework to represent a continuum of surface reconstruction methods from a given non-integrable gradient field. The methods differ in the choice of weights basically. All of the new proposed methods and available implementations are totally based on forward-differences with all the disadvantages using them on real-world data.

M-estimators

M-estimators can be formulated as an iterative re-weighted solution to the functional

$$S = \iint \left[w_x \left| z_x - p \right|^2 + w_y \left| z_y - q \right|^2 \right] \mathrm{d}x \, \mathrm{d}y \, . \tag{4.12}$$

The weights w_x and w_y at iteration k depend on the residual at iteration $k - 1$ using a symmetric, positive-definite function with a unique minimum at zero, and an increase less than square. Minimization yields the associated Euler-Lagrange equation

$$\partial_x \, w_x \, z_x + \partial_y \, w_y \, z_y = \partial_x \, w_x \, p + \partial_y \, w_y \, q \, . \tag{4.13}$$

The effect of outliers is reduced since the weights depend on a function that increases less than square. An implementation of Agrawal, *M_estim*, is available.

Diffusion

Since anisotropic diffusion is a common approach for image restoration, Agrawal et al. (2006) generalized the Poisson equation, Eq. 4.5,

$$\boldsymbol{\nabla} \cdot \left[\boldsymbol{D} \cdot \begin{pmatrix} z_x \\ z_y \end{pmatrix} \right] = \boldsymbol{\nabla} \cdot \left[\boldsymbol{D} \cdot \begin{pmatrix} p \\ q \end{pmatrix} \right] , \qquad \text{with} \quad \boldsymbol{D} = \begin{pmatrix} d_{11}\,(x, y) & d_{12}\,(x, y) \\ d_{12}\,(x, y) & d_{22}\,(x, y) \end{pmatrix} . \tag{4.14}$$

$\boldsymbol{D}$ is a 2-by-2 symmetric, positive-definite matrix at each point, i.e., a field of diffusion tensors. The generalized Poisson equation, Eq. 4.14, is the Euler-Lagrange equation of the functional

$$S = \iint \left[d_{11} \left| z_x - p \right|^2 + 2 \, d_{12} \left| z_x - p \right| \left| z_y - q \right| + d_{22} \left| z_y - q \right|^2 \right] \mathrm{d}x \, \mathrm{d}y \, . \tag{4.15}$$

Agrawal et al. (2006) give a scheme for obtaining the diffusion tensor by convolution with a Gaussian kernel. The implementation of Agrawal, *diffusionA*, is more robust to outliers than the method of Frankot and Chellappa (1988).

4.5 Du, Robles-Kelly, and Lu (2007)

Du, Robles-Kelly, and Lu (2007) considered the functional in Eq. 4.3 as a least squares estimation method in the continuous domain (see also section 4.6). Since least squares methods are known to be sensitive to outliers, an L^1-norm based discrete functional

$$S = \sum_{i=1}^{m-1} \sum_{j=1}^{n-1} \left| z_{i,j+1} - z_{i,j} - p_{i,j} \right| + \left| z_{i+1,j} - z_{i,j} - q_{i,j} \right| \tag{4.16}$$

was used for *m*-by-*n* surfaces. The derivatives are calculated with simple forward-differences. Minimization by converting the problem into a linear program yields the surface $\boldsymbol{Z}$. An improvement of the method is presented in section 4.11.

4.6 Harker and O'Leary (2008, 2011, 2013, 2015)

Harker and O'Leary (2008, 2011, 2013, 2015) reconstructed surfaces from gradient fields using least squares methods directly. The discretization of the functional in Eq. 4.3 in a least square sense is

$$S = \left\| \boldsymbol{Z}_x - \boldsymbol{P} \right\|_F^2 + \left\| \boldsymbol{Z}_y - \boldsymbol{Q} \right\|_F^2 . \tag{4.17}$$

Using that numerical differentiation is a linear operator yields

$$S = \left\| \boldsymbol{Z} \, \mathsf{D}_x^\top - \boldsymbol{P} \right\|_F^2 + \left\| \mathsf{D}_y \, \boldsymbol{Z} - \boldsymbol{Q} \right\|_F^2 , \tag{4.18}$$

and minimization a so-called Sylvester equation:

$$\mathsf{D}_y^\top \mathsf{D}_y \, \boldsymbol{Z} + \boldsymbol{Z} \, \mathsf{D}_x^\top \mathsf{D}_x - \mathsf{D}_y^\top \boldsymbol{Q} - \boldsymbol{P} \mathsf{D}_x = 0 . \tag{4.19}$$

Sylvester equations can be solved more efficiently than the associated least squares problem for *m*-by-*n* surfaces:

$$\text{minimize} \quad f_0(\boldsymbol{Z}) = \left\| \begin{pmatrix} \mathsf{D}_x \otimes \boldsymbol{I}_m \\ \boldsymbol{I}_n \otimes \mathsf{D}_y \end{pmatrix} \text{vec}(\boldsymbol{Z}) - \begin{pmatrix} \text{vec}(\boldsymbol{P}) \\ \text{vec}(\boldsymbol{Q}) \end{pmatrix} \right\|_2^2 . \tag{4.20}$$

The problem is rank-1 deficient, meaning that the integration constant cannot be recovered. Harker and O'Leary's implementation can apply three- and five-point formula derivatives. The modification *g2s* can additionally apply forward-differences derivatives (respecting Eq. 4.1), and has slightly improved computational efficiency on regular grids.

Since the Sylvester equation defines the reconstruction problem over a rectangular domain, possible gaps in given gradient fields have to be closed before solving the equation.

Spectral Regularization

Using an incomplete set of basis functions to represent a reconstructed surface, band-pass filtering can be incorporated into the least squares approach effectively (Harker & O'Leary, 2015). The implementation *g2sSpectral* uses polynomial, cosine, or Fourier bases. Spectral regularization can damp the influence of noise on the reconstruction and smooth the surface but can also damp small-scale structures or generate artifacts such as in Figure 4.3.

a) Ground truth.   b) Surface reconstructed with *gs2Spectral*.
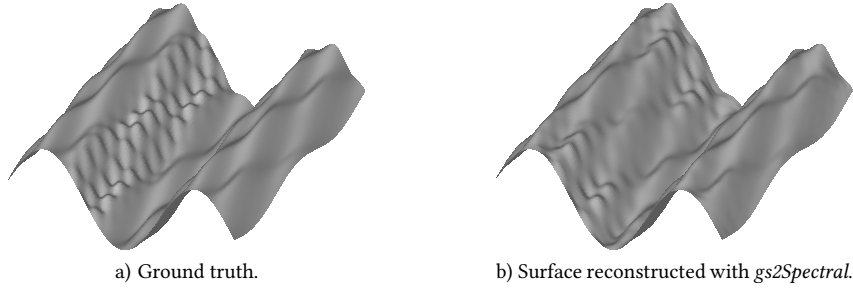
Figure 4.3 | Surface Reconstruction Based on Harker and O'Leary (2011) with Spectral Regularization in the Presence of Noise. An incomplete polynomial basis was used. The reconstruction of small-scale structures depends on the completeness of the used basis.

Tikhonov Regularization

Tikhonov regularization can not only be applied to 1-D vectors but also be modified to 2-D surfaces. One approach is to minimize (Harker & O'Leary, 2015)

$$
\begin{aligned}
S = {} & \left\| Z \mathsf{D}_x^\top - P \right\|_F^2 + \left\| \mathsf{D}_y Z - Q \right\|_F^2 \\
& + \lambda^2 \left\| \left(Z - Z_0 \right) L_x^\top \right\|_F^2 + \mu^2 \left\| L_y \left(Z - Z_0 \right) \right\|_F^2 .
\end{aligned}
\tag{4.21}
$$

Z_0 is an a-priori estimate of Z. λ and μ are the regularization parameters. L_x and L_y are operators to weight the measures of the deviations from the a-priori estimate.

4.7 Reddy, Agrawal, and Chellappa (2009)

Reddy, Agrawal, and Chellappa (2009) presented an algorithm for obtaining the surface by finding the gradient field which best fits the given corrupted gradient field in an L^1 sense. Essentially, it is a combination of the method of Du et al. (2007) and graph analogy. Unfortunately, it is also based on forward-differences without respecting Eq. 4.1.

4.8 Balzer and Mörwald (2012)

Balzer and Mörwald (2012) proposed solving the Poisson equation Eq. 4.5 numerically by isogeometric analysis, a special kind of finite-elements method that operates on B-spline patches. For a theoretical review see Balzer and Mörwald (2012). Since usual B-splines are used, the method is not robust to outliers.

Balzer's implementation *iga* can only handle image sizes which are a power of two and rectangular domains, and has two parameters to tune. Performing on perfect gradient data, this algorithm reaches very low reconstruction errors. However, working with noisy data there is no significant gain to other faster methods.

4.9 Badri, Yahia, and Aboutajdine (2014)

Badri, Yahia, and Aboutajdine (2014) proposed a new optimization method for robust surface reconstruction based on a triple sparsity prior: a double sparsity prior on the residual gradient and the surface gradients to handle gradient outliers, and a sparse prior on the surface to deal with noisy gradients and to produce smooth surfaces.

Instead of the L^1-norm, the $L^{p<1}$-norm (Hyper-Laplacian distribution) is used resulting in a highly non-convex problem:

$$\arg\min_{Z,\,Z'} \left\| \begin{pmatrix} \text{vec}\,(Z'_x - P) \\ \text{vec}\,(Z'_y - Q\,) \end{pmatrix} \right\|_{p_1}^{p_1} + \lambda_1 \left\| \begin{pmatrix} Z'_x \\ Z'_y \end{pmatrix} \right\|_{p_2}^{p_2} + \frac{\gamma}{2}\,\|\text{vec}\,(Z - Z'\,)\|_2^2 + \lambda_2 \left\| \begin{pmatrix} Z_x \\ Z_y \end{pmatrix} \right\|_{p_3}^{p_3}.$$

(4.22)

λ_1, λ_2 and γ are positive regularization parameters, Z' is an intermediate surface, and $p_1, p_2, p_3 < 1$. The problem is iteratively solved using a half-quadratic approach.

The shown reconstructed surfaces in Badri et al. (2014) are outstanding in the case of outliers. However, the parameters have to be tuned and for the iterative solution a good initialization is needed (Quéau et al., 2017). Besides the method is not a fast one. Badri and Yahia (2016) used a non-local low-rank approach to enforce integrability yielding a better reconstruction quality in extreme corruption situations.

4.10 Sevcenco, Hampton, and Agathoklis (2015)

Sevcenco, Hampton, and Agathoklis (2015) proposed an algorithm for image reconstruction from gradient data based on the Haar wavelet decomposition. How the figures 7 and 8 in Sevcenco et al. (2015) show, virtually no improvement to the method of Simchony et al. (1990) is visible in the presence of noise and outliers. Tests with the implementation *wavelets* and *scs_agrawal* performed on forward-differences derivatives could passably reproduce the relative reconstruction errors in table 1 of Sevcenco et al. (2015).

wavelets prefers the performing on forward-differences gradient fields. So the only advantage of the new method is the reduced computational complexity compared to the efficient methods of Frankot and Chellappa (1988) and Simchony et al. (1990).

4.11 Convex Optimization Based Methods

Advantages of convex optimization based methods are the conceptual simple formulation of the surface reconstruction problem as a weighted norm approximation problem and the use of efficient convex optimization solvers. Introducing weights, these methods can perform on irregular grids. No gaps in the gradient fields have to be closed at first or fields segmented into rectangular parts without gaps.

4.11.1 Least Squares Reconstruction

A modification of the method described in section 4.6 using weights is the weighted least squares problem:

$$
\text{minimize} \quad f_0(Z) = \left\| \begin{pmatrix} W \cdot (\mathsf{D}_x \otimes I_m) \\ W \cdot (I_n \otimes \mathsf{D}_y) \end{pmatrix} \text{vec}(Z) - \begin{pmatrix} \text{vec}(P) \\ \text{vec}(Q) \end{pmatrix} \right\|_2^2 . \tag{4.23}
$$

W is an mn-by-mn diagonal matrix with the weights on the diagonal. Pseudo-observations with zero weights and zero values for P and Q must be introduced to handle missing data in this notation. Weights for available data are 1. The improvement of handling non-rectangular domains is accompanied by the less efficient solving of the surface reconstruction problem. However, there is no problem in programming an algorithm which solves the weighted least squares problem if required and uses *g2s* if not.

The implementation *LSrec* uses sparse differentiation matrices and tensor products. Thus, the computation times are reasonable. If forward-differences are used, the implementation *LSrec* respects Eq. 4.1. In that case the algorithm delivers quite the same results as *discLS* implemented from Quéau (2015).

4.11.2 Least Absolute Deviations Reconstruction

Least squares solutions are not robust to outliers. Hence, in least squares surface reconstruction errors propagate, resulting in an unnatural surface even if only few gradient points are corrupted (Badri et al., 2014).

An obvious way to achieve robustness to outliers is to use an L^1-norm based method, such as Du et al. (2007) and Reddy et al. (2009) suggested. Since these methods are based on forward-differences without respecting Eq. 4.1, a modified method formulated as a L^1-norm approximation problem is presented:

$$
\text{minimize} \quad f_0(Z) = \left\| \begin{pmatrix} W \cdot (\mathsf{D}_x \otimes I_m) \\ W \cdot (I_n \otimes \mathsf{D}_y) \end{pmatrix} \text{vec}(Z) - \begin{pmatrix} \text{vec}(P) \\ \text{vec}(Q) \end{pmatrix} \right\|_1 . \tag{4.24}
$$

This problem can be solved as a linear program. As weights and zero value pseudo-observations are introduced, this method can also handle non-rectangular domains. The implementation *LADrec* respects Eq. 4.1 if forward-differences derivatives are chosen.

4.11.3 Regularized Least Absolute Deviations Reconstruction

Some regularization may be added to the least absolute deviations reconstruction approach, Eq. 4.24, to avoid artificial individual peaks in the reconstruction. These peaks occur at positions where the given gradient field is corrupted with outliers depending on the outlier magnitude.

Thus, to yield a smooth surface in presence of outliers some regularization is needed. Constraints on the surface's second derivatives similar to the ansatz of cubic smoothing splines in Eq. 2.15 but in a discrete way are chosen:

$$
\text{minimize} \quad f_0(\boldsymbol{Z}) = \left\| \begin{pmatrix} \boldsymbol{W} \cdot (\mathbf{D}_x \otimes \boldsymbol{I}_m) \\ \boldsymbol{W} \cdot (\boldsymbol{I}_n \otimes \mathbf{D}_y) \\ \lambda_x \boldsymbol{W} \cdot (\mathbf{D}_x^2 \otimes \boldsymbol{I}_m) \\ \lambda_y \boldsymbol{W} \cdot (\boldsymbol{I}_n \otimes \mathbf{D}_y^2) \end{pmatrix} \text{vec}(\boldsymbol{Z}) - \begin{pmatrix} \text{vec}(\boldsymbol{P}) \\ \text{vec}(\boldsymbol{Q}) \\ \boldsymbol{0} \\ \boldsymbol{0} \end{pmatrix} \right\|_1, \tag{4.25}
$$

with the second order differentiation matrices $\mathbf{D}_x^2 = \mathbf{D}_x \mathbf{D}_x$ and $\mathbf{D}_y^2 = \mathbf{D}_y \mathbf{D}_y$, and the positive smoothing parameters λ_x and λ_y. The implementation *LADrec2* is a straight extension of *LADrec*.

Other Regularizations

For the regularization term a least squares measure could also be used since the regularization only influences the smoothness of the reconstruction. The robustness to outliers should not be affected. In that case an appropriate solver has to be chosen because the problem is no longer a linear program but still a convex optimization problem.

Another way may be to let the regularization only work on the second derivative in x- or y-direction. The artificial peaks in the reconstructed surface should even in this easier approach be damped and the computational efficiency be increased compared to *LADrec2*. If the x-direction is chosen, the related minimization problem is:

$$
\text{minimize} \quad f_0(\boldsymbol{Z}) = \left\| \begin{pmatrix} \boldsymbol{W} \cdot (\mathbf{D}_x \otimes \boldsymbol{I}_m) \\ \boldsymbol{W} \cdot (\boldsymbol{I}_n \otimes \mathbf{D}_y) \\ \lambda_x \boldsymbol{W} \cdot (\mathbf{D}_x^2 \otimes \boldsymbol{I}_m) \end{pmatrix} \text{vec}(\boldsymbol{Z}) - \begin{pmatrix} \text{vec}(\boldsymbol{P}) \\ \text{vec}(\boldsymbol{Q}) \\ \boldsymbol{0} \end{pmatrix} \right\|_1. \tag{4.26}
$$

The implementation of this modified approach is *LADrec3*.

4.11.4 P-spline Reconstruction

In section 2.6 a special formulation for the differentiation of B-splines using tensor products was given. With this formulation a P-spline based least squares reconstruction is possible, enabling additional smoothing of the reconstructed surface or of its derivatives. By the way, the reconstructed surface may be interpolated at positions with gaps in the gradient data. The related least squares problem is

$$
\text{minimize} \quad f_0(\boldsymbol{\alpha}) = \left\| \begin{pmatrix} \boldsymbol{W} \boldsymbol{C}_x \boldsymbol{D}_{1,x} \\ \boldsymbol{W} \boldsymbol{C}_y \boldsymbol{D}_{1,y} \\ \lambda_x \boldsymbol{D}_{2,x} \\ \lambda_y \boldsymbol{D}_{2,y} \end{pmatrix} \text{vec}(\boldsymbol{\alpha}) - \begin{pmatrix} \text{vec}(\boldsymbol{P}) \\ \text{vec}(\boldsymbol{Q}) \\ \boldsymbol{0} \\ \boldsymbol{0} \end{pmatrix} \right\|_2^2. \tag{4.27}
$$

The optimal surface is in vector notation given by: $\mathrm{vec}(\boldsymbol{Z}^*) = \boldsymbol{C}\boldsymbol{\alpha}^*$. Another way of using P-splines for surface reconstruction is

$$
\text{minimize} \quad f_0(\boldsymbol{\alpha}) = \left\| \begin{pmatrix} \boldsymbol{W}\boldsymbol{C}_x\boldsymbol{D}_{1,x} \\ \boldsymbol{W}\boldsymbol{C}_y\boldsymbol{D}_{1,y} \\ \lambda_x\,\boldsymbol{D}_{2,x}\boldsymbol{D}_{1,x} \\ \lambda_y\,\boldsymbol{D}_{2,y}\boldsymbol{D}_{1,y} \end{pmatrix} \mathrm{vec}(\boldsymbol{\alpha}) - \begin{pmatrix} \mathrm{vec}(\boldsymbol{P}) \\ \mathrm{vec}(\boldsymbol{Q}) \\ \boldsymbol{0} \\ \boldsymbol{0} \end{pmatrix} \right\|_2^2 , \tag{4.28}
$$

meaning that the P-spline penalty works on the surface's derivatives. Both methods yield quite the same reconstructions and are available with *p_rec* and *p_rec* (deriv.).

The method has various parameters k_x, k_y, n_x, n_y, λ_x, and λ_y. In practice it is sufficient to use cubic P-splines and simply a high number of B-splines in each direction. So, only the smoothing parameters λ_x and λ_y have to be chosen. The method can also handle non-rectangular domains since weights with zero value pseudo-observations are introduced.

4.11.5 P1-spline Reconstruction

If outliers are present, a P1-spline based surface reconstruction may be the better choice. The related L^1-norm approximation problem is

$$
\text{minimize} \quad f_0(\boldsymbol{\alpha}) = \left\| \begin{pmatrix} \boldsymbol{W}\boldsymbol{C}_x\boldsymbol{D}_{1,x} \\ \boldsymbol{W}\boldsymbol{C}_y\boldsymbol{D}_{1,y} \\ \lambda_x\,\boldsymbol{D}_{2,x} \\ \lambda_y\,\boldsymbol{D}_{2,y} \end{pmatrix} \mathrm{vec}(\boldsymbol{\alpha}) - \begin{pmatrix} \mathrm{vec}(\boldsymbol{P}) \\ \mathrm{vec}(\boldsymbol{Q}) \\ \boldsymbol{0} \\ \boldsymbol{0} \end{pmatrix} \right\|_1 \tag{4.29}
$$

or with penalty on the spline's derivatives

$$
\text{minimize} \quad f_0(\boldsymbol{\alpha}) = \left\| \begin{pmatrix} \boldsymbol{W}\boldsymbol{C}_x\boldsymbol{D}_{1,x} \\ \boldsymbol{W}\boldsymbol{C}_y\boldsymbol{D}_{1,y} \\ \lambda_x\,\boldsymbol{D}_{2,x}\boldsymbol{D}_{1,x} \\ \lambda_y\,\boldsymbol{D}_{2,y}\boldsymbol{D}_{1,y} \end{pmatrix} \mathrm{vec}(\boldsymbol{\alpha}) - \begin{pmatrix} \mathrm{vec}(\boldsymbol{P}) \\ \mathrm{vec}(\boldsymbol{Q}) \\ \boldsymbol{0} \\ \boldsymbol{0} \end{pmatrix} \right\|_1 . \tag{4.30}
$$

Both methods can be solved as a linear program and yield quite the same reconstructions. They are available with *p1_rec* and *p1_rec* (deriv.).

4.11.6 Similar Surfaces

If the ground truth surface $\boldsymbol{Z_0}$ is known, e.g., in industrial material testing, Tikhonov regularization such as in section 4.6 may be applied. With this regularization the least squares based methods should be more stable to outliers since outliers alter the whole surface. For time series of water surface gradient fields the regularization may also work
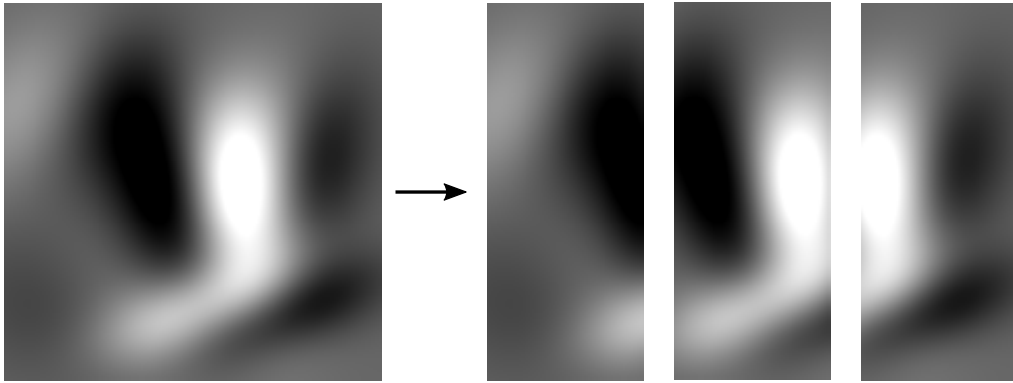
Figure 4.4 | Segmentation of a Gradient Field Component into Smaller Segments with Overlap.
The overlap is required to join the reconstructed surface segments in a smooth way because the integration constant is not known. It might be better to exclude the boundary of the reconstructed surface segments to avoid possible boundary effects. Appropriate segmentation allows to speed up slow methods.

if the water surface changes not much when it propagates between two frames. Instead of the ground truth Z_0, a shifted version of the reconstruction before would then be needed. The propagation velocity may be estimated with cross-correlation. Additionally, the reconstructed surfaces of a time series are no longer at different height levels.

Using the identity matrix for L_x and canceling the last term in Eq. 4.21, the formulation of the weighted least squares problem is straightforward. The regularization may also be used to speed up the least absolute deviations based methods. In addition, the artificial single peaks in the reconstruction with the method *LADrec* are damped. For the spline based methods a spline representation of the ground truth surface is needed.

4.12 Segmentation

Some of the to outliers robust methods using L^1-norm minimization can quickly get out of hand for large gradient fields. One idea to speed up these methods may be to use them locally in gradient field segments and put the results together.

Since there is no information about the integration constant, some overlap of the segments is needed to provide a smooth surface without discontinuities. It is assumed that in the overlap region the reconstructions differ basically in the integration constant. The overlap reduces also influences of boundary effects, e.g., due to outlier corruption at the border of a segment. Figure 4.4 shows a possible way for segmentation.

Segmentation may also be applied to methods not working on non-rectangular domains. However, the implementation may be for gaps somewhat tricky in contrast to the segmentation of large datasets. Methods handling non-rectangular domains have no segments to join. Joining segments are an additional error source and should be avoided if possible.

Reconstruction Error Analysis 5

In this chapter selected gradient-based surface reconstruction methods are compared in the cases of noise, outliers, and gaps in the gradient field. All implementations mentioned in Chapter 4 were tested. The uncorrupted gradient field of the non-analytical test surface *ramppeaks* was numerically calculated with the more accurate five-point formulas in contrast to the original source and most literature.

It turned out that, respecting Eq. 4.1, the use of simple forward-differences is the best choice for the methods described in section 4.11, besides performing on uncorrupted gradient fields. Thus, for these methods simple forward-differences were used in this chapter. For the spline based reconstruction methods the penalties were set on the surfaces most of the time and not on the derivatives. Linear programs were solved with the commercial solver Gurobi (free academic versions are available).

In the first sections of this chapter the reconstructed surfaces are 'eyeballed' only. In section 5.8 a detailed reconstruction error and computation time analysis is given for different surfaces and surface sizes. Additionally, the conceptual simple pre-processing of gradient data is investigated. Pre-processing may be an alternative to complex reconstruction methods in some special cases.

5.1 Gaussian Noise

Surface reconstruction techniques should be robust to noise since noise is omnipresent in measured data. Therefore, different Gaussian noise levels were added to the test surfaces' gradient fields. Figure 5.1 and Figure 5.2 show reconstructions of various methods in the case of Gaussian noise only. The joining of the segments in the reconstructions j) and l) is hardly visible.

Parameters of the L^1-norm based methods were tuned for the outlier case and are to some degree surface dependent. The parameters for the methods *LADrec2* and *LADrec3* were fixed for almost all surfaces in this chapter. The tuning of them is quite simple in the outlier case: increasing of the parameters until the single peaks vanish but too high values lead to inappropriate smoothing. In case of doubt increasing them a bit more is feasible since the methods are not very sensitive to the parameters in many cases.
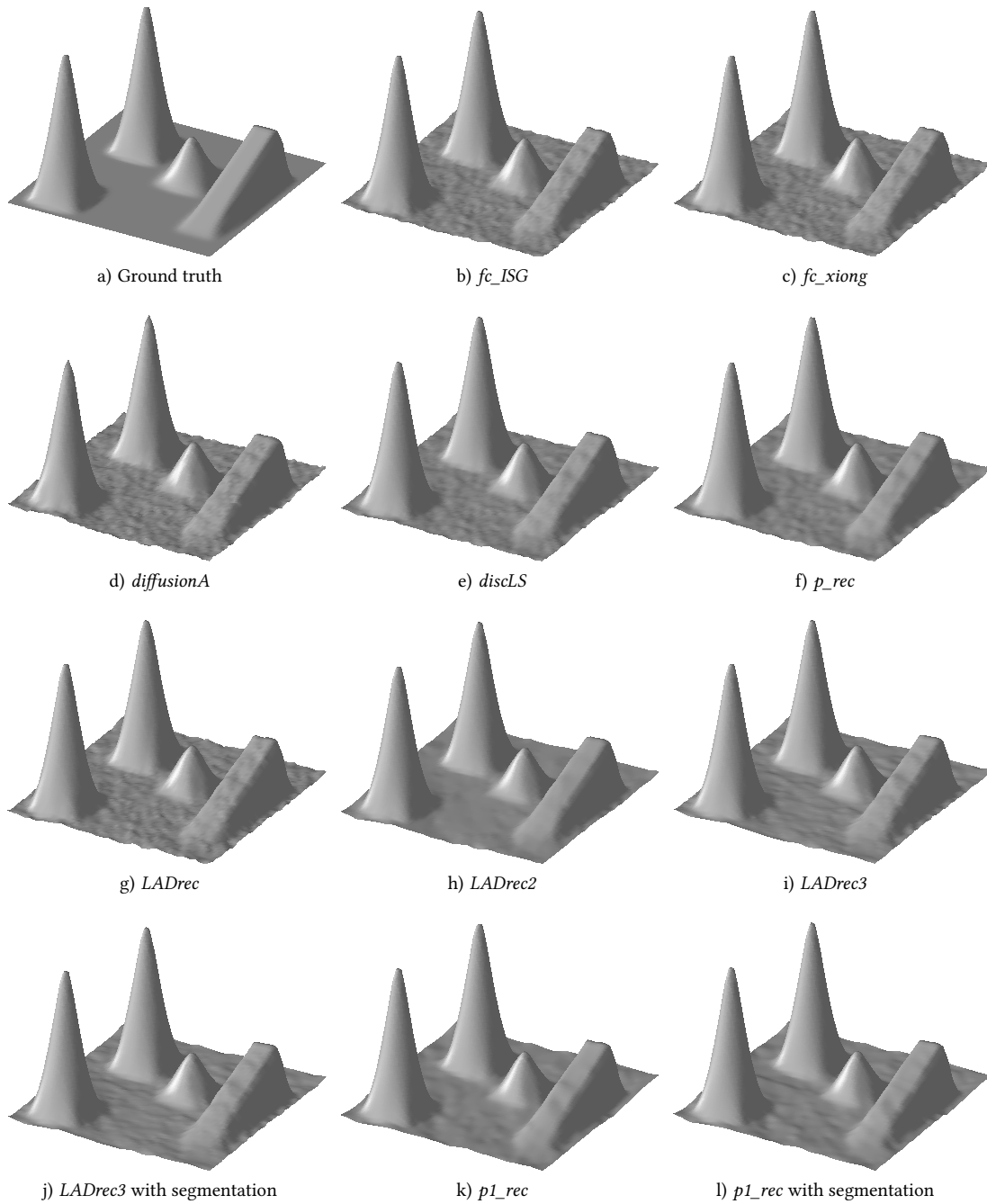
a) Ground truth

b) *fc_ISG*

c) *fc_xiong*

d) *diffusionA*

e) *discLS*

f) *p_rec*

g) *LADrec*

h) *LADrec2*

i) *LADrec3*

j) *LADrec3* with segmentation

k) *p1_rec*

l) *p1_rec* with segmentation

Figure 5.1 │ Reconstructions of the 64-by-64 Ramppeaks Surface in the Case of Gaussian Noise ($\sigma = 5\,\%\|g\|_\infty$). Parameters for *LADrec2*: $\lambda_x = \lambda_y = 0.6$. Parameters for *LADrec3* with and without segmentation: $\lambda_x = 0.8$. Parameters for *p_rec*: $k_x = k_y = 3$, $n_x = n_y = 64$, $\lambda_x = \lambda_y = 0.3$. Parameters for *p1_rec*: $k_x = k_y = 3$, $n_x = n_y = 64$, $\lambda_x = \lambda_y = 0.3$. Parameters for *p1_rec* with segmentation: $k_x = k_y = 3$, $n_x = 65$, $n_y = 55$, $\lambda_x = 0.3$, $\lambda_y = 0.35$. Segmentation: two 39-by-64 segments.

a) Ground truth

b) *fc_ISG*

c) *fc_xiong*

d) *diffusionA*

e) *discLS*

f) *p_rec*

g) *LADrec*

h) *LADrec2*

i) *LADrec3*

j) *LADrec3* with segmentation

k) *p1_rec*

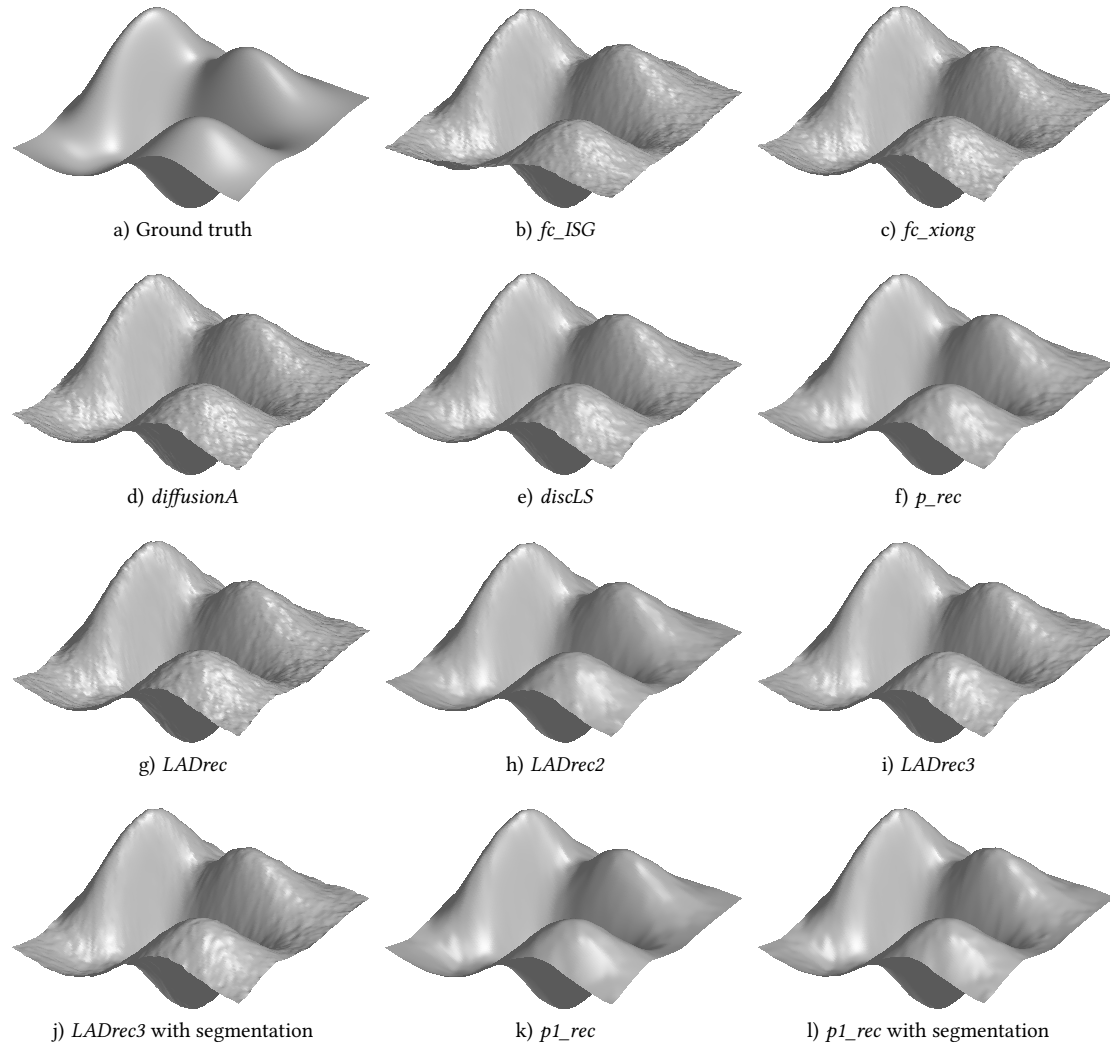l) *p1_rec* with segmentation

Figure 5.2 │ Reconstructions of the 128-by-128 g2sTestSurf Surface in the Case of Gaussian Noise ($\sigma = 10\,\%\|g\|_\infty$). Parameters for *LADrec2*: $\lambda_x = \lambda_y = 0.6$. Parameters for *LADrec3* with and without segmentation: $\lambda_x = 0.8$. Parameters for *p_rec*: $k_x = k_y = 3$, $n_x = n_y = 128$, $\lambda_x = \lambda_y = 0.5$. Parameters for *p1_rec*: $k_x = k_y = 3$, $n_x = n_y = 64$, $\lambda_x = \lambda_y = 0.4$. Parameters for *p1_rec* with segmentation: $k_x = k_y = 3$, $n_x = 65$, $n_y = 55$, $\lambda_x = 0.3$, $\lambda_y = 0.35$. Segmentation: two 71-by-128 segments. The reconstruction with *fc_ISG* shows boundary effects as mentioned in section 4.1.

In the case of Gaussian noise, only eyeballing of the reconstructions yields no information about the best method. Even the half pixel shift of the method *diffusionA* is not recognizable. Only the boundary effects of *fc_ISG* in Figure 5.2 shows the disadvantages of this method. Though, it can be seen that the methods are quite robust to noise.

5.2 Outliers

As mentioned before, in computer vision processes simplified assumptions do often not hold for illumination and surface reflection. Thus, the robustness to outliers is another major task in gradient-based surface reconstruction. For testing the robustness to outliers, randomly distributed positive and negative outliers were added to the uncorrupted gradient fields such as in Badri and Yahia (2016).

The outlier amount $N_{out} = p_{out} \cdot m \cdot n$, where m and n mark the surface/gradient size, and magnitude a_{out} were varied. In this thesis N_{out} outliers were added to each gradient field component, whereas it is in Badri and Yahia (2016) not clear if each component or the total amount was meant. Comparing the least squares based method suggests the former case. The L^1-minimization based methods in Badri and Yahia (2016) seem to be implemented erroneously.

Figure 5.3 shows reconstructions of various methods in the presence of outliers only. Obviously, and how expected, are only the L^1-norm based methods robust to outliers. Thus, in the high outlier corruption case *diffusionA* is not robust. The boundary effects at the borders in x-dimension in *LADrec3* appear since the x-derivative is used for regularization. For higher regularization parameters λ_x these effect may vanish or for smaller outlier magnitudes.

5.3 Gaussian Noise and Outliers

More realistic than the case of outliers only is the case of noise and outliers. Figure 5.4 to Figure 5.7 show reconstructions of various methods in the presence of outliers and noise. Again, only the L^1-norm based methods are robust enough.

Since in some gradient field measuring methods, e.g., in imaging slope gauge, the measurement errors are bounded, a more moderate outlier corruption was added in Figure 5.5 and Figure 5.7. However, once again only the L^1-norm based methods are robust enough, but the regularization in *LADrec3* works better with the same regularization parameter as before.

In Figure 5.5 *diffusionA* delivers a quite well reconstruction for a not L^1-norm based method. However, looking at the front peak and considering the half pixel shift disqualifies this method as a usable one. Furthermore is the robustness of *diffusionA* in the moderate outlier case dependent on the outlier positions.
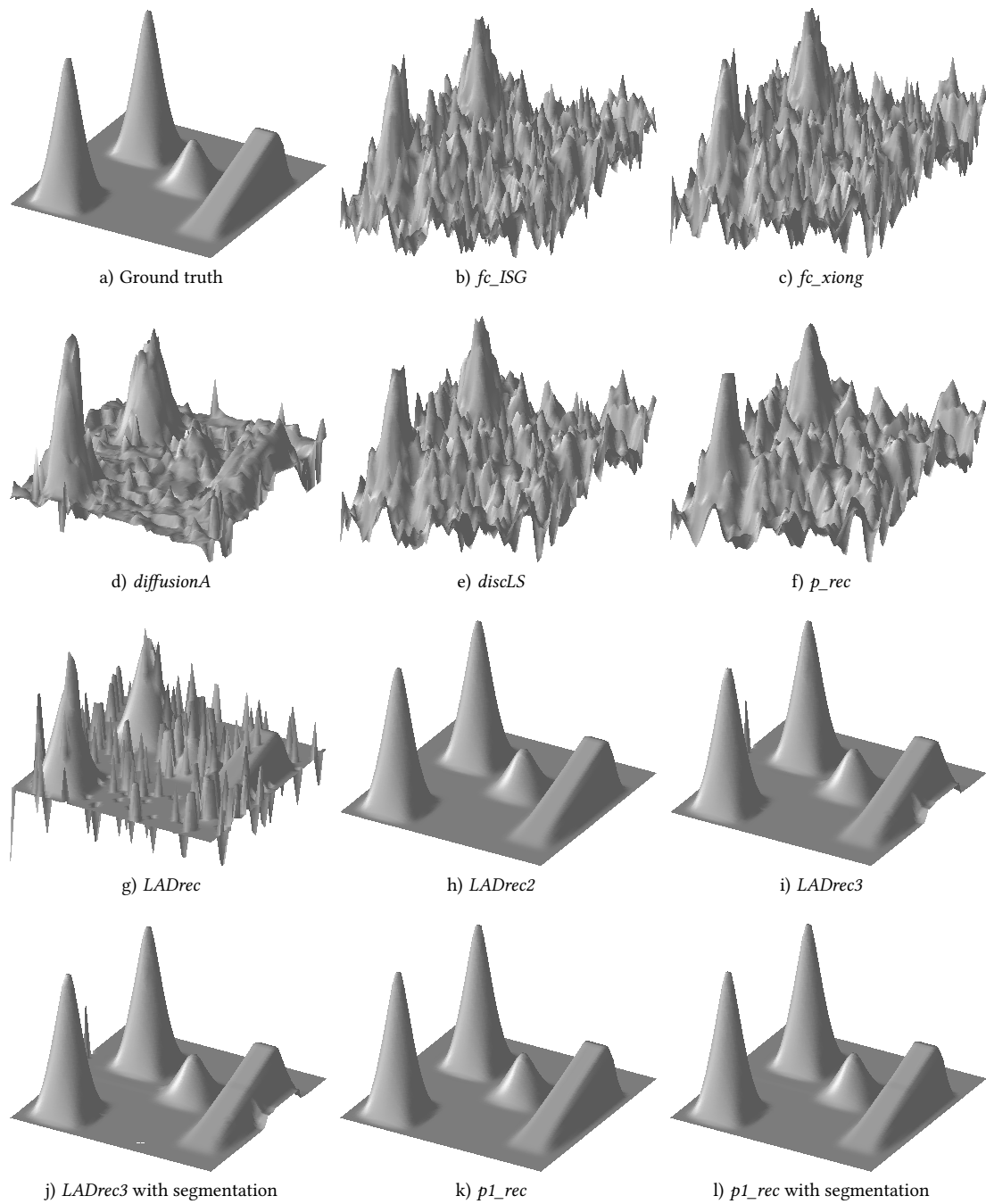
a) Ground truth   b) *fc_ISG*   c) *fc_xiong*

d) *diffusionA*   e) *discLS*   f) *p_rec*

g) *LADrec*   h) *LADrec2*   i) *LADrec3*

j) *LADrec3* with segmentation   k) *p1_rec*   l) *p1_rec* with segmentation

Figure 5.3 │ Reconstructions of the 64-by-64 Ramppeaks Surface in the Case of Outliers only ($p_{\mathbf{out}} = 10\,\%$, $a_{\mathbf{out}} = 5\,\|g\|_\infty$). Parameters of the methods are such as in Figure 5.1. The height ranges of the reconstructions b), c), e), f), and g) are reduced for a clear view. The outlier corruption is quite heavy for this rather bad sampled surface resulting in the single peaks in *LADrec* and the boundary effects in *LADrec3*. The least squares based methods are not robust to outliers.
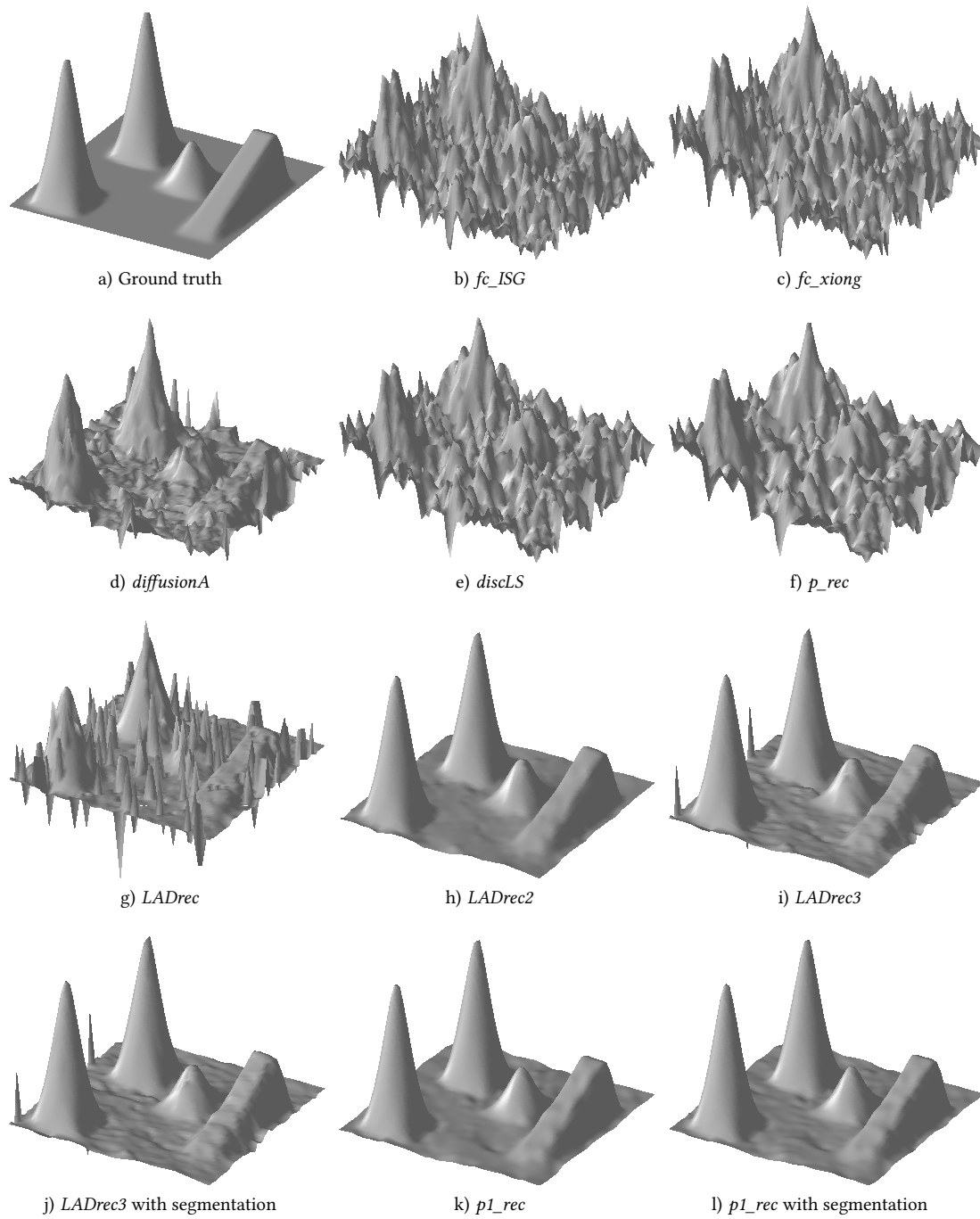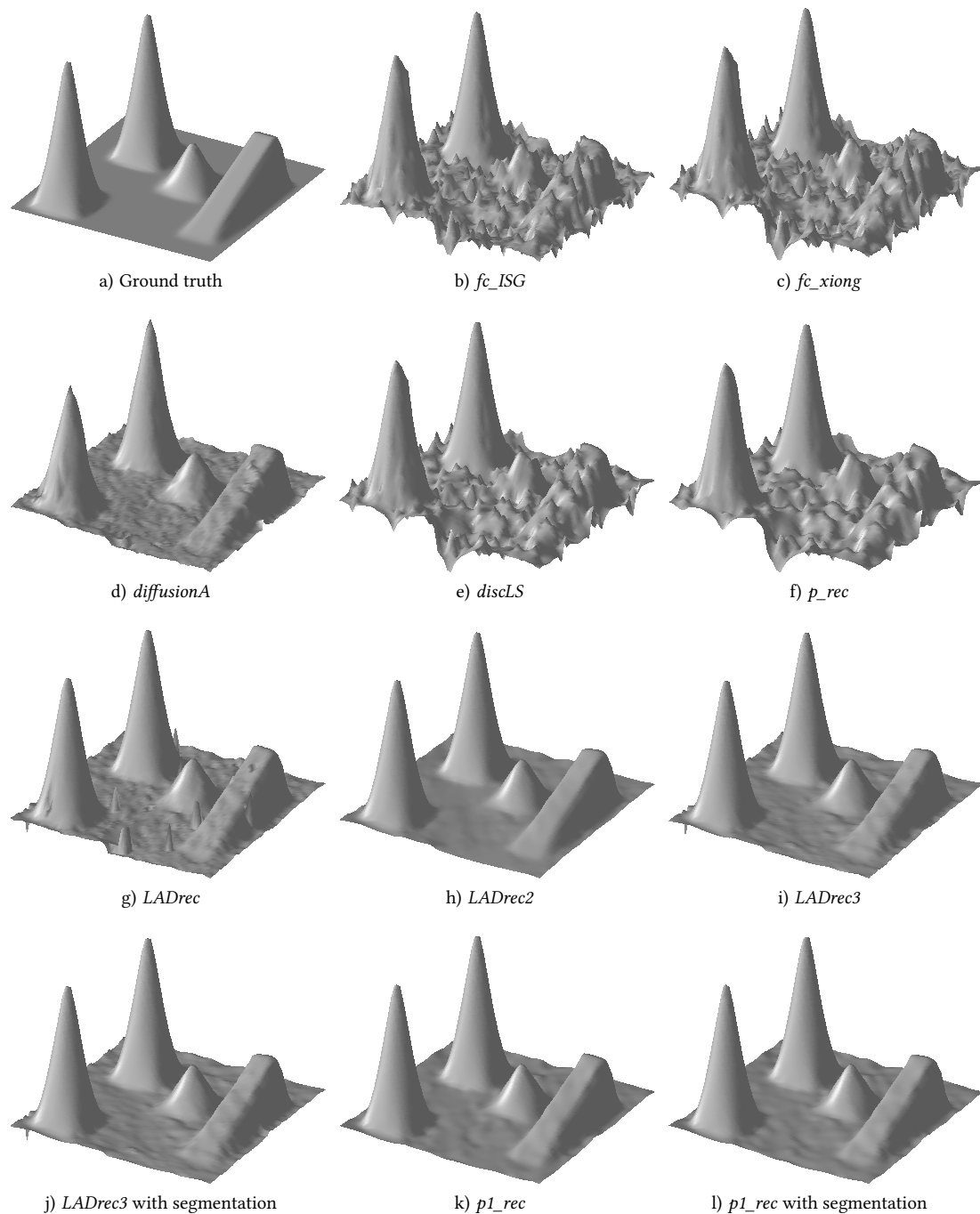
a) Ground truth   b) *fc_ISG*   c) *fc_xiong*

d) *diffusionA*   e) *discLS*   f) *p_rec*

g) *LADrec*   h) *LADrec2*   i) *LADrec3*

j) *LADrec3* with segmentation   k) *p1_rec*   l) *p1_rec* with segmentation

Figure 5.4 │ Reconstructions of the 64-by-64 Ramppeaks Surface in the Case of Outliers and Gaussian Noise ($\sigma = 5\,\%\|g\|_\infty$, $p_{\mathbf{out}} = 10\,\%$, $a_{\mathbf{out}} = 5\,\|g\|_\infty$). Parameters of the methods are such as in Figure 5.1. The height ranges of the reconstructions b), c), d), e), f), and g) are reduced for a clear view. The outlier corruption is quite heavy for this rather bad sampled surface resulting in the single peaks in *LADrec* and the boundary effects in *LADrec3*.

a) Ground truth   b) *fc_ISG*   c) *fc_xiong*

d) *diffusionA*   e) *discLS*   f) *p_rec*

g) *LADrec*   h) *LADrec2*   i) *LADrec3*

j) *LADrec3* with segmentation   k) *p1_rec*   l) *p1_rec* with segmentation
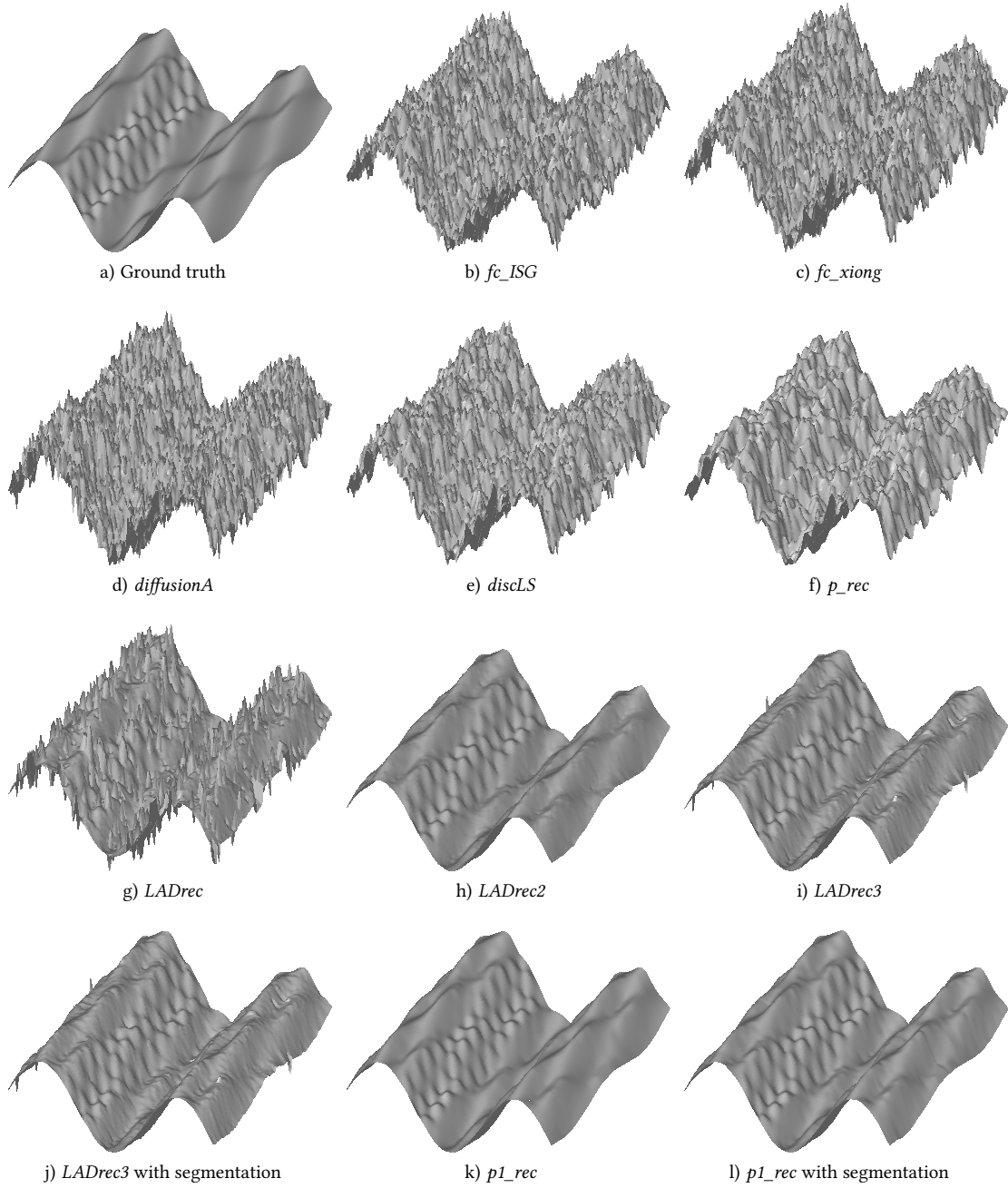
Figure 5.5 │ Reconstructions of the 64-by-64 Ramppeaks Surface in the Case of Outliers and Gaussian Noise ($\sigma = 5\,\%\|g\|_\infty$, $p_{\text{out}} = 3\,\%$, $a_{\text{out}} = 2.5\,\|g\|_\infty$). Parameters of the methods are such as in Figure 5.1. In contrast to Figure 5.4, the regularization in *LADrec3* works better with the same parameter since the outliers have smaller magnitude. Even for this moderate outlier corruption the least squares based methods are not robust enough.

a) Ground truth

b) *fc_ISG*

c) *fc_xiong*

d) *diffusionA*

e) *discLS*

f) *p_rec*

g) *LADrec*

h) *LADrec2*

i) *LADrec3*

j) *LADrec3* with segmentation
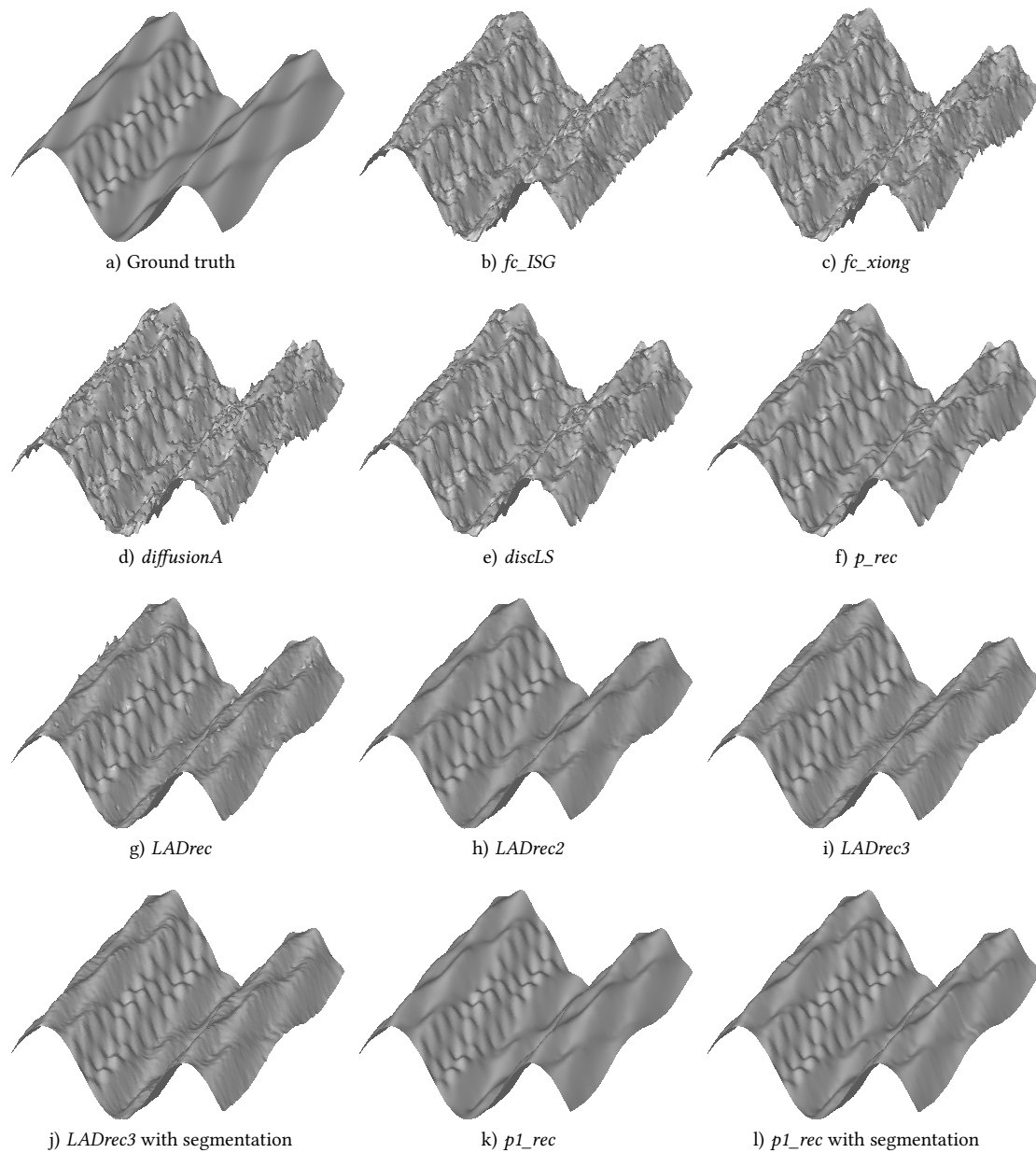
k) *p1_rec*

l) *p1_rec* with segmentation

Figure 5.6 │ Reconstructions of the 128-by-128 Cos2 Surface in the Case of Outliers and Gaussian Noise ($\sigma = 7\,\% \|g\|_\infty$, $p_{out} = 10\,\%$, $a_{out} = 5\,\|g\|_\infty$). Parameters of the methods and the segmentation are such as in Figure 5.2. The height ranges of the reconstructions b), c), d), e), and f) are reduced for a clear view.

a) Ground truth

b) *fc_ISG*

c) *fc_xiong*

d) *diffusionA*

e) *discLS*

f) *p_rec*

g) *LADrec*

h) *LADrec2*

i) *LADrec3*

j) *LADrec3* with segmentation

k) *p1_rec*

l) *p1_rec* with segmentation

Figure 5.7 | **Reconstructions of the 128-by-128 Cos2 Surface in the Case of Outliers and Gaussian Noise ($\sigma = 7\,\%\,\|g\|_\infty$, $p_{\text{out}} = 3\,\%$, $a_{\text{out}} = 2\,\|g\|_\infty$).** Parameters of the methods and the segmentation are such as in Figure 5.2. The least squares based methods at least reconstruct the structure of the surface roughly.

a) Ground truth.   b) Median filtering and *discLS*.   c) *p1_rec*
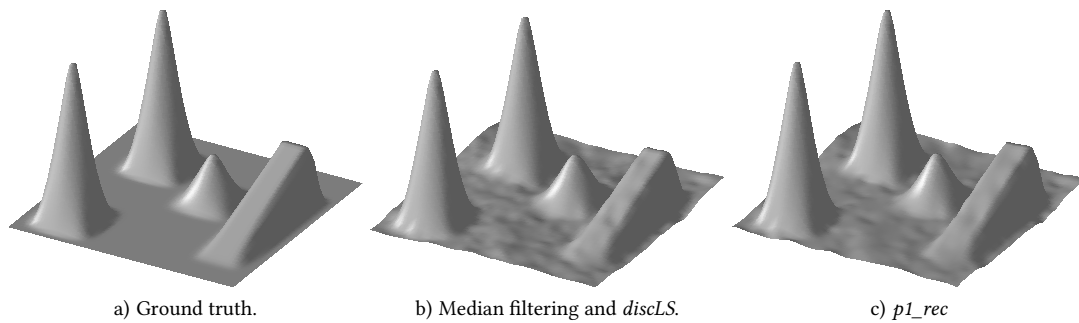
Figure 5.8 │ 64-by-64 Ramppeaks Surface Reconstructed with Median Filter Pre-processing in the Case of Outliers and Gaussian Noise ($\sigma = 5\,\%\|g\|_\infty$, $p_\mathrm{out} = 10\,\%$, $a_\mathrm{out} = 5\,\|g\|_\infty$). Parameters of *p1_rec* are such as in Figure 5.1. With median filtering the reconstruction is much faster but not as accurate as the reconstruction with *p1_rec* since the peaks are smoothed slightly.

5.4 Imperfect Gradient Fields

Another problem may be the reconstruction from incomplete gradient fields. Incomplete grids may occur for very steep surfaces, e.g., in imaging slope gauge measurements, or if the area to investigate of the surface is separated from its background. For testing the reconstruction methods, the highest absolute slope values in the uncorrupted gradient data were ignored. Only methods which can handle non-rectangular domains can be applied without pre-processing how Figure 5.9 shows.

All spline based methods may also interpolate the surface such as the reconstructions k) and l) show. Using *LADrec*, *LADrec2*, and *LADrec3*, the gaps are spreading one pixel in the related dimension because of the respecting of Eq. 4.1.

5.5 Data Pre-processing

Instead of using to outlier corruption adapted methods, pre-processing of the corrupted gradient field and using a fast method may be an alternative since to outliers robust methods are generally no fast methods. Besides the gain in computational efficiency in the outlier case, an open question is which reconstruction quality may be achieved.

5.5.1 Median Filtering

Median filtering is a common technique for filtering outliers. Figure 5.8 shows a reconstruction of the non-robust method *discLS* performed on the median filtered gradient. Comparing with Figure 5.4, the improvement due to the filtering is obvious. Major advantage is the possible use of one of the fast, not to outliers robust methods. Disadvantages are the smoothing of steep structures and the related reduction of the reconstruction quality. For better sampled surfaces this reduction may be insignificant.
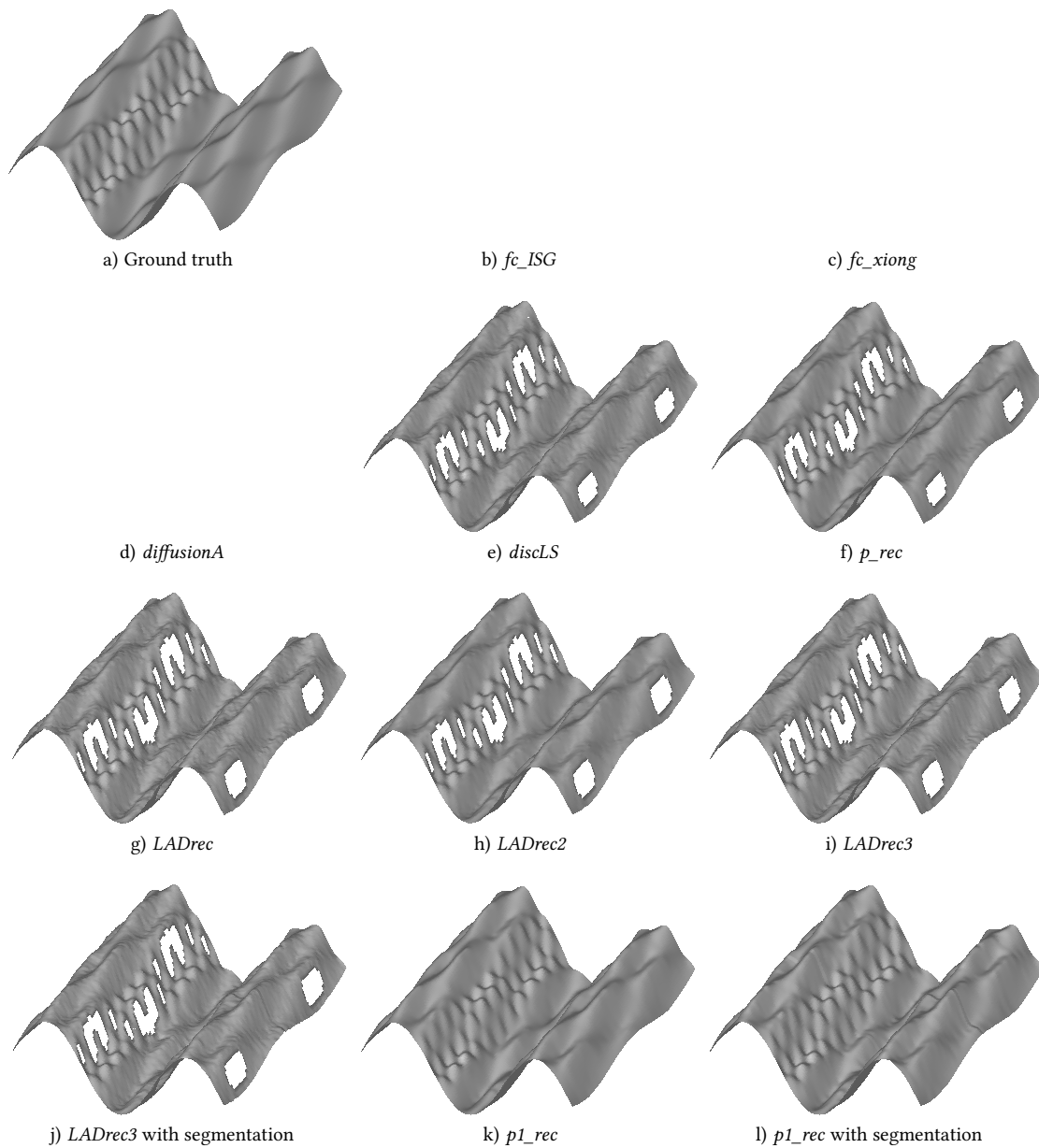
a) Ground truth   b) *fc_ISG*   c) *fc_xiong*

d) *diffusionA*   e) *discLS*   f) *p_rec*

g) *LADrec*   h) *LADrec2*   i) *LADrec3*

j) *LADrec3* with segmentation   k) *p1_rec*   l) *p1_rec* with segmentation

Figure 5.9 │ Reconstructions of the 128-by-128 Cos2 Surface in the Case of Gaussian Noise and Gaps ($\sigma = 7\,\%\|g\|_\infty$). Parameters of the methods and the segmentation are such as in Figure 5.2. The methods b), c), and d) are not able to reconstruct surfaces from imperfect gradient fields. All spline methods may interpolate the gaps.

a) Ground truth   b) *discLS*   c) P1-spline smoothing and *discLS*
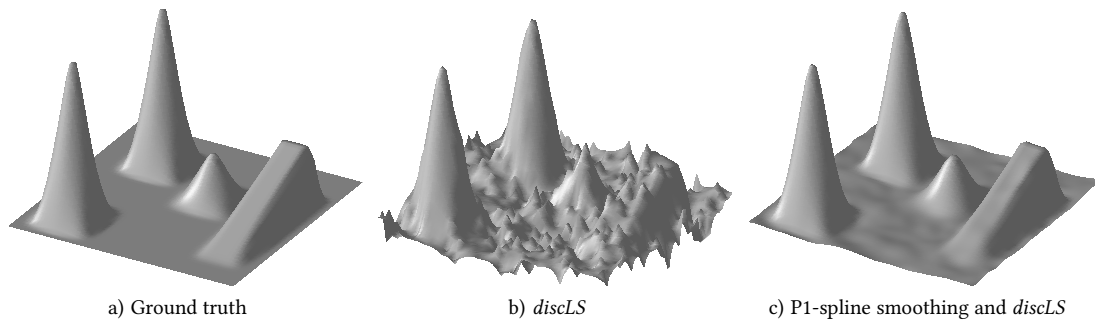
Figure 5.10 │ 64-by-64 Ramppeaks Surface Reconstructed without and with P1-spline Pre-processing in the Case of Outliers and Gaussian Noise ($\sigma = 5\,\% \|g\|_\infty$, $p_{\text{out}} = 3\,\%$, $a_{\text{out}} = 2.5\,\|g\|_\infty$). The enhancement of the reconstruction quality with P1-spline smoothing is obvious in the outlier case. Thus, P1-spline pre-processing may be an alternative to the L^1-norm based reconstruction methods with the difficulties shifted to the pre-processing.

5.5.2 Binomial Filtering

Binomial filtering could in tests not improve the reconstruction quality significantly since many methods are specialized to noisy gradient fields anyway. Outliers would only be damped slightly but propagate.

5.5.3 Spline Smoothing

Generalized cross-validation provides a tool for finding the right amount of smoothing with P-splines if the numbers n_x and n_y of B-splines are not too high. In the case of noise a small enhancement in reconstruction quality is possible but only feasible if the smoothing parameters have to be tuned one time only, e.g., in industrial material testing. The smoother the surface the better is the reconstruction after P-spline smoothing.

Figure 5.10 shows how pre-processing with P1-splines may improve the reconstruction quality for non-robust methods. The results of P1-spline pre-processing and P1-spline based reconstruction methods are quite similar. For the rest of this thesis only P1-spline based reconstruction methods are considered but P1-spline smoothing remains an interesting alternative. Gradient fields may be interpolated with spline pre-processing.

5.5.4 Gradient Field and Surface Interpolation

Instead of using a reconstruction method which can handle non-rectangular domains, imperfect gradient fields may be interpolated before. Then a method performs on the interpolated gradient field. To obtain an accurate and physically sound reconstruction a proper interpolation is needed. One possibility for gradient field interpolation may be spline interpolation. Another may be image restoration with a Laplacian diffusion
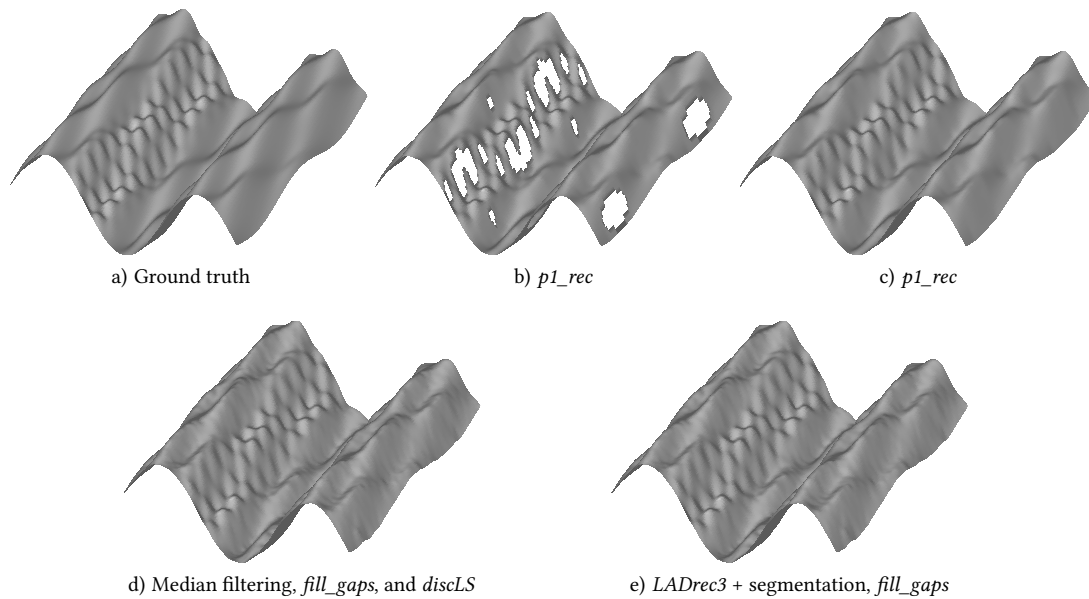
a) Ground truth   b) *p1_rec*   c) *p1_rec*

d) Median filtering, *fill_gaps*, and *discLS*   e) *LADrec3* + segmentation, *fill_gaps*

Figure 5.11 │ Comparison of Interpolation Techniques for Surface Reconstruction. The surfaces are 128-by-128 *cos2* surfaces reconstructed with various methods in the case of outliers and Gaussian noise ($\sigma = 7\,\%\|g\|_\infty$, $p_{\text{out}} = 3\,\%$, $a_{\text{out}} = 2\,\|g\|_\infty$). Parameters of the methods and the segmentation are such as in Figure 5.2. b) shows how large the gaps have been. The small scale structures are reconstructed quite well. Outliers and noise were added to the gradient after cutting off the largest slopes.

equation ansatz. For the latter *fill_gaps*, a from D. Kiefhaber slightly modified Laplace operator taken from the software for digital image processing Heurisko[1], was used.

fill_gaps may also be applied to surfaces reconstructed from incomplete gradient fields. In this case a method which can handle gaps in the data is needed. To get an interpolated reconstructed surface also one of the spline based reconstruction methods may be used. There may be advantages of surface interpolation in contrast to gradient field interpolation if the surface is smoother than its gradient.

Figure 5.11 shows a comparison of the different interpolation techniques. The differences are hardly recognizable with the human eye. Therefore, in section 5.8 is given a more detailed error analysis. The interpolation quality depends on the gap size and on the surface shape. Thus, in case of doubt it might be better to do without interpolation.

5.6 Depth Discontinuities

So far only smooth surfaces were considered. If the surface to be reconstructed contains depth discontinuities, all of the tested solvers fail how Figure 5.12 shows. L^1-norm based methods reconstruct the steep features of the surface but suffer from staircase

---

[1]http://www.aeon.de/heurisko_produkte.html

a) Ground truth   b) $\boldsymbol{Z}_x$ c) $\boldsymbol{Z}_y$

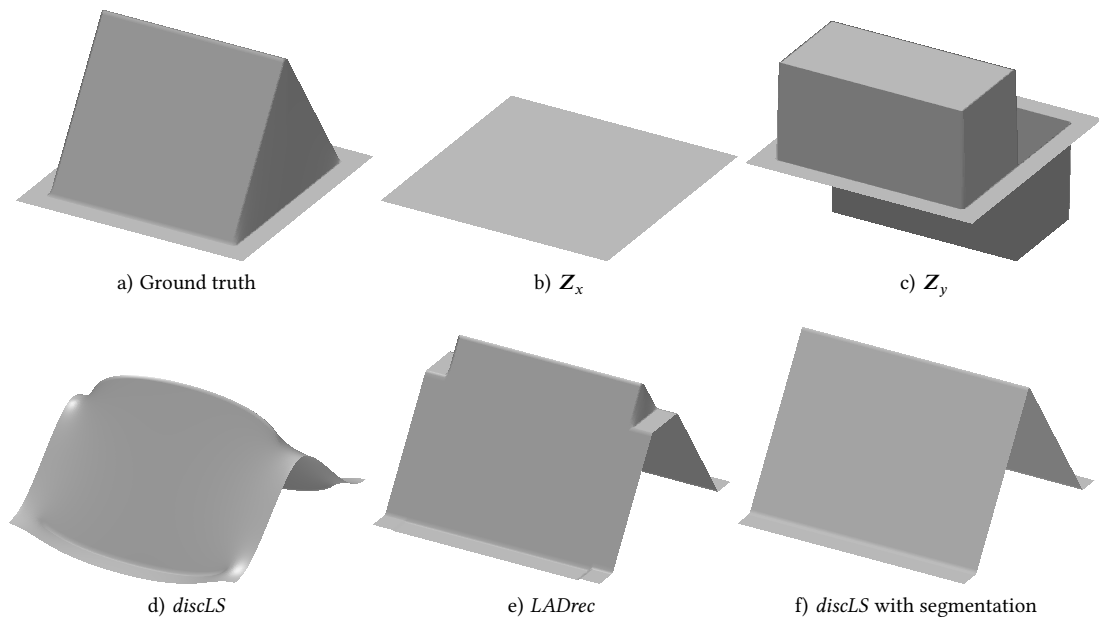d) *discLS*   e) *LADrec*   f) *discLS* with segmentation

Figure 5.12 │ Surface Reconstruction in the Presence of Depth Discontinuities. The 256-by-256 *tent* test surface contains depth continuities. Without segmentation of the gradient field into segments without depth discontinuities, the surface cannot be reconstructed accurately.

artifacts. With Tikhonov regularization as described in subsection 4.11.6 this artifacts can be avoided. Least squares based methods distort the surface since the integrability condition, Eq. 4.2, is not fulfilled. Then, the in section 4.1 mentioned smoothing appears.

For non-differentiable elements new adapted functionals are needed. The total variation functional proposed by Quéau and Durou (2015) shows smaller staircase artifacts (Quéau et al., 2017). Another way may be the segmentation into segments without depth discontinuities. Similar difficulties arise in the transition from foreground to background of objects (Bähr et al., 2017).

5.7 Computation Time Analysis

For a computation time analysis datasets with 20 differently but with same noise and outlier level corrupted gradient fields were generated. Mean computation time and standard deviation were estimated for different surface sizes. The calculations were carried out on a Windows 7 system with Intel Core i5-6500 CPU, 16 GB RAM and MATLAB R2016a. The results are presented in Table 5.1.

All of the least squares based methods provide a solution in reasonable time scales for all tested surface sizes. This includes the size of the for this thesis relevant ISG data. The computation time of *p_rec* may be reduced using less splines without affecting the reconstruction quality.

Table 5.1 | Computation Times for Various Surface Sizes. Datasets with 20 differently but with same corruption level corrupted gradient fields were generated to get mean computation time and standard deviation. The 64-by-64 surface is the *ramppeaks* test surface. The other surfaces are *cos2* surfaces. For the chosen segmentation (seg.), method parameters, and gradient field corruption see Appendix B. Standard deviations smaller than 5 ms are not stated below.

Method	Mean Computation Time [s]				
	64-by-64	128-by-128	256-by-256	512-by-512	760-by-930
fc_xiong	$9 \cdot 10^{-4}$	$3 \cdot 10^{-3}$	0.02	0.09	0.25
discLS	$8 \cdot 10^{-3}$	0.04	0.17 ± 0.01	0.84 ± 0.01	2.27 ± 0.06
p_rec	0.093	0.48 ± 0.01	0.96 ± 0.04	4.39 ± 0.04	8.40 ± 0.08
LADrec	0.17 ± 0.02	0.99 ± 0.03	6.6 ± 0.2	53 ± 2	$323 \pm 23^{\dagger}$
LADrec2	2.62 ± 0.01	4.2 ± 0.5	$40 \pm 7^{*}$	$-^{\ddagger}$	$-^{\ddagger}$
LADrec2 (seg.)	1.50 ± 0.02	3.56 ± 0.06	35 ± 13	$539 \pm 359^{\dagger}$	261 ± 11
LADrec3	0.31 ± 0.02	1.80 ± 0.07	11.0 ± 0.6	$154 \pm 30^{*}$	$-^{\ddagger}$
LADrec3 (seg.)	0.34 ± 0.02	1.71 ± 0.03	9.7 ± 0.3	56 ± 3	129 ± 3
p1_rec	3.58 ± 0.03	$21 \pm 1^{*}$	42.4 ± 0.2	$-^{\ddagger}$	$-^{\ddagger}$
p1_rec (seg.)	4.48 ± 0.07	16 ± 1	35.0 ± 0.4	$182 \pm 7^{*}$	223 ± 28

[*] One field was excluded from the analysis since the solver didn't find a solution in a reasonable time.
[†] Estimated from 4 fields only.
[‡] No computation time estimated.

The computation times of the L^1-norm based methods depend not only on the surface size but on the methods' parameters and on the gradient field corruption also. Further parameter tuning may reduce the computation time significantly since the method *LADrec2* was in tests even for a 1024-by-1024 surface in average faster than for the 512-by-512 surface with similar segmentation but different smoothing parameters.

Since median filtering is even for large gradient fields very fast, it was not considered in the computation time analysis. For a single 1024-by-1024 image median filtering needed about 0.1 s on the used system. Using Tikhonov regularization reduces the computation times significantly. For a 1024-by-1024 surface the computation time of *LADrec* could be reduced from approximately 750 s to approximately 115 s.

5.8 Reconstruction Errors

As in the section before, datasets were generated for a reconstruction error analysis. Mean reconstruction error and standard deviation were estimated for different corruption levels and surfaces. For the parameters used see Appendix B. Infrequently the parameters of the P1-spline based methods were modified slightly. The small modifications reduced the computation time in some cases without influencing the reconstruction error. Due to the artificial peaks, *LADrec* may only be used to check for outliers in a gradient field.
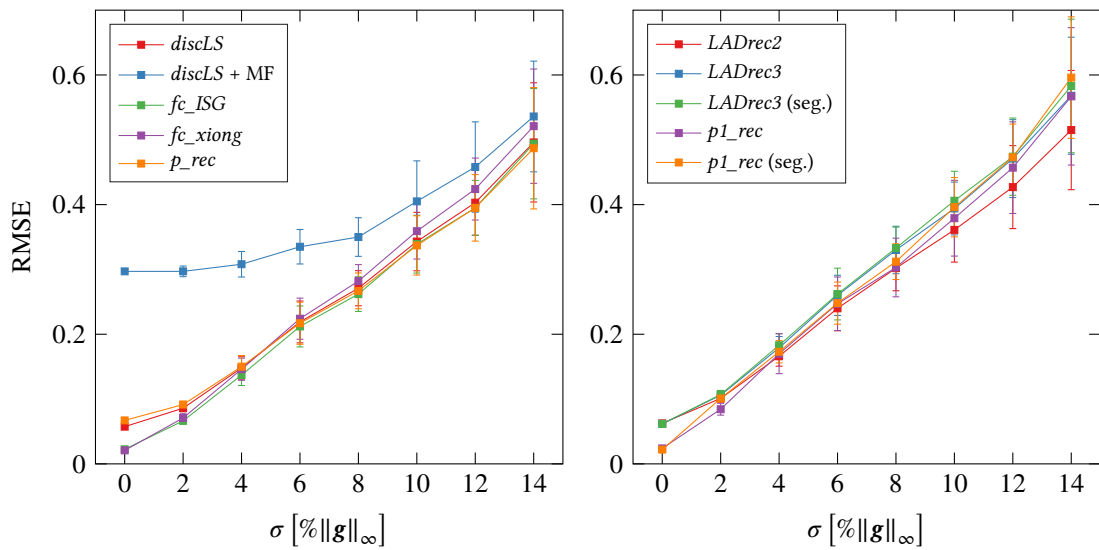
Figure 5.13 | Reconstruction Errors of the 64-by-64 Ramppeaks Surface for Different Gaussian Noise Levels. The reconstruction errors of the fast and without median filter (MF) pre-processing not to outliers robust methods are plotted in the left. The L^1-norm based methods are plotted in the right with segmentation (seg.) and without. Median filtering results in less accurate reconstructions since the *ramppeaks* surface is sampled badly and the filtering smooths the peaks and the ramp.

Figure 5.13 shows the reconstruction errors of various methods for different noise levels without outliers for the *ramppeaks* test surface. Besides the median filter (MF) method are the fast methods in the left plot at least as accurate as the L^1-norm based methods. The median filter reconstruction is less accurate due to some smoothing of the peaks and the ramp of the steep *ramppeaks* surface. This degradation reduces for the smoother *cos2* surface how the reconstruction errors in Figure 5.14 show. Gradient field segmentation (seg.) works for both surfaces quite well in the case of Gaussian noise.

The non-applicability of *fc_ISG* for non-periodic surface boundaries results in the large reconstruction errors in Figure 5.14. Thus, the error of *fc_ISG* may be used as a border for a successful reconstruction. The use of the in literature often used method *fc_agrawal* would result in even larger errors. Anyway, published error analyses should be handled with care. Sometimes, new methods are no improvement to a proper implementation of the method of Frankot and Chellappa (1988).

For no and low level gaussian noise *p_rec* and *discLS* seem less accurate than the other methods. This is the result of some built-in smoothing. The smoothing yields better reconstructions for high level noise. An advantage of all spline based methods is the adaptability to the noise level. Tuning the parameters of *p_rec* for each noise level individually resulted in lower reconstruction errors compared to the shown *p_rec* errors and to the other non-spline methods.

Finally, in the case of Gaussian noise only there is no need for the L^1-norm based methods. However, there is also no big disadvantage but computation time.
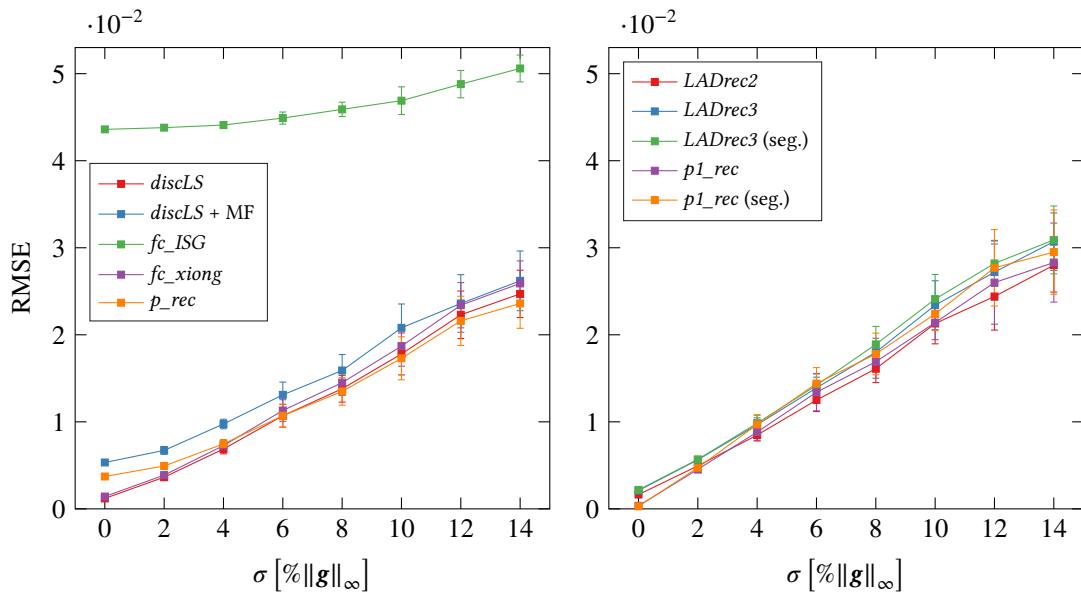
Figure 5.14 | Reconstruction Errors of the 128-by-128 Cos2 Surface for Different Gaussian Noise Levels. Median filtering results in smaller deviations than in Figure 5.13. In contrast to the *ramppeaks* surface, the non-periodic boundaries cause the large errors of the method *fc_ISG*. Thus, the error of *fc_ISG* can be used as a border for a successful reconstruction.

Figure 5.15 to Figure 5.18 show that even for small outlier magnitudes and low outlier amount the not robust methods are not really applicable. Segmentation results in to some degree larger reconstruction errors. If median filtering is an alternative to the L^1-norm based methods, depends on the sampling of the surface. For the used *cos2* surface median filtering is almost as accurate as *p1_rec* but much faster.

As already mentioned, sometimes boundary effects occur with the chosen regularization for the method *LADrec3* resulting in larger errors in contrast to *LADrec2*. These effects appear more frequently with higher outlier amount. The other robust methods were quite stable in relation to outlier amount and to outlier magnitude. Using the error of *fc_ISG* in the uncorrupted case as border, the robust methods yielded all a successful reconstruction even in the high outlier amount and magnitude case.

5.8.1 Interpolation

Before testing and comparing interpolation methods, the question was how to build in the gaps in the data. Using an imaging slope gauge the maximum measurable absolute slope depends on the geometry of the setup (Kiefhaber, 2014; Kiefhaber et al., 2014). Thus, in this thesis the largest slope values were cut off for testing interpolation. In the case of noise only, this was quite easy. There was only a small difference in the gaps if they were introduced before or after adding the noise to the test gradient field.
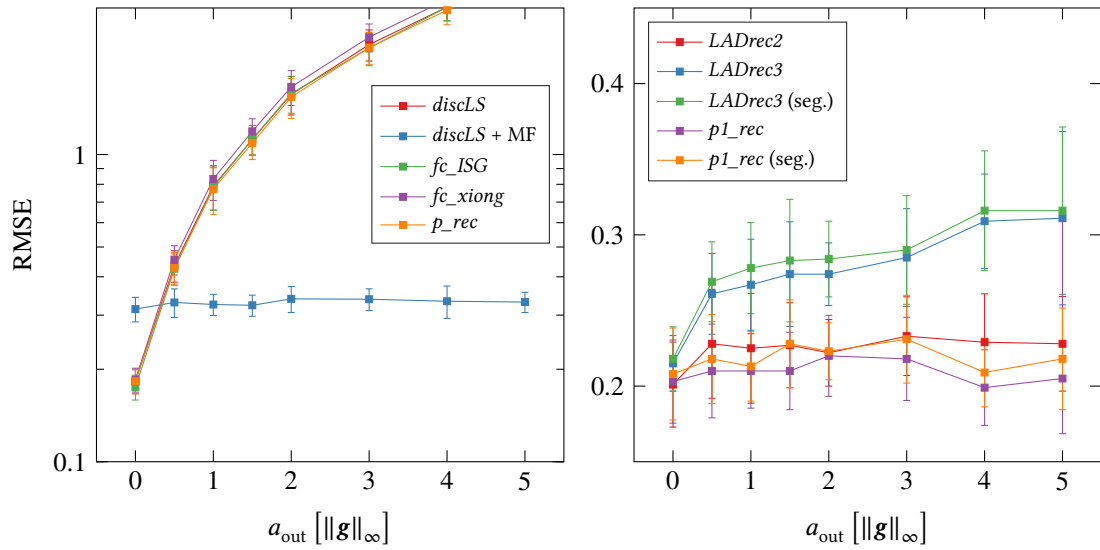
Figure 5.15 │ Reconstruction Errors of the 64-by-64 Ramppeaks Surface for Different Outlier Magnitudes ($\sigma = 5\,\%\|\boldsymbol{g}\|_\infty$, $p_{\text{out}} = 5\,\%$). Even for small magnitudes the non-robust methods are not really applicable. The chosen regularization for the method *LADrec3* is obviously not strong enough. Segmentation results in somewhat larger reconstruction errors.
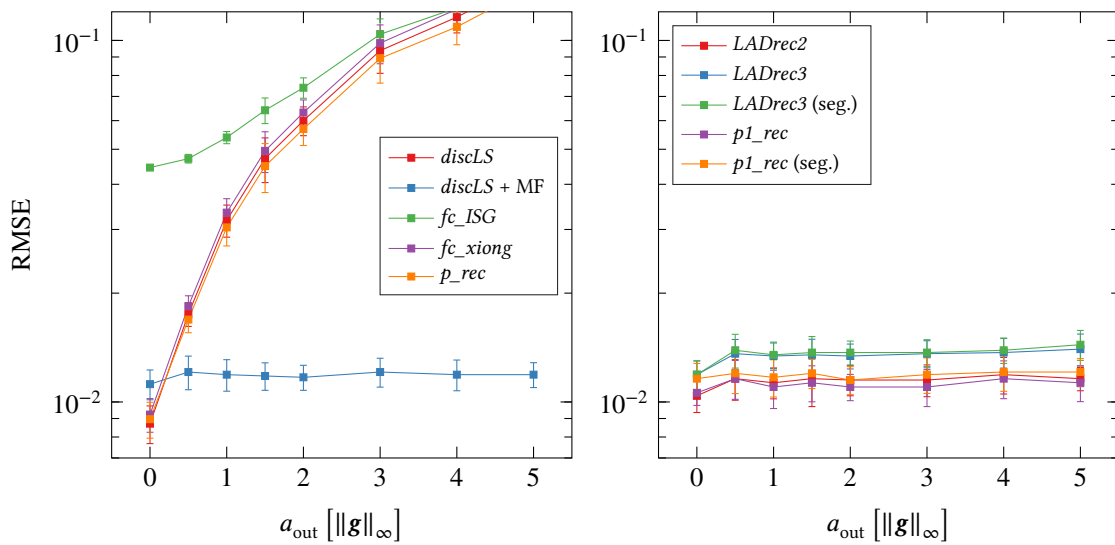

Figure 5.16 │ Reconstruction Errors of the 128-by-128 Cos2 Surface for Different Outlier Magnitudes ($\sigma = 5\,\%\|\boldsymbol{g}\|_\infty$, $p_{\text{out}} = 3\,\%$). The median filter method is not as accurate as *p1_rec* but comes quite close and is much faster. *LADrec3* is more accurate than in Figure 5.15. This is due to the dependency of the boundary effects on outlier positions and amount respectively.
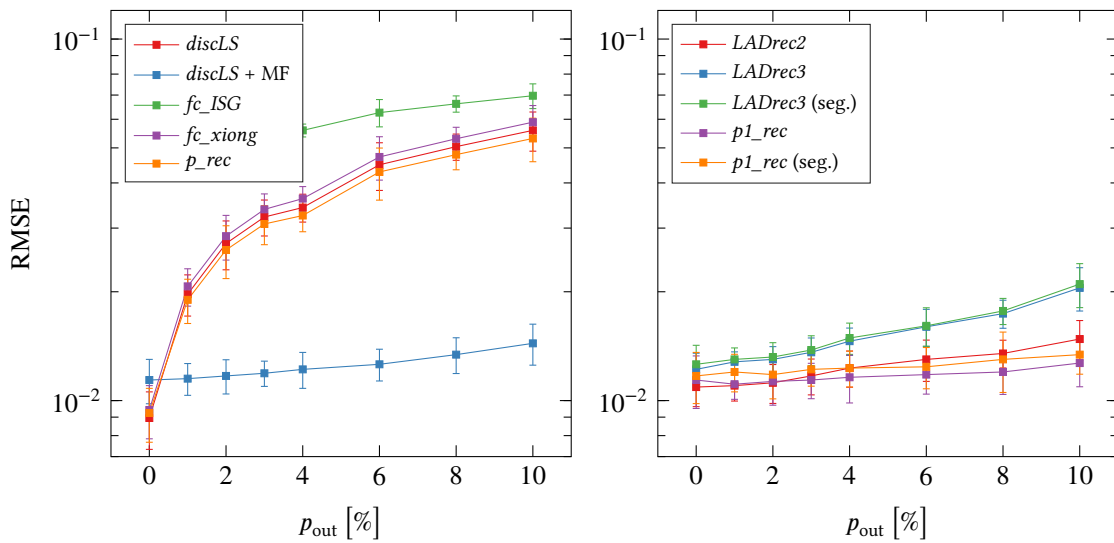
Figure 5.17 │ Reconstruction Errors of the 128-by-128 Cos2 Surface for Different Amounts of Outliers ($\sigma = 5\,\%\|g\|_\infty$, $a_{\text{out}} = 1\,\|g\|_\infty$). The robust methods are quite stable in relation to the outlier amount in this rather small outlier magnitude case. The accuracy of *LADrec3* drops with the outlier amount since the already mentioned boundary effects occur more frequently and the regularization works not well at the boundaries.
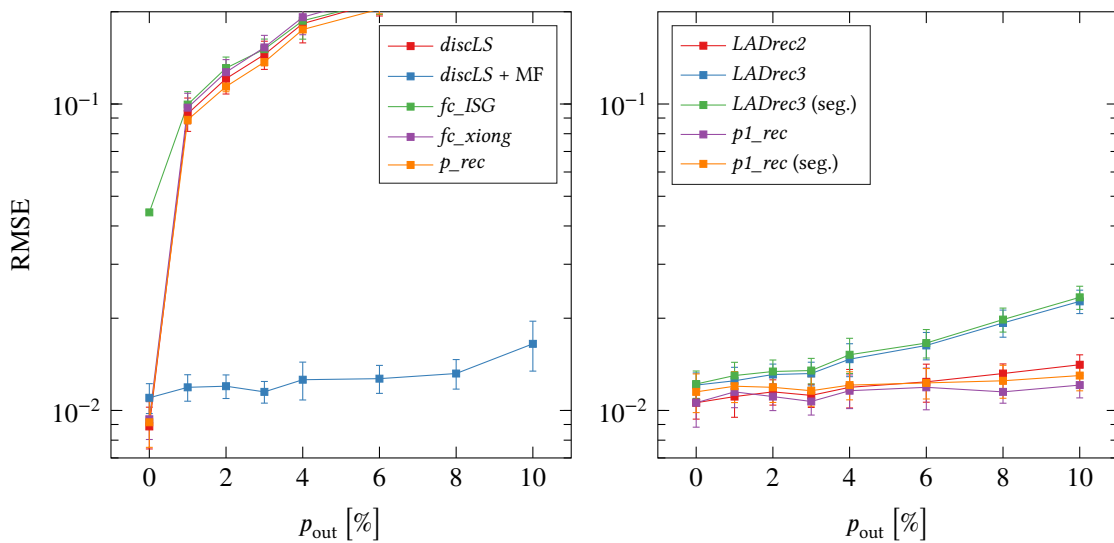

Figure 5.18 │ Reconstruction Errors of the 128-by-128 Cos2 Surface for Different Amounts of Outliers ($\sigma = 5\,\%\|g\|_\infty$, $a_{\text{out}} = 5\,\|g\|_\infty$). The robust methods are even quite stable to the outlier amount in this high outlier magnitude case. Using the error of *fc_ISG* for $p_{\text{out}} = 0$ as border, the robust methods yield all a successful reconstruction even in the high outlier amount case.
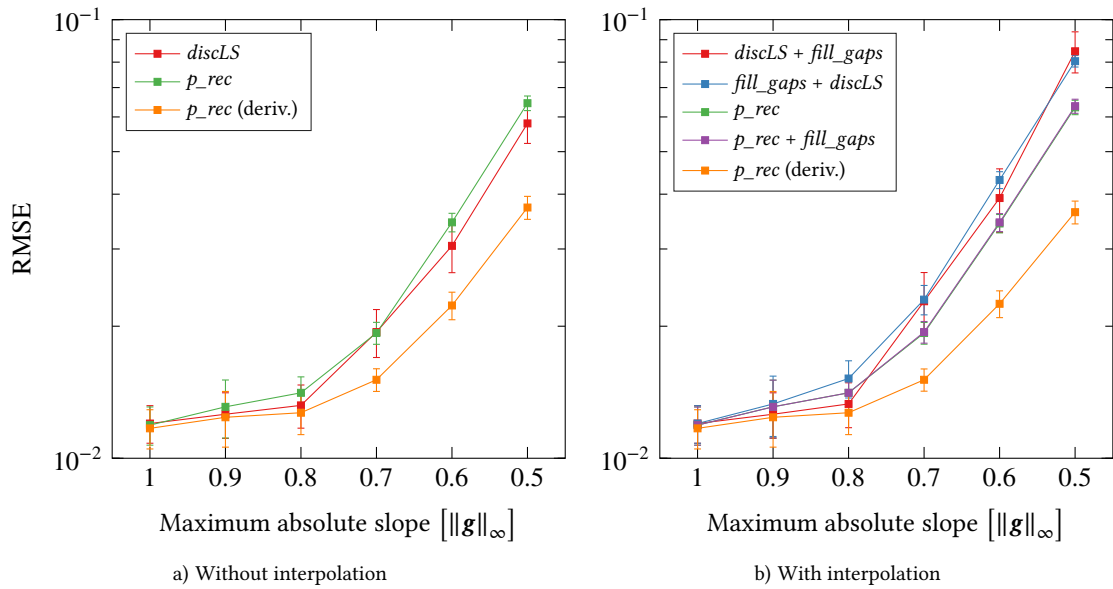
a) Without interpolation   b) With interpolation

Figure 5.19 | Reconstruction Errors of the 128-by-128 Cos2 Surface in the Case of Gaussian Noise and Interpolation ($\sigma = 7\,\%\|g\|_\infty$) Without interpolation, *p_rec* is in average not as accurate as *discLS*, but with interpolation superior to *discLS*. *p_rec* (deriv.), which sets the penalties on the derivatives, is for interpolation the best tested method. The noise was added before cutting off the largest slope values.

In the case of outliers there was a huge difference between cutting off the largest slopes before or after adding the outliers. In the former method there were outliers in the gradient field with much larger value than the maximum measurable. This was not realistic but could be used for a challenging interpolation test. In the latter method a problem was to cut not only outliers away resulting in single one pixel size gaps. Another problem might have been to cut off all outliers. Thus, only moderate outlier magnitudes could be used.

In Figure 5.19 different interpolation techniques are compared. The noise was added before cutting off the largest slope values. In the left plot the reconstruction errors for the reconstruction without interpolation are shown. The errors without interpolation are not directly comparable with the errors with interpolation since *m* and *n* in Eq. 2.11 are different. However, the left plot shows that *p_rec* is less accurate than *discLS* without interpolation. In contrast, *p_rec* is more accurate than *discLS* for the larger gaps in the interpolation case. This may be due to boundary effects of *discLS* near gaps. Applying *fill_gaps* to a non-interpolated *p_rec* reconstruction yields no difference to an interpolated *p_rec* reconstruction. Using the spline method *p_rec* (deriv.), which sets the penalties on the derivatives, yields better reconstructions. The larger the gaps the larger is the advantage over the other methods.

Figure 5.20 shows the reconstruction errors for different interpolation techniques in the case of noise and outliers. In a) the rather unrealistic case of adding outliers
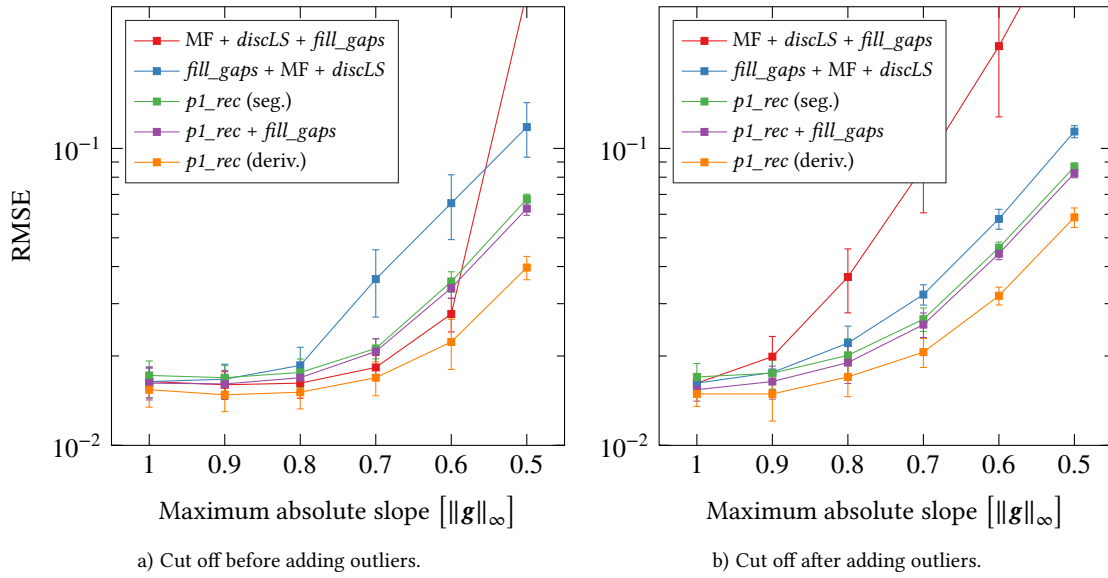
a) Cut off before adding outliers.

b) Cut off after adding outliers.

Figure 5.20 │ Reconstruction Errors of the 128-by-128 Cos2 Surface in the Case of Gaussian Noise, Outliers, and Interpolation ($\sigma = 7\,\%\|g\|_\infty$, **left:** $p_{\mathbf{out}} = 5\,\%$, $a_{\mathbf{out}} = 5\,\|g\|_\infty$, **right:** $p_{\mathbf{out}} = 3\,\%$ $a_{\mathbf{out}} = 0.8\,\|g\|_\infty$). Again, the spline methods are superior to the others. A problem of median filtering is the spreading of the gaps. However, without median filtering *discLS* is not robust to outliers.

after cutting off the gradient field is shown. Since the method *discLS* is not robust to outliers, median filtering is needed. This can be done before or after interpolating the data with *fill_gaps*. Median filtering before interpolation of the gradient is for small gaps the best way since then the outliers cannot influence the interpolation. Median filtering spreads the gaps in each dimension. For larger gaps this spreading results in larger reconstruction errors. Similar to the noise only case the derivative method *p1_rec* (deriv.) is superior to the other methods.

In b) the gradient fields were cut off after adding outliers. Though using small magnitude outliers, some pixel size gaps result from the cutting. Due to these additional gaps in contrast to a), the errors are larger even with this moderate corruption. Median filtering spreads the gaps and should be applied after interpolation. *p1_rec* (deriv.) provides the best reconstructions. Using *fill_gaps* is for the spline based methods needless. The result is similar to the spline interpolation, which is always computed.

5.8.2 Normalized Root-Mean-Squared Error

A disadvantage of the root-mean-squared error is its surface dependency. Even for equal sized surfaces the errors may differ in orders of magnitude. An error may be reasonable for one surface but indicate a totally false reconstruction for another. Thus, the root-mean-squared error can only be used to compare methods. If no method yields

Table 5.2 | NRMSE for Different Surfaces, Surface Sizes, and Corruptions ($a_{out} = 2\,\|g\|_\infty$). For equal-sized surfaces and similar gradient field corruption levels the normalized root-mean-squared error is quite stable. In contrast the root-mean-squared errors differed a lot, e.g., in Figure 5.13 and Figure 5.14.

Test Surface	m, n	$\sigma\left[\|g\|_\infty\right]$	p_{out}	NRMSE	
				discLS	*p1_rec* (seg.)
		-	-	$1.59 \cdot 10^{-3}$	$6.92 \cdot 10^{-4}$
cos2	64, 64	$5\,\%$	-	$(5.5 \pm 0.6) \cdot 10^{-3}$	$(6.9 \pm 1.0) \cdot 10^{-3}$
		$5\,\%$	$5\,\%$	$(1.1 \pm 0.1) \cdot 10^{-2\dagger}$	$(7.5 \pm 1.4) \cdot 10^{-3}$
		-	-	$2.27 \cdot 10^{-3}$	$8.56 \cdot 10^{-4}$
ramppeaks	64, 64	$5\,\%$	-	$(7.1 \pm 0.6) \cdot 10^{-3}$	$(7.9 \pm 1.2) \cdot 10^{-3}$
		$5\,\%$	$5\,\%$	$(1.3 \pm 0.1) \cdot 10^{-2\dagger}$	$(8.4 \pm 0.7) \cdot 10^{-3}$
		-	-	$3.89 \cdot 10^{-4}$	$9.38 \cdot 10^{-5}$
cos2	128, 128	$5\,\%$	-	$(2.8 \pm 0.3) \cdot 10^{-3}$	$(3.7 \pm 0.4) \cdot 10^{-3}$
		$5\,\%$	$3\,\%$	$(3.8 \pm 0.3) \cdot 10^{-3\dagger}$	$(3.7 \pm 0.3) \cdot 10^{-3}$
		-	-	$1.18 \cdot 10^{-4}$	$1.13 \cdot 10^{-6}$
g2sTestSurf	128, 128	$5\,\%$	-	$(2.1 \pm 0.2) \cdot 10^{-3}$	$(2.6 \pm 0.4) \cdot 10^{-3}$
		$5\,\%$	$3\,\%$	$(2.5 \pm 0.3) \cdot 10^{-3\dagger}$	$(2.9 \pm 0.4) \cdot 10^{-3}$
		-	-	$2.40 \cdot 10^{-4}$	$1.30 \cdot 10^{-5}$
sin2	128, 128	$5\,\%$	-	$(3.3 \pm 0.3) \cdot 10^{-3}$	$(4.1 \pm 0.5) \cdot 10^{-3}$
		$5\,\%$	$3\,\%$	$(4.5 \pm 0.4) \cdot 10^{-3\dagger}$	$(4.1 \pm 0.6) \cdot 10^{-3}$

† With median filter pre-processing.

an adequate reconstruction, the only way to exclude strong deviations is to eyeball the reconstructions. To avoid this eyeballing, another error measure is needed. The new error measure should provide consistent values, at least for equal sized surfaces and similar gradient field corruptions. The normalized root-mean-squared error

$$\text{NRMSE} = \frac{\text{RMSE}}{z_{max} - z_{min}} \tag{5.1}$$

may be an aspirant for this new measure. It is relatively stable for equal sized surfaces and similar corruptions how Table 5.2 shows.

With the normalized root-mean-squared error a rough error estimation in real-world data is possible. Only noise and outlier corruption have to be known approximately. If the surface is reconstructed erroneously, e.g., in the case of outliers and the use of a non-robust method, the normalized root-mean-squared error is useless. This is due to the division by the incorrectly estimated difference of maximum and minimum surface height. If the ground truth surface is known, the maximum and minimum ground truth surface height may be used.

Imaging Slope Gauge Data 6

All of the following water surface reconstructions were estimated from imaging slope gauge data. The data were measured in the wind-wave facility Aeolotron. The Aeolotron is an annular facility built to study air-sea interaction processes. Annular means infinite fetch. Thus, the development of the water waves is only limited by the finite water depth of about 1 m. For simulating a finite fetch in the annular facility a wave absorber can be used. Changing the absorber's position relative to the measurement section, the fetch dependent development of waves can be studied. All measurements were carried out by Christine Kräuter and Jakob Kunz in 2015. The final slope data were provided by Angelika Klein. The wind speed in the Aeolotron is controlled by setting a frequency for two axial ventilators.

Since four raw data images for calculating the water surface slopes are used, the influence of noise may be rather small. In contrast, the influence of outliers, e.g., due to bubbles, may be significant. The appearance of outliers may depend on the wind speed, on the shape of the waves, and on the calibration.

6.1 Examination of the Calibration

Calibrating a system means always another error source. A variation over time of the calibration may be possible and a recalibration can be time-consuming. Thus, it is useful to have a simple tool to examine the calibration. Since spatial localized errors cannot propagate to other segments, segmentation methods may be used.

6.1.1 Original Imaging Slope Gauge Data

At first, ISG data were used as provided. Only the signs of the slopes P in wind direction and Q in crosswind direction were changed. This simply means that wave crests and wave troughs were at the top and the bottom respectively.

Figure 6.1 shows water surface reconstructions of different methods for an axial ventilator frequency of 19.9 Hz and infinite fetch. The frequency corresponds to a wind speed of $5.8\,\mathrm{m\,s^{-1}}$ at a reference position in the Aeolotron. For the parameters of the reconstruction methods see Appendix B.

a) *fc_ISG*
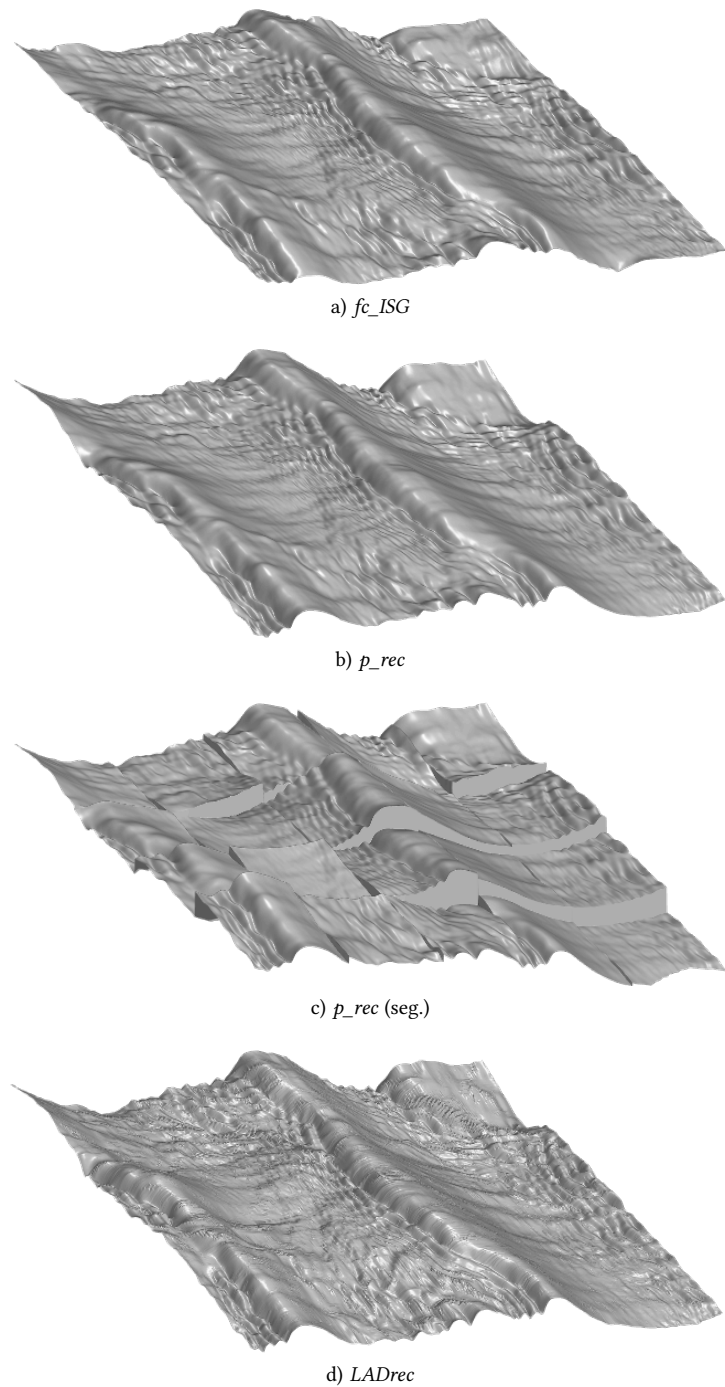

b) *p_rec*

c) *p_rec* (seg.)

d) *LADrec*

Figure 6.1 │ Water Surface Reconstructions from ISG Data for a Ventilator Frequency of 19.9 Hz and Infinite Fetch in the Aeolotron. The wind direction is from right to left. The wind speed, which was measured at a reference position in the Aeolotron, is 5.8 m s^{-1}. The resulting surface using *fc_ISG* shows unnatural periodic boundaries as discussed in section 4.1. Using *fc_xiong* or *discLS* result in to *p_rec* similar reconstructions. The segmentation method shows distinctive depth discontinuities.

The single segments of the segmentation method do not fit together. The reconstruction with *LADrec* shows some small-scale artifacts. The reconstruction with *fc_ISG* is shown, since this algorithm was used for former reconstructions from ISG data. The use of this algorithm is of course not recommended because of the enforced periodic boundaries.

6.1.2 Coordinate System Orientation Correction

The segment discontinuities and the artifacts of *LADrec* could be reproduced using test data with a sign-changed gradient field component in one of the two dimensions. The appearance of discontinuities becomes clear looking at the integrability condition, Eq. 4.2. Thus, in Figure 6.2 reconstructions from the negative slope in wind direction $-\boldsymbol{P}$ and the slope in crosswind direction $\boldsymbol{Q}$ are shown for the same data as in Figure 6.1. The discontinuities are much smaller. In the region front right there are still small discontinuities. This may indicate a calibration error.

The wrong sign of the slope in crosswind direction $\boldsymbol{P}$ may originate from different coordinate system orientations. The slope coordinates may built a left-hand system and the surface coordinates a right-hand system. Flipping of the gradient field components along the wind direction axis is equivalent to the described changing of one sign. Anyway, before applying surface reconstruction algorithms, the provided slope data need to get flipped along the wind direction axis. So far, this prerequisite has been stated due to the a priori expectation of the resulting wave fields. The new segmentation methods provide a qualitative measure to verify if a coordinate system orientation correction is needed. Without a segmentation method, it may be difficult to decide if given data are in for the reconstruction methods correct form. Parasitic capillary waves are with and without the orientation correction on the correct, leeward side of the waves. Even with knowledge of water wave theory, it may be difficult to decide which reconstructions are correct. With the segmentation method it seems clear that the orientation corrected reconstruction is the right one.

Especially for external imaging slope gauge data it is helpful to check the data with segmentation methods. In the calibration a coordinate system orientation could have been used which agrees with the orientation used in the chosen reconstruction algorithm.

6.1.3 Zero Slope Correction

Since the mean slope of the water surface over a longer time period is not zero and shows some inhomogeneities, an additional zero slope correction image has been subtracted from the slope data so far. Here is evaluated if this correction improves the surface reconstruction. In addition, the need of this correction may be called into question if the reconstruction is worsened.

Figure 6.3 shows mean slope images, or zero slope images, that were estimated for wind and crosswind direction from 10 Hz ventilator frequency data with 1.82 m fetch.
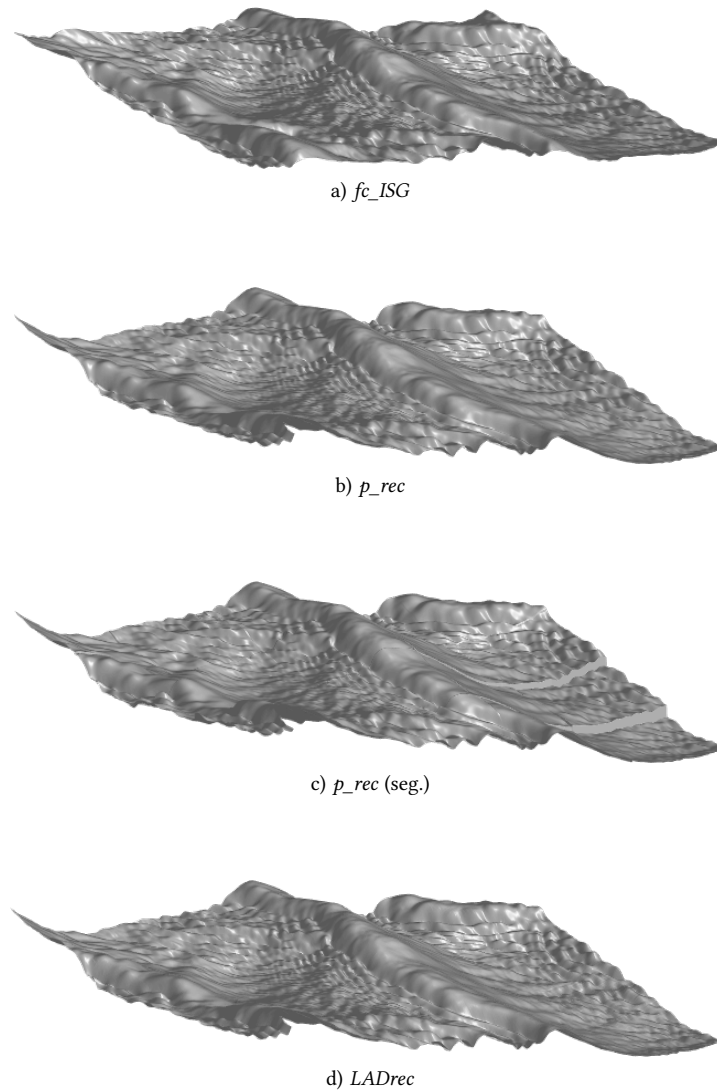
a) *fc_ISG*

b) *p_rec*

c) *p_rec* (seg.)

d) *LADrec*

Figure 6.2 │ Water Surface Reconstructions from Coordinate System Orientation Corrected ISG Data for a Ventilator Frequency of 19.9 Hz in the Aeolotron. Data, viewing angles and scales are the same as in Figure 6.1. The depth discontinuities in the segmentation reconstruction almost vanished. However, in the front right are still discontinuities. This may indicate calibration errors. The artifacts in the reconstruction with *LADrec* disappeared. Since the reconstruction is similar to the *p_rec* reconstruction, there are no outliers in the used data.

a) Wind direction: $-P_0$ b) Crosswind direction: Q_0
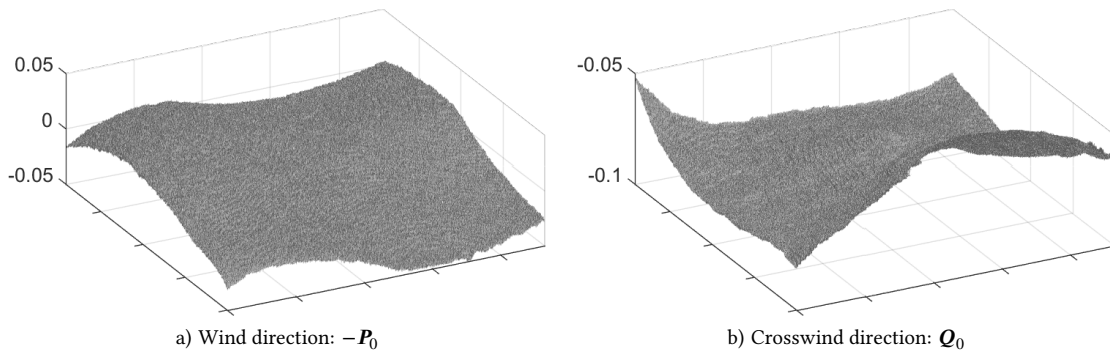
Figure 6.3 │ Zero Slope Images for the Wind and Crosswind Direction. The zero slopes images were estimated from 250 images for each slope component. Data with a ventilator frequency of 10 Hz and 1.82 m fetch were used. The corresponding wind speed at the reference position was 3 m s^{-1}. The images $-P$ in wind direction and Q in crosswind direction are nonuniform. The means of these images are non-zero. Adding scaled versions of these zero slope images to test data results in depth discontinuities for the segmentation methods.
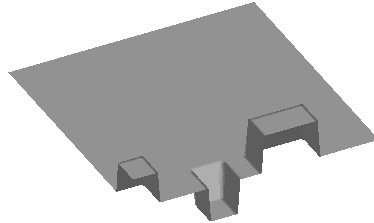
Figure 6.4 │ Simple Pattern to Reconstruct Depth Discontinuities in the Segmentation Methods. Adding this pattern to test data gradient fields yields depth discontinuities in the front segments for segmentation methods. A linear increasing or constant offset does not induce discontinuities, some spatial restriction seems to be required.

The waves in this dataset were rather small since the fetch was small and the wind velocity of 3 m s^{-1} at the reference position was low. So, the pixel-wise averaging over the 250 images for each slope component should provide usable zero slope images. Both zero slope images are nonuniform and have non-zero means. Adding the scaled zero slope images to test data yields similar segment discontinuities as in Figure 6.2. This indicates that the reconstruction without a zero slope correction is not a physically sound one. Adding a pattern such as shown in Figure 6.4 to test data results in discontinuities also. Adding constant or linear increasing offsets yields no discontinuities. Consequently, segmentation methods can only be used to detect some kind of calibration errors.

After subtracting the zero slope images from the gradient data used in Figure 6.2, the reconstructed segment discontinuities were smaller again. The coordinate system orientation and zero mean corrected reconstructions are shown in Figure 6.5. The discontinuities are hardly visible like in the tests in Chapter 5. Also, the mean rise of the surface looks more realistic.

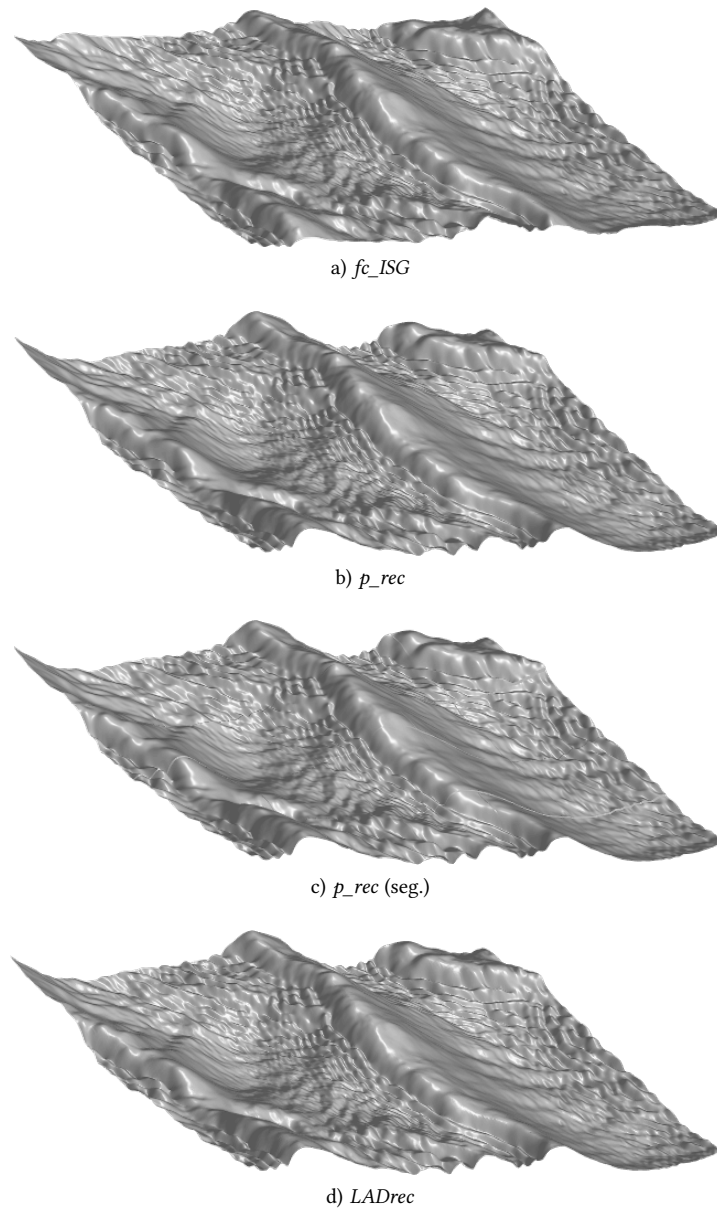a) *fc_ISG*

b) *p_rec*

c) *p_rec* (seg.)

d) *LADrec*

Figure 6.5 | Water Surface Reconstructions from Coordinate System Orientation and Zero Slope Corrected ISG Data for a Ventilator Frequency of 19.9 Hz in the Aeolotron. Data, viewing angles and scales are the same as in Figure 6.1 and Figure 6.2. After the corrections, discontinuities are hardly visible. This indicates to use the corrections. Without using a segmentation method it is difficult to decide if the uncorrected or the corrected reconstructions represent the true water surface. The differences are significant.

Another way for checking the calibration is to cut off certain slopes and compare the reconstruction with the one without gaps. Considering no corrections yielded a tilted surface in comparison to the full reconstruction. Considering both corrections, almost no tilt was visible. Cutting off slopes in corrupted test data did not result in tilts. Again, this recommends to use both corrections.

Final Comparison

Figure 6.6 shows a final comparison between a coordinate system orientation and zero slope corrected, and an uncorrected water surface reconstruction. The corrected surface reconstruction looks more realistic, but this is also due to the chosen viewing angles and the shading. The differences of the surfaces depend on the wind speed and the fetch. However, it is useful to have the possibility of using segmentation methods. Even without knowledge of water wave theory, incorrect reconstructions can be identified.

For the further analysis of the provided imaging slope gauge data, the coordinate system orientation correction and the zero slope correction were always applied. The subtraction of the zero slope images is only applicable for an at least approximately linear dependency in the calibration.

6.1.4 Further Issues

Infrequently, even after the corrections some discontinuities in the segmentation reconstructions appeared. In Figure 6.7 a reconstruction with a depth discontinuity in the front right segment is shown. The time series in Figure 6.8 shows an evolving depth discontinuity in the left. Using the method *LADrec* yields artifacts. The segment depth discontinuities and the artifacts may rely on non-integrable elements in the gradient field. In least squares based methods smoothing such as shown in Figure 5.12 appears.

The infrequent discontinuities do not seem to be spatially localized or slope dependent. Maybe some small dirt particles or bubbles influenced the measurement locally and temporally. A calibration error can not be excluded.
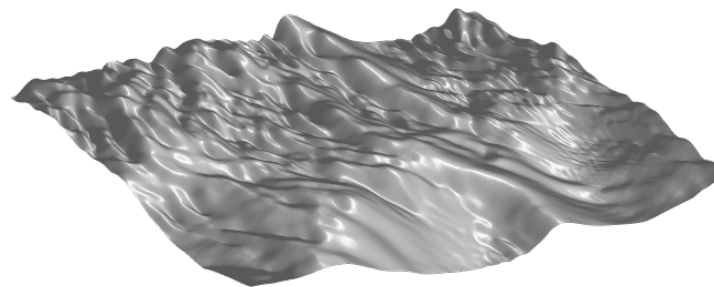
6.2 Comparison of the Reconstruction Methods

Eyeballing the reconstructions of the least squares based methods *fc_xiong*, *discLS*, and *p_rec* yielded no differences. Even median filtering did not affect the reconstruction in most cases. This is due to the smooth water surface and the good sampling. Choosing higher smoothing for *p_rec* damps the capillary waves and small-scale structures. An advantage of spline methods may be the intrinsic spline representation of the surface.

Using the former used algorithm *fc_ISG*, e.g., in Kiefhaber et al. (2014), yields unnatural deformed surfaces. This is because of the already described periodic boundaries enforcing. The mirroring of the gradient fields proposed from Balschbach (2000) must not be
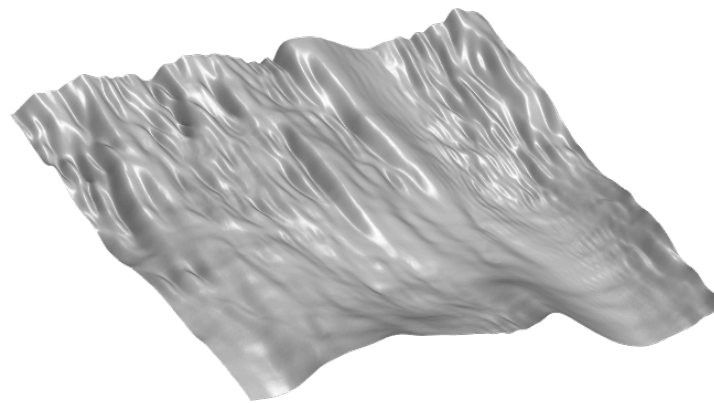
a) Original ISG data

b) Corrected ISG data

Figure 6.6 │ Comparison of Reconstructions from ISG Data for a Ventilator Frequency of 12.6 Hz and Infinite Fetch in the Aeolotron. The wind blows from the right to the left. The wind speed is $3.8\,\mathrm{m\,s^{-1}}$ at the reference position in the Aeolotron. Data, viewing angles and scales are the same for both reconstructions. The reconstructions differ in inclination, small-scale and large-scale structures. The corrected surface reconstruction looks more realistic, but this is also due to the chosen viewing angles. Shown are reconstructions with the algorithm *p_rec*.
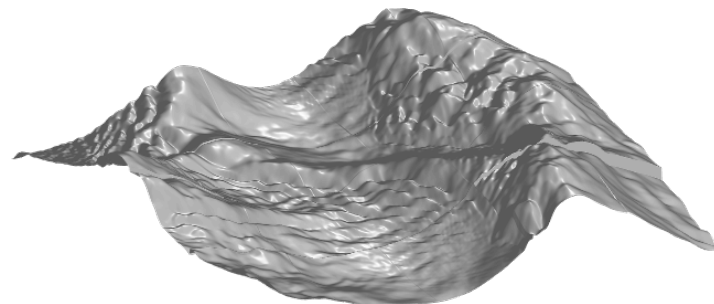

Figure 6.7 │ Water Surface Reconstruction from Corrected ISG Data for a Ventilator Frequency of 25.1 Hz and 2.79 m Fetch in the Aeolotron. The wind blows from the right. The wind speed is $7.2\,\mathrm{m\,s^{-1}}$ at the reference position. Shown is a reconstruction with the algorithm *p_rec* (seg.). A depth discontinuity in the front right segment is visible. The rest of the surface shows no discontinuities.
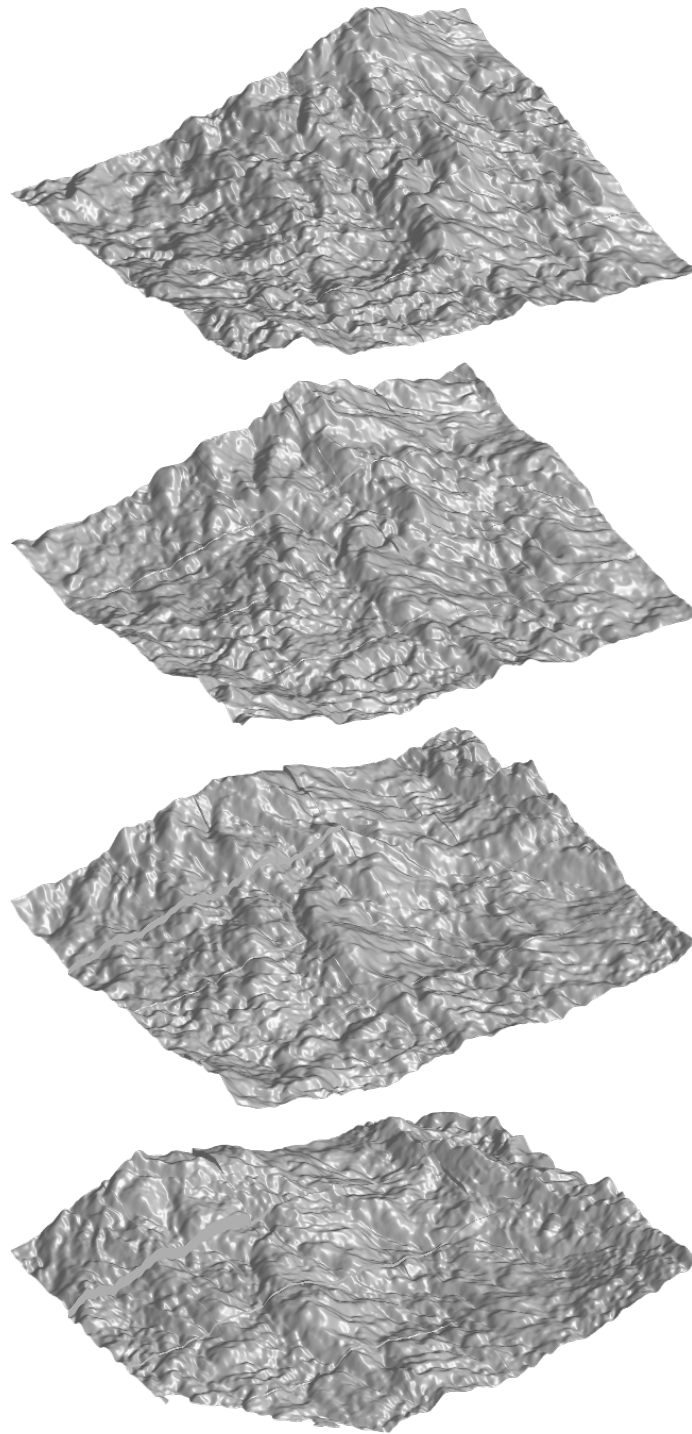
Figure 6.8 │ Water Surface Time Series from Corrected ISG Data for a Ventilator Frequency of 50 Hz and Infinite Fetch in the Aeolotron. The wind comes from the right. The wind speed is 11.3 m s^{-1} at the reference position. Shown are reconstructions with the algorithm *p_rec* (seg.). The first two reconstructions contain almost no discontinuities, whereas the last two show discontinuities on the left side.

confused with the embedding applied in *fc_xiong*. Rocholz (2008) detected artifacts using mirroring. The right embedding, e.g., in Bon et al. (2012), yields no artifacts.

The parameters of the spline methods and of the regularized LAD methods are in Appendix B. For surfaces with very small-scale structures the smoothing parameters of the spline methods may be too high. For the major part of the data the parameters were adequate. The wanted smoothing may be application dependent as well.

6.2.1 Need of LAD Based Methods

Least absolute deviations based methods are needed if there are outliers in the gradient fields. Another possibility is median filter pre-processing. The LAD based methods are superior to the median filter pre-processing in the case of depth discontinuities. Water surfaces should not contain depth discontinuities but discontinuities may result from the calibration.

For the provided data no differences between the least squares based methods with median filter pre-processing and without the pre-processing could be found. The provided imaging slope gauge data are well sampled. Thus, median filtering does not worsen the reconstruction quality in the absence of outliers. This better applicability for better sampled surfaces was already mentioned in section 5.8. Combining median filter pre-processing and, e.g., the fast algorithm *fc_xiong* yields a fast method, that is robust to outliers. If gaps are in the data, the algorithms *discLS* or *p_rec* may be combined with median filter pre-processing.

The segmentation methods *LADrec3* (seg.) and *p1_rec* (seg.) produced no significant differences compared to *p_rec* (seg.). Sometimes the depth discontinuities of the segments looked to some degree different. This is simply due to the different response to depth discontinuities of the L^1-norm based methods. In addition, median filter pre-processing does not smooth out the well sampled structures. So, the need of LAD based methods for the provided imaging slope data is called into question.

An open question is if the calibration of the imaging slope gauge or the estimation of the slopes from the raw data may be responsible for the non-existence of outliers. Smoothing data containing outliers would result in similar reconstructions for least squares and for least absolute deviations based methods. An indication for smoothing in the slope data may be the absence of very small-scale structures and the smoothness of the small-scale structures in Figure 6.8. However, this may also result from bubbles. The surfaces shown in Figure 6.8 may be physical correct reconstructions as well.

6.2.2 Bubbles

In Figure 6.9 an artifact in the reconstructed surface is visible. This artifact may result from a bubble in the light path of the imaging slope gauge. The bubble refracted the light and changed the measured slope. The artifact is method independent since it is

spatially too extended to be handled as a outlier. The shown artifact was tied to its place for a few reconstructions. Then it disappeared. The bubble is supposed to be in the bulk of the water or at the bottom of the facility. Otherwise, the artifact would have moved with the surface waves.

Using a MATLAB built-in edge detector, circular artifacts can be detected. After cutting off the region around the artifact in the gradient data, a reconstruction without artifact is possible. An interpolated reconstruction without the artifact is shown in Figure 6.9 also. The influence of the artifact is only local since the rest of the surface is the same.

Figure 6.10 shows two artifacts which may also result from bubbles. This time the bubbles have to be closer to the surface since they are moving. One artifact changes its shape to a circular wave like pattern. This pattern may be a diffraction pattern or simply a bubble bursting at the water surface. A bursting bubble may induce a small amplitude circular wave. Artifacts occur more frequently at higher wind speeds. Then, the probability for breaking waves, which may entrap bubbles in the water, is higher.
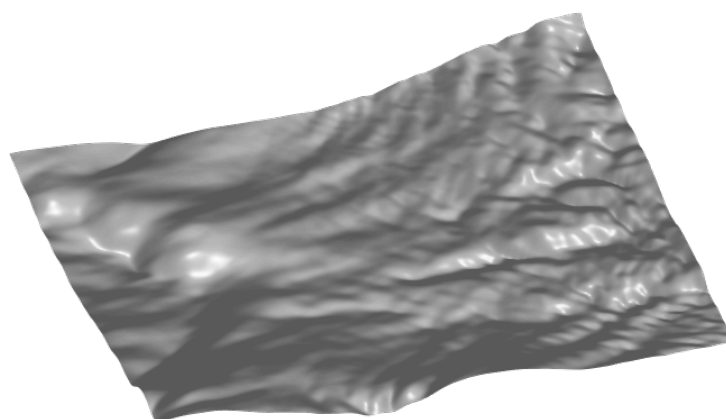
6.2.3 Interpolation

In section 5.8 it was shown that the new spline methods are superior to the other methods in the interpolation case. For the used imaging slope gauge gaps occur if the water surface slopes are greater than $26.3°$ in alongwind and $19.6°$ in crosswind direction. Unfortunately, no slope data with adequate gaps are available. In the 50 Hz ventilator frequency dataset only one pixel sized gaps occur. So, no reasonable interpolation comparison was possible.

6.3 Fetch Dependency of Wind Waves

The development of wind induced waves is fetch dependent until they are in equilibrium with the forcing wind. Figure 6.11 shows an evolving wave field for different fetches at $3.8\,\mathrm{m\,s^{-1}}$ wind speed in the Aeolotron. The waves grow with the fetch. In addition, the wave field looks more regular for larger fetches. For the 20.70 m fetch there are also waves with larger wavelengths, which are difficult to show in a single image. Using the former used algorithm *fc_ISG* would result in significantly different surfaces at the boundary area.
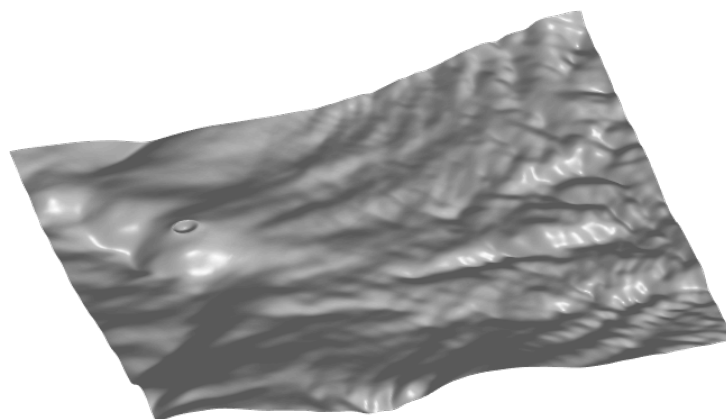
a) Reconstruction with *fc_xiong*

b) Interpolated reconstruction with *p_rec* (deriv.)

Figure 6.9 │ Artifact Correction in Water Surface Reconstruction. The wind comes from the right. The wind speed is $7.2\,\mathrm{m\,s^{-1}}$ at the reference position in the Aeolotron (25.1 Hz). The fetch is infinite. The shown section corresponds to a size of $10.4\,\mathrm{cm} \times 8.1\,\mathrm{cm}$. The diameter of the artifact is approximately 16 pixels corresponding to 3.7 mm. The artifact is at an almost fixed position until it disappears after a few images. It does not change its shape. The artifact may result from slop data that exhibited estimation errors due to bubbles in the light path of the imaging slope gauge.
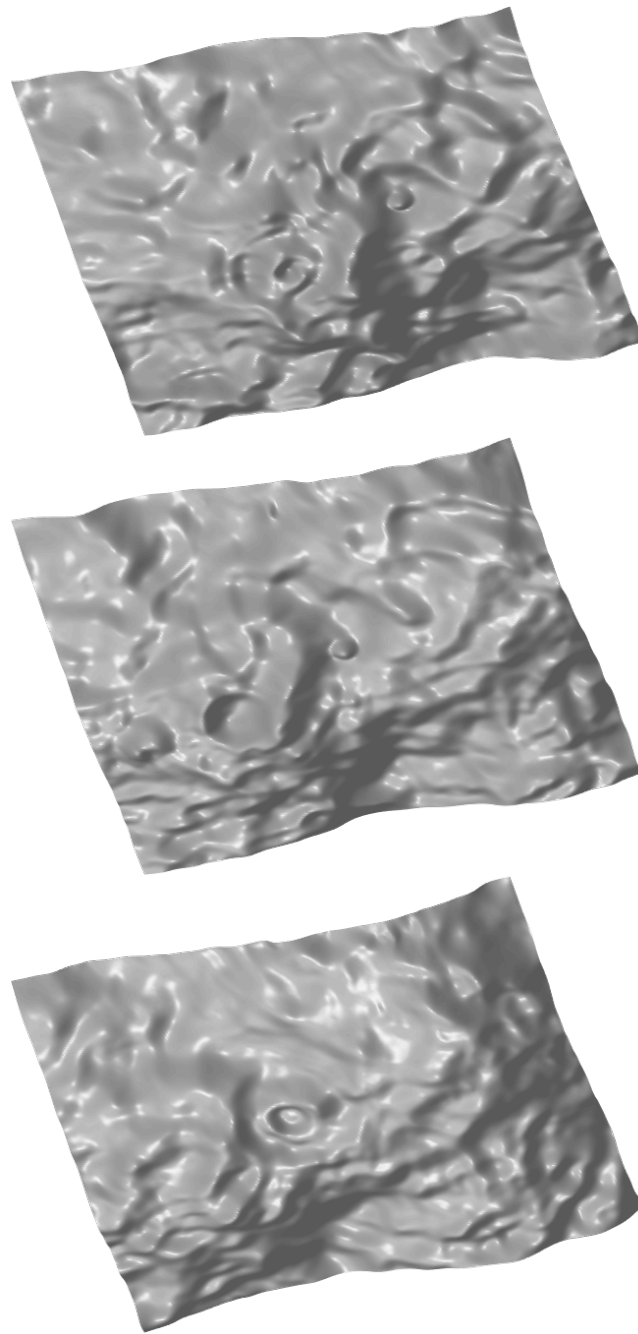
Figure 6.10 | Shape-changing Artifacts in a Surface Reconstruction Time Series. The wind comes from the right. The wind speed is $11.3\,\mathrm{m\,s^{-1}}$ at the reference position. The fetch is infinite. For every reconstruction the same $5.8\,\mathrm{cm} \times 5.8\,\mathrm{cm}$ section is shown. The time step between the images is $0.66\,\mathrm{ms}$. In contrast to the artifact in Figure 6.9, the artifacts shown here move with the surface waves. One artifact is changing its shape to a diffraction pattern. Maybe this pattern is no artifact but simply a bubble bursting at the surface. This may induce a small amplitude circular wave.
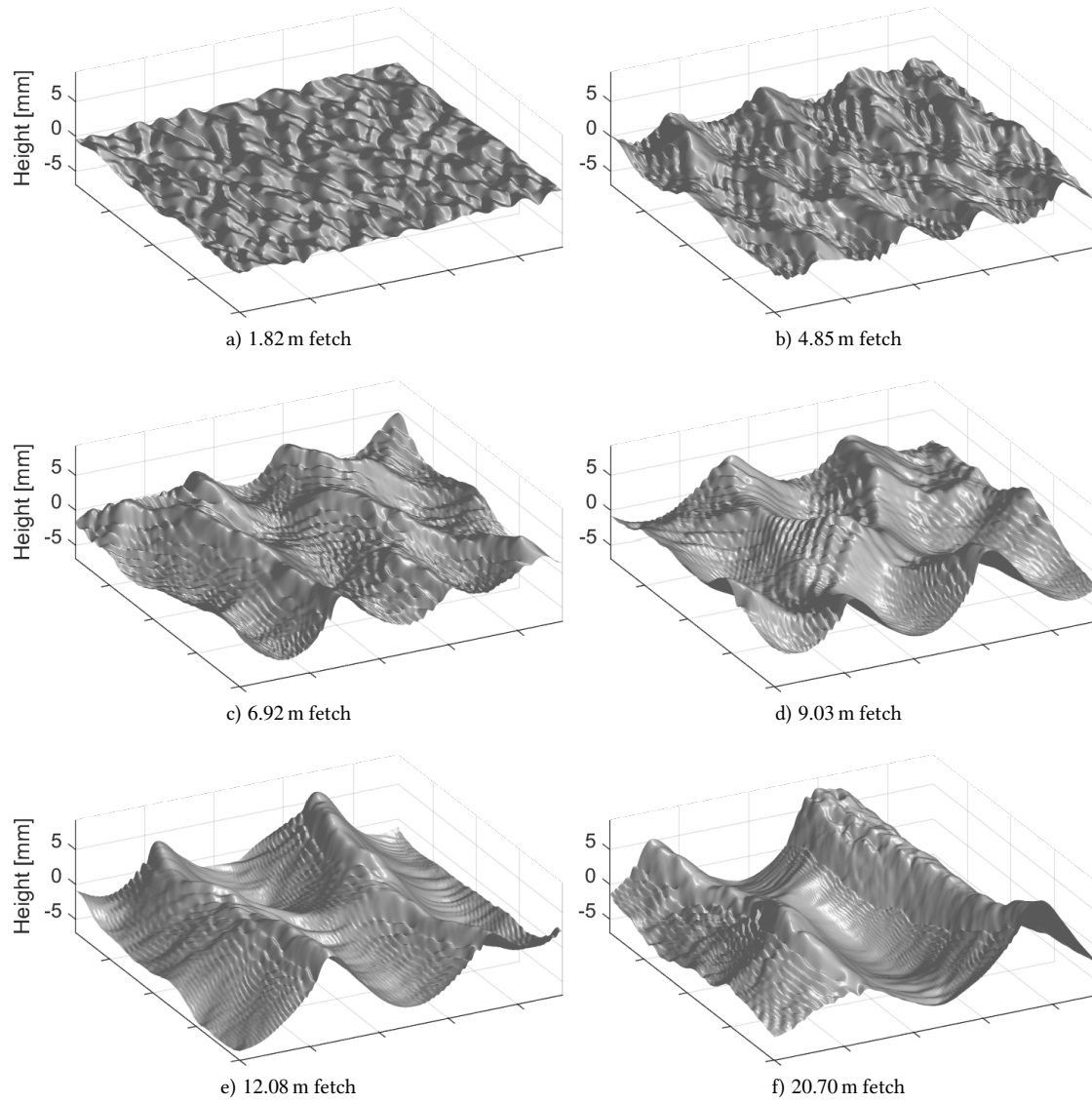
Figure 6.11 │ Evolving Wave Field for Different Fetches and a Ventilator Freqency of 12.6 Hz in the Aeolotron. The wind comes from the right. The wind speed is 3.8 m s^{-1} at the reference position in the Aeolotron. The waves grow with the fetch. For the 20.70 m fetch there are also waves with larger wavelength as shown.

Conclusion and Outlook 7

7.1 Conclusion

Gradient-Based Surface Reconstruction

New gradient-based surface reconstruction techniques were developed (section 4.11). In the reconstruction error and computation time analysis in Chapter 5 they were compared with conventional methods. The new methods are more accurate than the established algorithm for processing imaging slope gauge data. The established algorithm showed extensive boundary effects for non-periodic boundaries. Incomplete gradient fields no longer need to be interpolated before reconstructing the surface. The new methods are able to handle non-rectangular domains. The possibility of surface reconstruction without interpolation of incomplete gradient fields offers more options. In the reconstruction error analysis, it was shown that the new spline based methods are superior to other methods in the case of outliers, and concerning interpolation (section 5.8). In other cases, they were at least as accurate as the other methods, after adjusting parameters.

In the case of gradient fields corrupted by Gaussian noise, least squares based methods are recommended. They are fast and accurate (see section 5.7 and section 5.8). If a gradient field is corrupted by outliers, least absolute deviations based methods are superior to the least squares methods. While least absolute deviations based methods are robust to outliers, they are generally not as computationally efficient as least squares methods. Surfaces containing depth discontinuities are smoothed out using least squares based methods since discontinuities are non-integrable (section 5.6). Least absolute deviations based methods show staircase artifacts and can be used to detect depth discontinuities. The problem can be solved by segmentation of the gradient field into segments without discontinuity.

So far, it seems that combining pre-processing of gradient fields with fast non-robust surface reconstruction methods is not considered in literature. The combination of median filtering with a fast least squares method resulted in a fast method that is robust to outliers (section 5.5). However, median filtering may smooth structures slightly, which depends on the sampling of the surface. For well sampled or smooth surfaces almost no degradation due to median filtering could be found. In the case of noise, pre-processing does not need to be considered since improvements are rather small.

When comparing the carried out reconstruction error analysis to analyses in literature, the following aspects should be considered:

- There is no standard error measure in literature.

- If reconstructions are not shifted to the reference level of the ground truth, the resulting error analyses are non-representative. The shift may be method-dependent.

- Some methods are only robust to outliers for particular outlier distributions, e.g., the diffusion method of Agrawal et al. (2006). Estimating a single reconstruction only would result in a non-representative error analysis.

- For the benchmark test surface *ramppeaks*, often simple forward-differences are used to compute the uncorrupted gradient fields. In doing so, only forward-differences based methods yield low reconstruction errors since these methods compensate a half-pixel shift. This may result in an insignificant error analysis.

- The fact, that the discrete Fourier transform periodizes the reconstructed surface artificially, which results in wrong errors for the method of Frankot and Chellappa (1988), is almost never recognized. Thus, sometimes it is not clear if newly proposed methods really offer an improvement to a proper implementation of that method.

Application to Imaging Slope Gauge Data

Selected gradient-based surface reconstruction methods were applied to imaging slope gauge data measured in the wind-wave facility Aeolotron in Heidelberg. Using segmentation methods, it was shown that a coordinate system orientation correction is necessary to apply the reconstruction methods correctly (section 6.1).

Even after a coordinate system orientation correction, the reconstructions with segmentation methods showed distinct depth discontinuities. These discontinuities resulted from the calibration of the used imaging slope gauge. Zero slope images estimated from data with small waves were nonuniform (section 6.1). Adding these zero slope images to synthetic test data resulted in similar depth discontinuities in reconstructions. After a zero slope correction, in most reconstructions there were no depth discontinuities visible. Infrequently, some discontinuities evolved and vanished with time. This indicates either another calibration inaccuracy or other measurement errors.

Without the new segmentation methods, it is difficult to decide if water surface reconstructions are correct. Least squares based methods smooth discontinuities. Least absolute deviations based methods show only small artifacts. Thus, segmentation provides a fast and powerful tool for the examination of an imaging slope gauge calibration.

In a comparison of reconstruction methods for imaging slope gauge data, almost no differences between least squares and least absolute deviations based methods, and median filter pre-processing could be found (section 6.2). Thus, no outliers seem to be in the provided imaging slope gauge data. Due to the good sampling and the smoothness of the water surface, median filter pre-processing did not result in additional smoothing.

Bubbles in the light path of the imaging slope gauge may result in circular artifacts. In addition, they can burst at the surface and cause small circular waves. All tested reconstruction methods responded similar to bubbles. Detecting artifacts and cutting off their region in the gradient data resulted in undisturbed reconstructions, which were outside of an artifact region similar to the primary reconstructions. Thus, single bubbles do only result in local artifacts and do not propagate. After interpolation, a smooth and complete surface can be obtained. The bubbles in the data are too big to handle them as outliers. However, in other cases may arise the need for handling smaller bubbles.

At last, example water surface reconstructions for different fetches were given as an application (section 6.3). Wave fields obtained with the established algorithm for processing imaging slope gauge data would look significantly different. The enforcement of periodic boundary conditions would alter the whole surface.

7.2 Outlook

For future measurements the calibration of the imaging slope gauge in the Aeolotron can be examined quickly using the newly developed segmentation methods. The least absolute deviations based methods can be used to detect unphysical depth discontinuities as well. Another way for the examination of the calibration may be the cutting off of certain slope data. Then the reconstruction could be compared to the reconstruction from the full gradient field.

In the Aeolotron, a laser height camera is installed (J. Horn, 2013). With the laser height camera the unknown integration constant of the surface normal integration problem can be obtained. Using two laser height cameras, systematic errors such as tilts of the surface may be detected. The remaining rare depth discontinuities in the segmentation methods may correlate with the absolute surface height. So far, no time information is used in the new developed spline based reconstruction methods. Using this information may improve computational efficiency and reduce bubble induced artifacts.

Imaging slope gauge data can be used to estimate the mean square slope of a wave field. In the surface reconstruction problem, information of both slope components is used. Thus, the slopes related to the reconstructed water surface may be suitable for a mean square slope analysis as well. Additionally, slope data that exhibited estimation errors due to bubbles may be corrected. It may be instructive to draw a comparison between directly estimated mean square slope data and slope data related to reconstructed surfaces.

In the analysis of data taken during recent measurements at the SUSTAIN facility in Miami under hurricane conditions, the new interpolation methods and the new methods, that are robust to outliers, may show their advantages. No telecentric measurement setup was used in this experiment. Hence, the height dependent calibration may be improved by combining laser height camera information with the surface reconstruction information iteratively.

References

Agrawal, A., Raskar, R., & Chellappa, R. (2006). What is the range of surface reconstructions from a gradient field? In *Computer Vision - ECCV 2006* (pp. 578–591). Springer. doi:10.1007/11744023_45

Antensteiner, D., Štolc, S., Valentín, K., Blaschitz, B., Huber-Mörk, R., & Pock, T. (2017). High-precision 3d sensing with hybrid light field & photometric stereo approach in multi-line scan framework. *Electronic Imaging, 2017*(9), 52–60. doi:10.2352/ISSN.2470-1173.2017.9.IRIACV-268

Babanin, A. (2011). *Breaking and Dissipation of Ocean Surface Waves*. Cambridge University Press. doi:10.1017/CBO9780511736162

Badri, H. & Yahia, H. (2016). A non-local low-rank approach to enforce integrability. *IEEE Transactions on Image Processing, 25*, 3562–3571. doi:10.1109/TIP.2016.2570548

Badri, H., Yahia, H., & Aboutajdine, D. (2014). Robust surface reconstruction via triple sparsity. In *2014 IEEE Conference on Computer Vision and Pattern Recognition* (pp. 2291–2298). doi:10.1109/CVPR.2014.293

Bähr, M., Breuß, M., Quéau, Y., Boroujerdi, A. S., & Durou, J.-D. (2017). Fast and accurate surface normal integration on non-rectangular domains. *Computational Visual Media*, 1–23. doi:10.1007/s41095-016-0075-z

Balschbach, G. (2000). *Untersuchungen statistischer und geometrischer Eigenschaften von Windwellen und ihrer Wechselwirkungen mit der wasserseitigen Grenzschicht* (Doktorarbeit, Ruprecht-Karls-Universität Heidelberg). doi:10.11588/heidok.00002473

Balzer, J. & Mörwald, T. (2012). Isogeometric finite-elements methods and variational reconstruction tasks in vision - a perfect match. In *2012 IEEE Conference on Computer Vision and Pattern Recognition* (pp. 1624–1631). doi:10.1109/CVPR.2012.6247855

Banner, M. L. & Phillips, O. M. (1974). On the incipient breaking of small scale waves. *Journal of Fluid Mechanics, 65*, 647–656. doi:10.1017/S0022112074001583

Barrodale, I. & Roberts, F. D. K. (1973). An improved algorithm for discrete l1 linear approximation. *SIAM Journal on Numerical Analysis, 10*, 839–848. doi:10.1137/0710069

Björck, Å. (2015). *Numerical Methods in Matrix Computations*. Texts in Applied Mathematics. Springer. doi:10.1007/978-3-319-05089-8

Bon, P., Monneret, S., & Wattellier, B. (2012). Noniterative boundary-artifact-free wavefront reconstruction from its derivatives. *Appl. Opt. 51*, 5698–5704. doi:10.1364/AO.51.005698

Boyd, S. & Vandenberghe, L. (2009). *Convex Optimization* (7th ed.). Cambridge University Press.

Brooks, M. J. & Horn, B. K. P. (1985). Shape and source from shading. In *Proceedings of International Joint Conference on Artificial Intelligence* (pp. 932–936).

Burden, R. L. & Faires, J. D. (2011). *Numerical Analysis* (9th ed.). Cengage Learning.

Caulliez, G. (2013). Dissipation regimes for short wind waves. *Journal of Geophysical Research: Oceans, 118*, 672–684. doi:10.1029/2012JC008402

Crapper, G. D. (1957). An exact solution for progressive capillary waves of arbitrary amplitude. *Journal of Fluid Mechanics, 2*, 532–540. doi:10.1017/S0022112057000348

de Boor, C. (2001). *A Practical Guide to Splines* (rev. ed.). Applied Mathematical Sciences Vol. 27. Springer.

Deike, L., Popinet, S., & Melville, W. K. (2015). Capillary effects on wave breaking. *Journal of Fluid Mechanics, 769*, 541–569. doi:10.1017/jfm.2015.103

Du, Z., Robles-Kelly, A., & Lu, F. (2007). Robust surface reconstruction from gradient field using the l1 norm. In *9th Biennial Conference of the Australian Pattern Recognition Society on Digital Image Computing Techniques and Applications (DICTA 2007)* (pp. 203–209). doi:10.1109/DICTA.2007.4426797

Duncan, J. H., Qiao, H., Philomin, V., & Wenz, A. (1999). Gentle spilling breakers: Crest profile evolution. *Journal of Fluid Mechanics, 379*, 191–222. doi:10.1017/S0022112098003152

Eilers, P. H. C., Currie, I. D., & Durbán, M. (2006). Fast and compact smoothing on large multidimensional grids. *Computational Statistics & Data Analysis, 50*, 61–76. doi:10.1016/j.csda.2004.07.008

Eilers, P. H. C. & Marx, B. D. (1996). Flexible smoothing with B-splines and penalties. *Statist. Sci. 11*, 89–121. doi:10.1214/ss/1038425655

Eilers, P. H. C. & Marx, B. D. (2010). Splines, knots, and penalties. *Wiley Interdisciplinary Reviews: Computational Statistics, 2*, 637–653. doi:10.1002/wics.125

Eilers, P. H. C., Marx, B. D., & Durbán, M. (2015). Twenty years of P-splines. *SORT, 39*(2), 149–186. Retrieved from http://www.raco.cat/index.php/SORT/article/view/302258/391947

Ellis, S. P. (1998). Instability of least squares, least absolute deviation and least median of squares linear regression. *Statist. Sci. 13*, 337–350. doi:10.1214/ss/1028905829

EMVA. (2016, December). EMVA Standard 1288: Standard for characerization of image sensors and cameras. release 3.1. Retrieved from http://www.emva.org/standards-technology/emva-1288/

Ettl, S., Kaminski, J., Knauer, M. C., & Häusler, G. (2008). Shape reconstruction from gradient data. *Appl. Opt. 47*, 2091–2097. doi:10.1364/AO.47.002091

Fattal, R., Lischinski, D., & Werman, M. (2002). Gradient domain high dynamic range compression. *ACM Trans. Graph. 21*, 249–256. doi:10.1145/566654.566573

Frankot, R. T. & Chellappa, R. (1988). A method for enforcing integrability in shape from shading algorithms. *IEEE Transactions on Pattern Analysis and Machine Intelligence*, *10*, 439–451. doi:10.1109/34.3909

Garbe, C. S., Rutgersson, A., Boutin, J., de Leeuw, G., Delille, B., Fairall, C. W., … Zappa, C. J. (2014). Transfer across the air-sea interface. In P. S. Liss & M. T. Johnson (Eds.), *Ocean-Atmosphere Interactions of Gases and Particles* (pp. 55–112). Springer. doi:10.1007/978-3-642-25643-1_2

Golub, G. H., Hansen, P. C., & O'Leary, D. P. (1999). Tikhonov regularization and total least squares. *SIAM Journal on Matrix Analysis and Applications*, *21*, 185–194. doi:10.1137/S0895479897326432

Gurobi Optimization, Inc. (2017). Gurobi optimizer reference manual. Version 7.0. Retrieved from http://www.gurobi.com

Hansen, M. F., Atkinson, G. A., Smith, L. N., & Smith, M. L. (2010). 3d face reconstructions from photometric stereo using near infrared and visible light. *Computer Vision and Image Understanding*, *114*, 942–951. doi:10.1016/j.cviu.2010.03.001

Härdle, W. (1990). *Applied Nonparametric Regresion*. Cambridge University Press.

Harker, M. & O'Leary, P. (2008). Least squares surface reconstruction from measured gradient fields. In *2008 IEEE Conference on Computer Vision and Pattern Recognition* (pp. 1–7). doi:10.1109/CVPR.2008.4587414

Harker, M. & O'Leary, P. (2011). Least squares surface reconstruction from gradients: Direct algebraic methods with spectral, tikhonov, and constrained regularization. In *CVPR 2011* (pp. 2529–2536). doi:10.1109/CVPR.2011.5995427

Harker, M. & O'Leary, P. (2013). Direct regularized surface reconstruction from gradients for industrial photometric stereo. *Computers in Industry*, *64*, 1221–1228. Special Issue: 3D Imaging in Industry. doi:10.1016/j.compind.2013.03.013

Harker, M. & O'Leary, P. (2015). Regularized reconstruction of a surface from its measured gradient field. *J Math Imaging Vis*, *51*, 46–70. doi:10.1007/s10851-014-0505-4

Horn, B. K. P. (1970). *Shape from shading: A method for obtaining the shape of a smooth opaque object from one view*. Cambridge, MA, USA: Massachusetts Institute of Technology.

Horn, B. K. P. & Brooks, M. J. (1986). The variational approach to shape from shading. *Computer Vision, Graphics, and Image Processing*, *33*, 174–208. doi:10.1016/0734-189X(86)90114-3

Horn, J. (2013). *Hochaufgelöste optische Wellenhöhenmessung am Aeolotron mit Laser-induzierter Fluoreszenz* (Bachelorarbeit, Ruprecht-Karls-Universität Heidelberg).

Iafrati, I. & Campana, E. F. (2005). Free-surface fluctuations behind microbreakers: Space–time behaviour and subsurface flow field. *Journal of Fluid Mechanics*, *529*, 311–347. doi:10.1017/S0022112005003472

References

Ikeuchi, K. (1981). Determining surface orientations of specular surfaces by using the photometric stereo method. *IEEE Transactions on Pattern Analysis and Machine Intelligence, PAMI-3*, 661–669. doi:10.1109/TPAMI.1981.4767167

Jähne, B. (2005). *Digital Image Processing* (6th ed.). Springer.

Jähne, B. (2012). *Digitale Bildverarbeitung: und Bildgewinnung* (7. Auflage). Springer. doi:10.1007/978-3-642-04952-1

Jähne, B., Klinke, J., & Waas, S. (1994). Imaging of short ocean wind waves: A critical theoretical review. *J. Opt. Soc. Am. A, 11*, 2197–2209. doi:10.1364/JOSAA.11.002197

Johnson, R. S. (1997). *A Modern Introduction to the Mathematical Theory of Water Waves*. Cambridge Texts in Applied Mathematics. Cambridge University Press. doi:10.1017/CBO9780511624056

Kang, D., Jang, Y. J., & Won, S. (2013). Development of an inspection system for planar steel surface using multispectral photometric stereo. *Optical Engineering, 52*. doi:10.1117/1.OE.52.3.039701

Ke, Q. & Kanade, T. (2005). Robust l1 norm factorization in the presence of outliers and missing data by alternative convex programming. In *2005 IEEE Computer Society Conference on Computer Vision and Pattern Recognition (CVPR'05)* (Vol. 1, pp. 739–746). doi:10.1109/CVPR.2005.309

Kiefhaber, D. (2014). *Optical measurement of short wind waves — from the laboratory to the field* (PhD thesis, Ruperto-Carola University of Heidelberg). doi:10.11588/heidok.00016304

Kiefhaber, D., Reith, S., Rocholz, R., & Jähne, B. (2014). High-speed imaging of short wind waves by shape from refraction. *J. Europ. Opt. Soc. Rap. Public. 9*. doi:10.2971/jeos.2014.14015

Komar, P. D. & Gaughan, M. K. (1972). Airy wave theory and breaker height prediction. In *Coastal engineering 1972* (Chap. 20, pp. 405–418). doi:10.1061/9780872620490.023

Kundu, P. K. & Cohen, I. M. (2008). *Fluid Mechanics* (4th ed.). Elsevier.

Melville, W. K. (1996). The role of surface-wave breaking in air-sea interaction. *Annual Review of Fluid Mechanics, 28*, 279–321. doi:10.1146/annurev.fl.28.010196.001431

Munk, W. H. (1949). The solitary wave theory and its application to surf problems. *Annals of the New York Academy of Sciences, 51*, 376–424. doi:10.1111/j.1749-6632.1949.tb27281.x

O'Sullivan, F. (1986). A statistical perspective on ill-posed inverse problems. *Statist. Sci. 1*, 502–518. doi:10.1214/ss/1177013525

O'Sullivan, F. (1988). Fast computation of fully automated log-density and log-hazard estimators. *SIAM J. Sci. and Stat. Comput. 9*, 363–379. doi:10.1137/0909024

Pérez, P., Gangnet, M., & Blake, A. (2003). Poisson image editing. *ACM Trans. Graph. 22*, 313–318. doi:10.1145/882262.882269

Quéau, Y. (2015). *Reconstruction tridimensionnelle par stéréophotométrie* (PhD thesis, Institut National Polytechnique de Toulouse). Retrieved from https://tel.archives-ouvertes.fr/tel-01261526

Quéau, Y. & Durou, J.-D. (2015). Edge-preserving integration of a normal field: Weighted least-squares, tv and l^1 approaches. In J.-F. Aujol, M. Nikolova, & N. Papadakis (Eds.), *Scale Space and Variational Methods in Computer Vision* (pp. 576–588). Springer. doi:10.1007/978-3-319-18461-6_46

Quéau, Y., Durou, J.-D., & Aujol, J.-F. (2017). *Normal Integration – Part I: A Survey*. working paper or preprint. Retrieved from https://hal.archives-ouvertes.fr/hal-01334349v2

Reddy, D., Agrawal, A., & Chellappa, R. (2009). Enforcing integrability by error correction using l1-minimization. In *2009 IEEE Conference on Computer Vision and Pattern Recognition* (pp. 2350–2357). doi:10.1109/CVPR.2009.5206603

Reinsch, C. H. (1967). Smoothing by spline functions. *Numerische Mathematik*, *10*, 177–183. doi:10.1007/BF02162161

Reith, S. (2014). *Spatio-temporal slope measurement of short wind waves under the influence of surface films at the Heidelberg Aeolotron* (Master's thesis, University of Heidelberg). doi:10.11588/heidok.00017697

Rocholz, R. (2008). *Spatio-temporal measurements of short wind-driven water waves* (PhD thesis, Ruperto-Carola University of Heidelberg). doi:10.11588/heidok.00008897

Sevcenco, I. S., Hampton, P. J., & Agathoklis, P. (2015). A wavelet based method for image reconstruction from gradient data with applications. *Multidimensional Systems and Signal Processing*, *26*, 717–737. doi:10.1007/s11045-013-0262-3

Simchony, T., Chellappa, R., & Shao, M. (1990). Direct analytical methods for solving poisson equations in computer vision problems. *IEEE Transactions on Pattern Analysis and Machine Intelligence*, *12*, 435–446. doi:10.1109/34.55103

Wei, T. & Klette, R. (2001). A new algorithm for gradient field integration. In *Image and Vision Computing New Zealand*. Retrieved from https://researchspace.auckland.ac.nz/handle/2292/2683

Wei, T. & Klette, R. (2002). Regularization method for depth from noisy gradient vector fields. Retrieved from https://researchspace.auckland.ac.nz/handle/2292/2850

Woodham, R. J. (1980). Photometric method for determining surface orientation from multiple images. *Optical Engineering*, *19*, 139–144. doi:10.1117/12.7972479

Wu, Z. & Li, L. (1988). A line-integration based method for depth recovery from surface normals. *Computer Vision, Graphics, and Image Processing*, *43*, 53–66. doi:10.1016/0734-189X(88)90042-4

Zappa, C. J., Asher, W. E., Jessup, A. T., Klinke, J., & Long, S. R. (2004). Microbreaking and the enhancement of air-water transfer velocity. *J. Geophys. Res. 109*. doi:10.1029/2003JC001897

Zhang, R., Tsai, P.-S., Cryer, J. E., & Shah, M. (1999). Shape-from-shading: A survey. *IEEE Transactions on Pattern Analysis and Machine Intelligence*, *21*, 690–706. doi:10.1109/34.784284

Zhang, X. & Cox, C. S. (1994). Measuring the two-dimensional structure of a wavy water surface optically: A surface gradient detector. *Experiments in Fluids*, *17*, 225–237. doi:10.1007/BF00203041

Convex Optimization A

A.1 Derivation of the Normal Equations

Least squares problem:

$$\text{minimize} \quad f_0(x) = \|Ax - b\|_2^2 = (Ax - b)^\top (Ax - b) \,, \qquad \text{(2.3 revisited)}$$

For an unconstrained convex problem the necessary and sufficient condition for x beeing optimal is (Boyd & Vandenberghe, 2009)

$$\frac{\mathrm{d}}{\mathrm{d}x} f_0(x) := \nabla f_0(x) = 0 \,. \qquad \text{(A.1)}$$

Based on the definition follows

$$\frac{\mathrm{d}}{\mathrm{d}x} x^\top y = \frac{\mathrm{d}}{\mathrm{d}x} y^\top x = y \,, \qquad \frac{\mathrm{d}}{\mathrm{d}x} x^\top x = 2\,x \,. \qquad \text{(A.2)}$$

Calculating the gradient

$$\frac{\mathrm{d}}{\mathrm{d}x} f_0(x) = \frac{\mathrm{d}}{\mathrm{d}x} (x^\top A^\top A x - x^\top A^\top b - b^\top A x + b^\top b) = 2\,A^\top A x - 2\,A^\top b \qquad \text{(A.3)}$$

and setting the gradient to zero yields the normal equations

$$A^\top A x^* = A^\top b \,. \qquad \text{(2.4 revisited)}$$

A.2 Least Absolute Deviations as a Linear Program

Least absolute deviations statistical optimality criterion:

$$\text{minimize} \quad f_0(x) = \|Ax - b\|_1 \,. \qquad \text{(2.7 revisited)}$$

Barrodale and Roberts (1973)

With the nonnegative variables $\boldsymbol{u}, \boldsymbol{v} \in \mathbb{R}_{\geq 0}^m, \boldsymbol{\gamma}, \boldsymbol{\delta} \in \mathbb{R}_{\geq 0}^n$, and $\mathbf{1} \in \mathbb{R}^m$ (vector whose elements are all 1) such that

$$\boldsymbol{b} - \boldsymbol{A}\boldsymbol{x} = \boldsymbol{u} - \boldsymbol{v} \, , \tag{A.4}$$

$$\boldsymbol{x} = \boldsymbol{\gamma} - \boldsymbol{\delta} \, , \tag{A.5}$$

the best L^1-norm approximation corresponds to an optimal solution to the standard form linear program (Barrodale & Roberts, [1973](#))

$$
\begin{aligned}
\text{minimize} \quad & \mathbf{1}^\top (\boldsymbol{u} + \boldsymbol{v}) \\
\text{subject to} \quad & \boldsymbol{b} = \boldsymbol{A}(\boldsymbol{\gamma} - \boldsymbol{\delta}) + \boldsymbol{u} - \boldsymbol{v} \, .
\end{aligned}
\tag{A.6}
$$

For some solvers reformulations are needed to bring the problem to the right form:

$$\tilde{\boldsymbol{A}} = \begin{pmatrix} \boldsymbol{A} & \boldsymbol{I}_m & -\boldsymbol{I}_m \end{pmatrix}, \quad \tilde{\boldsymbol{x}} = \begin{pmatrix} \boldsymbol{x} & \boldsymbol{u} & \boldsymbol{v} \end{pmatrix}^\top, \quad \tilde{\boldsymbol{f}}_0 = \begin{pmatrix} \boldsymbol{0} & \mathbf{1} & \mathbf{1} \end{pmatrix}^\top . \tag{A.7}$$

$\boldsymbol{0} \in \mathbb{R}^n$ is the zero vector. With these formulations [Eq. A.6](#) can be rewritten:

$$
\begin{aligned}
\text{minimize} \quad & \tilde{\boldsymbol{f}}_0^\top \tilde{\boldsymbol{x}} \\
\text{subject to} \quad & \tilde{\boldsymbol{A}}\tilde{\boldsymbol{x}} \leq \boldsymbol{b} \, .
\end{aligned}
\tag{A.6 revised}
$$

$\leq$ means componentwise less than or equal to. Solutions are the first n elements of $\tilde{\boldsymbol{x}}^*$.

Boyd and Vandenberghe (2009)

With $\boldsymbol{t}, \mathbf{1} \in \mathbb{R}^m$ the best L^1-norm approximation corresponds to an optimal solution to the inequality form linear program (Boyd & Vandenberghe, [2009](#))

$$
\begin{aligned}
\text{minimize} \quad & \mathbf{1}^\top \boldsymbol{t} \\
\text{subject to} \quad & -\boldsymbol{t} \leq \boldsymbol{A}\boldsymbol{x} - \boldsymbol{b} \leq \boldsymbol{t} \, .
\end{aligned}
\tag{A.8}
$$

For some solvers reformulations are needed to bring the problem to the right form:

$$\tilde{\boldsymbol{A}} = \begin{pmatrix} \boldsymbol{A} & -\boldsymbol{I}_m \\ -\boldsymbol{A} & -\boldsymbol{I}_m \end{pmatrix}, \quad \tilde{\boldsymbol{x}} = \begin{pmatrix} \boldsymbol{x} \\ \boldsymbol{t} \end{pmatrix}, \quad \tilde{\boldsymbol{b}} = \begin{pmatrix} \boldsymbol{b} \\ -\boldsymbol{b} \end{pmatrix}, \quad \tilde{\boldsymbol{f}}_0 = \begin{pmatrix} \boldsymbol{0} \\ \mathbf{1} \end{pmatrix} . \tag{A.9}$$

With this formulations [Eq. A.8](#) can be rewritten:

$$
\begin{aligned}
\text{minimize} \quad & \tilde{\boldsymbol{f}}_0^\top \tilde{\boldsymbol{x}} \\
\text{subject to} \quad & \tilde{\boldsymbol{A}}\tilde{\boldsymbol{x}} \leq \tilde{\boldsymbol{b}} \, .
\end{aligned}
\tag{A.8 revised}
$$

Parameters B

B.1 Segmentation

- 64-by-64 surface: two 39-by-64 segments.
- 128-by-128 surface: two 71-by-128 segments.
- 256-by-256 surface: two 135-by-256 segments.
- 512-by-512 surface: two 135-by-512 and two 142-by-512 segments.
- 760-by-930 surface: four 197-by-193, six 197-by-200, four 204-by-193, and six 204-by-200 segments.

Equal sized segments are not always possible but also not necessary. The overlap of two joining segments is 14 pixel in each case.

B.2 Computation Time Analysis

Gradient field corruptions:

- *ramppeaks* : $\sigma = 5\,\%\|g\|_\infty\,,\ p_{\text{out}} = 5\,\%\,,\ a_{\text{out}} = 3\,\|g\|_\infty$.
- *cos2*: $\sigma = 7\,\%\|g\|_\infty\,,\ p_{\text{out}} = 3\,\%\,,\ a_{\text{out}} = 2\,\|g\|_\infty$.

Parameters of *LADrec2* and *LADrec2* (seg.):

- 760-by-930 surface: $\lambda_x = \lambda_y = 0.25$.
- Else: $\lambda_x = \lambda_y = 0.6$.

Parameters of *LADrec3* and *LADrec3* (seg.):

- For all surfaces: $\lambda_x = 0.8$.

Parameters of *p_rec*:

- 64-by-64 surface: $k_x = k_y = 3,\, n_x = 64,\ \ n_y = 64,\ \ \lambda_x = 0.30,\, \lambda_y = 0.30.$
- 128-by-128 surface: $k_x = k_y = 3,\, n_x = 128,\, n_y = 128,\, \lambda_x = 0.50,\, \lambda_y = 0.50.$
- 256-by-256 surface: $k_x = k_y = 3,\, n_x = 128,\, n_y = 128,\, \lambda_x = 0.40,\, \lambda_y = 0.40.$

- 512-by-512 surface: $k_x = k_y = 3$, $n_x = 256$, $n_y = 256$, $\lambda_x = 0.40$, $\lambda_y = 0.40$.
- 760-by-930 surface: $k_x = k_y = 3$, $n_x = 300$, $n_y = 250$, $\lambda_x = 0.30$, $\lambda_y = 0.30$.

Parameters of *p1_rec*:

- 64-by-64 surface: $k_x = k_y = 3$, $n_x = 64$, $n_y = 64$, $\lambda_x = 0.30$, $\lambda_y = 0.30$.
- Else: $k_x = k_y = 3$, $n_x = 64$, $n_y = 64$, $\lambda_x = 0.40$, $\lambda_y = 0.40$.

Parameters of *p1_rec* (seg.):

- 64-by-64 surface: $k_x = k_y = 3$, $n_x = 65$, $n_y = 55$, $\lambda_x = 0.30$, $\lambda_y = 0.35$.
- 128-by-128 surface: $k_x = k_y = 3$, $n_x = 65$, $n_y = 55$, $\lambda_x = 0.30$, $\lambda_y = 0.35$.
- 256-by-256 surface: $k_x = k_y = 3$, $n_x = 65$, $n_y = 55$, $\lambda_x = 0.30$, $\lambda_y = 0.35$.
- 512-by-512 surface: $k_x = k_y = 3$, $n_x = 75$, $n_y = 55$, $\lambda_x = 0.45$, $\lambda_y = 0.40$.
- 760-by-930 surface: $k_x = k_y = 3$, $n_x = 45$, $n_y = 45$, $\lambda_x = 0.17$, $\lambda_y = 0.12$[1].

B.3 Reconstruction Errors

Parameters of *LADrec2*:

- For all surfaces: $\lambda_x = 0.6$.

Parameters of *LADrec3* and *LADrec3* (seg.):

- For all surfaces: $\lambda_x = 0.8$.

Parameters of *p_rec*:

- 64-by-64 surface: $k_x = k_y = 3$, $n_x = 64$, $n_y = 64$, $\lambda_x = 0.30$, $\lambda_y = 0.30$.
- 128-by-128 surface: $k_x = k_y = 3$, $n_x = 128$, $n_y = 128$, $\lambda_x = 0.50$, $\lambda_y = 0.50$.

Parameters of *p_rec* (deriv.):

- 128-by-128 surface: $k_x = k_y = 3$, $n_x = 128$, $n_y = 128$, $\lambda_x = 0.25$, $\lambda_y = 0.25$.

Parameters of *p1_rec*:

- 64-by-64 surface: $k_x = k_y = 3$, $n_x = 64$, $n_y = 64$, $\lambda_x = 0.30$, $\lambda_y = 0.30$.
- 128-by-128 surface: $k_x = k_y = 3$, $n_x = 64$, $n_y = 64$, $\lambda_x = 0.40$, $\lambda_y = 0.40$[2].

Parameters of *p1_rec* (seg.):

- 64-by-64 surface: $k_x = k_y = 3$, $n_x = 65$, $n_y = 55$, $\lambda_x = 0.30$, $\lambda_y = 0.35$.
- 128-by-128 surface: $k_x = k_y = 3$, $n_x = 65$, $n_y = 55$, $\lambda_x = 0.30$, $\lambda_y = 0.35$[3].

---

[1] If Gurobi finds no solution for a segment after 45 s, λ_x and λ_y are increased by 0.002 for this segment.
[2] $\lambda_x = \lambda_y = 0.399$ if Gurobi does not find a solution in a reasonable time.
[3] $\lambda_y = 0.3495$ if Gurobi does not find a solution in a reasonable time.

Parameters of *p1_rec* (deriv.):

- 128-by-128 surface:　$k_x = k_y = 3, n_x = 64,\ \ n_y = 64,\ \ \lambda_x = 0.25, \lambda_y = 0.25.$

B.4 ISG Data

Parameters of *LADrec2* (seg.):

- $\lambda_x = \lambda_y = 0.25.$

Parameters of *LADrec3* (seg.):

- $\lambda_x = 0.8.$

Parameters of *p_rec*:

- $k_x = k_y = 3, n_x = 300, n_y = 250, \lambda_x = 0.01, \lambda_y = 0.01.$

Parameters of *p_rec* (deriv.):

- $k_x = k_y = 3, n_x = 300, n_y = 250, \lambda_x = 0.01, \lambda_y = 0.01.$

Parameters of *p_rec* (seg.):

- $k_x = k_y = 3, n_x = 45, n_y = 45, \lambda_x = 0.17, \lambda_y = 0.12.$

Parameters of *p1_rec* (seg.):

- $k_x = k_y = 3, n_x = 45, n_y = 45, \lambda_x = 0.05, \lambda_y = 0.05.$[4]

B.5 Test Surfaces

The discrete representations $\mathbf{Z}$, $\mathbf{Z}_x$, and $\mathbf{Z}_y$ of the following surfaces and gradients are *m*-by-*n* matrices calculated with *n* / *m* equidistant *x*- / *y*-values.

cos2

Surface and gradient components:

$$z(x, y) = \sin(x) + 0.1y + 0.2\cos(5x)\sin(y) \tag{B.1}$$
$$+ 0.1\cos(7x)\sin(7y)\exp\!\left(-5(x + \pi)^4\right),$$
$$z_x(x, y) = \cos(x) - \sin(5x)\sin(y) - 0.7\sin(7x)\sin(7y)\exp\!\left(-5(x + \pi)^4\right) \tag{B.2}$$
$$- 2(x + \pi)^3\cos(7x)\sin(7y)\exp\!\left(-5(x + \pi)^4\right),$$
$$z_y(x, y) = 0.1 + 0.2\cos(5x)\cos(y) + 0.7\cos(7x)\cos(7y)\exp\!\left(-5(x + \pi)^4\right). \tag{B.3}$$

---

[4]If Gurobi finds no solution for a segment after 45 s, λ_x and λ_y are increased by 0.002 for this segment.

Domain:

$$x \in [-2\pi, \pi] \ , \qquad y \in \begin{cases} [0, 20] & \text{for } m = 760, n = 930 \\ [0, 10] & \text{else} \end{cases} .$$

g2sTestSurf

Surface (calculation of the derivatives is left to the reader):

$$
\begin{aligned}
z(x, y) = {} & \tfrac{5}{2} \exp\left(-\tfrac{3}{16}x^2 + \tfrac{5}{8}x - \tfrac{19}{16} - \tfrac{1}{8}xy + \tfrac{7}{8}y - \tfrac{3}{16}y^2 \right) \\
& + 3 \exp\left(-\tfrac{2}{7}x^2 + \tfrac{32}{7}x - \tfrac{142}{7} - \tfrac{1}{7}xy + \tfrac{15}{7}y - \tfrac{1}{7}y^2 \right) \\
& - 5 \exp\left(-\tfrac{5}{18}x^2 + \tfrac{20}{9}x - \tfrac{125}{18} + \tfrac{1}{9}xy + \tfrac{5}{9}y - \tfrac{1}{9}y^2 \right) \\
& - 2 \exp\left(-\tfrac{3}{28}x^2 - \tfrac{1}{7}x - \tfrac{75}{7} + \tfrac{1}{14}xy + \tfrac{19}{7}y - \tfrac{5}{28}y^2 \right) \\
& + 5 \exp\left(-\tfrac{1}{6}x^2 + \tfrac{14}{3}x - \tfrac{194}{3} - \tfrac{1}{3}xy + \tfrac{38}{3}y - \tfrac{2}{3}y^2 \right) .
\end{aligned}
\tag{B.4}
$$

Domain:

$$x, y \in [-1, 10] \ .$$

sin2

Surface and gradient components:

$$z(x, y) = 1.6 \sin(x) \sin(y) y \ , \tag{B.5}$$

$$z_x(x, y) = 1.6 \cos(x) \sin(y) y \ , \tag{B.6}$$

$$z_y(x, y) = 1.6 \sin(x) \cos(y) y + 1.6 \sin(x) \sin(y) \ . \tag{B.7}$$

Domain:

$$x \in \left[\frac{\pi}{4}, 6\pi \right] \ , \qquad y \in \left[0, \frac{11\pi}{2} \right] \ .$$

Table of Functions C

Function	Description	Source
cos2	Test surface with analytic gradient.	-
diffusionA	Surface reconstruction 4.4.	http://www.amitkagrawal.com/software.html
discLS	Surface reconstruction 4.11.1.	http://ubee.enseeiht.fr/photometricstereo/
fc_agrawal	Surface reconstruction 4.1.	http://www.amitkagrawal.com/software.html
fc_ISG	Surface reconstruction 4.1.	-
fc_xiong	Surface reconstruction 4.1.	MathWorks File Exchange*
fill_gaps	Fill gaps in gradient.	http://www.aeon.de/heurisko_produkte.html
g2s	Surface reconstruction 4.6.	MathWorks File Exchange†
g2sSpectral	g2s with spectral Regularization.	MathWorks File Exchange†
g2sTestSurf	Test surface with analytic gradient.	MathWorks File Exchange†
gradient	Numerical gradient.	MATLAB
gradOp	Matrix differential operator **D**.	-
iga	Surface reconstruction 4.8.	https://github.com/jonabalzer/iga-integration
M_estim	Surface reconstruction 4.4.	http://www.amitkagrawal.com/software.html
mldivide, \	Solve systems of linear equations.	MATLAB
LADrec	Surface reconstruction 4.11.2.	-
LADrec2	Surface reconstruction 4.11.3.	-
LADrec3	Surface reconstruction 4.11.3.	-
LSrec	Surface reconstruction 4.11.1.	-
ramppeaks	Test surface with numeric gradient.	http://www.amitkagrawal.com/software.html
p_rec	Surface reconstruction 4.11.4.	-
p1_rec	Surface reconstruction 4.11.5.	-
scs	Surface reconstruction 4.2.	Based on scs_queau
scs_agrawal	Surface reconstruction 4.2.	http://www.amitkagrawal.com/software.html
scs_queau	Surface reconstruction 4.2.	http://ubee.enseeiht.fr/photometricstereo/
sin2	Test surface with analytic gradient.	-
tent	Test surface with discontinuities.	http://ubee.enseeiht.fr/photometricstereo/
wavelets	Surface reconstruction 4.10.	MathWorks File Exchange‡
wei	Surface reconstruction 4.3.	-
wei2	Surface reconstruction 4.3.	-

[*] https://de.mathworks.com/matlabcentral/fileexchange/45269-dfgbox
[†] https://de.mathworks.com/matlabcentral/fileexchange/43149%2Dsurface%2Dreconstruction%2Dfrom%2Dgradient%2Dfields--grad2surf%2Dversion%2D1%2D0
[‡] https://de.mathworks.com/matlabcentral/fileexchange/48066-wavelet-based-image%2Dreconstruction-from-gradient-data

Danksagung

Erklärung

Ich versichere, dass ich diese Arbeit selbstständig verfasst habe und keine anderen als die angegebenen Quellen und Hilfsmittel benutzt habe.

Heidelberg, den 9. Oktober 2017

. . . .

Corrigendum

Revised Version December 2017

The following list provides a description of the changes made to the thesis since the original version was printed:

- Page 3, Equation 1.1:

$$z\,(x, y) = \int_{\gamma} [p\,(x, y) + q\,(x, y)]\,\mathrm{d}x\,\mathrm{d}y = \int_{\gamma} \boldsymbol{g}\,(x, y)\,\mathrm{d}\boldsymbol{x}\,.$$

should read

$$z\,(x, y) = \int_{\gamma} [p\,(x, y)\,\mathrm{d}x + q\,(x, y)\,\mathrm{d}y] = \int_{\gamma} \boldsymbol{g}\,(x, y)\,\mathrm{d}\boldsymbol{x}\,.$$